

2012

# Experimental characterization of a liquid-liquid co-axial swirl rocket injector using non-invasive optical and X-ray techniques

Christopher Daniel Radke  
*Iowa State University*

Follow this and additional works at: <https://lib.dr.iastate.edu/etd>

 Part of the [Mechanical Engineering Commons](#)

## Recommended Citation

Radke, Christopher Daniel, "Experimental characterization of a liquid-liquid co-axial swirl rocket injector using non-invasive optical and X-ray techniques" (2012). *Graduate Theses and Dissertations*. 12789.  
<https://lib.dr.iastate.edu/etd/12789>

This Thesis is brought to you for free and open access by the Iowa State University Capstones, Theses and Dissertations at Iowa State University Digital Repository. It has been accepted for inclusion in Graduate Theses and Dissertations by an authorized administrator of Iowa State University Digital Repository. For more information, please contact [digirep@iastate.edu](mailto:digirep@iastate.edu).

**Experimental characterization of a liquid-liquid co-axial swirl rocket  
injector using non-invasive optical and X-ray techniques**

by

**Christopher Daniel Radke**

A thesis submitted to the graduate faculty  
in partial fulfillment of the requirements for the degree of  
**MASTER OF SCIENCE**

Major: Mechanical Engineering

Program of Study Committee:  
Terrence R Meyer, Major Professor  
Theodore Heindel  
James Hill

Iowa State University

Ames, Iowa

Copyright © Christopher Daniel Radke, 2012. All rights reserved.

## Table of Contents

List of Figures .....	v
List of Tables.....	x
Abstract.....	xi
Chapter 1. Introduction and Background.....	1
Chapter 2. Literature Review .....	4
2.1 Optical Techniques .....	4
2.1.1 High-speed Optical Imaging .....	4
2.1.2 Phase-Doppler interferometry .....	5
2.1.3 X-Ray Radiography and Computed Tomography.....	6
2.2 Rocket Spray Background .....	8
2.2.1 Rocketry Background.....	8
2.2.2 Fuel Background .....	9
2.2.3 Combustion Instability .....	10
2.3 Spray Background.....	12
2.3.1 Injector Introduction .....	12
2.3.2 Coaxial Injector Atomization .....	13
Chapter 3. Experimental Setup .....	18
3.1 Objectives of Laboratory Setup .....	18
3.2 Data Collection Devices .....	18
3.2.1 High Speed Imaging.....	18
3.2.2 Phase Doppler Particle Analyzer: Setup .....	19
3.2.3 Phase Doppler Particle Analyzer: Processing .....	21
3.2.4 X-ray Setup.....	22
3.2.5 Absorption Coefficient Study.....	24
Chapter 4. Results: Effects of Injector Geometry and Injection Pressure .....	26
4.1 Overview.....	26
4.2 Image Processing .....	26
4.3 Investigation of Recess Designs .....	27
4.4 Effects of Varying Recess Design and Injection Pressure.....	29

4.4.1 Overview on Effects of Recess Design.....	29
4.4.2 Discussion of Results at Low Injection Pressures .....	30
4.4.3 Discussion of Results at High Injection Pressures.....	33
4.4.4 Discussion on spray cone angle and sheet stability .....	33
4.4.5 Discussion of Geometric Factors on Breakup and Atomization.....	35
4.4.6 Recess Design Conclusions .....	38
Chapter 5. Results: Effects of Fluid Properties and Injection Pressure .....	40
5.1 Fluid Properties.....	40
5.2 Survey of Images Varying Fluid Properties and Injection Pressure .....	41
5.2.1 Results: High Speed Images Varying Fluid Properties and Injection Pressure .....	41
5.3 PDPA Data Collection and Processing.....	46
5.4 Spray Characterization Methods.....	49
5.5 PDPA Results.....	50
5.5.1 Discussion of Axial Velocity Result.....	51
5.5.2 Droplet Diameter Results.....	55
5.5.1 Discussion of Breakup Type from PDPA Analysis.....	63
5.5.2 PDPA Analysis of Breakup Length.....	65
Chapter 6. Results: X- Imaging .....	68
6.1 Overview .....	68
6.2 Experimental Considerations .....	68
6.3 Radiograph Data.....	70
6.3.1 Radiographs.....	70
6.3.2 Radiograph Results.....	74
6.4 X-ray CT Data .....	75
6.5 Discussion .....	76
6.6 A novel use of high speed images as a supplement to CT scans for sheet thickness .....	77
6.6.1 Motivation .....	77
6.6.2 Development .....	77
6.6.3 Results .....	78
Chapter 7. Summary and Future Work.....	82
7.1 Conclusions.....	82
7.2 Future Work.....	83
Chapter 8: Works Cited .....	85
Appendix A: Data for Different Recess Designs and Varying Pressure.....	90
A.1 Data for Recess Design 1 .....	90
A.2 Data for Recess Design 2 .....	91
A.3 Data for Recess Design 3 .....	92
A.4 Data for Recess Design 4 .....	93

A.5 Data for Recess Design 5 .....	94
Appendix B: Data for Different Fluids and Varying Pressure.....	95
B.1 Data for Acetone.....	95
B.2 Data for Methanol.....	96
B.3 Data for JP-8.....	97
B.4 Data for Water .....	98
Appendix C: PDPA data .....	99
C.1 Effects of Fluid Properties on Droplet Velocity.....	99
C.1.1 Mean Axial Velocity, 25mm from injector exit .....	99
C.1.2 Mean Axial Velocity, 50 mm from injector exit .....	100
C.1.3 Mean Axial Velocity, 75 mm from injector exit .....	101
C.2 Effects of Fluid Properties on Droplet Velocity.....	102
C.2.1 Mean Radial Velocity, 25mm from Injector Exit.....	102
C.2.2 Mean Radial Velocity, 50mm from injector exit.....	103
C.2.3 Mean Radial Velocity, 75mm from injector exit.....	104
C.3 Composite Velocity Magnitude .....	105
C.3.1 Composite Velocity Magnitude, 25 mm from injector exit.....	105
C.3.2 Composite Velocity Magnitude, 50 mm from injector exit.....	106
C.3.3 Composite Velocity Magnitude, 75 mm from injector exit.....	107
C.4 Effects of Fluid Properties on Sauter Mean Diameter (SMD) .....	108
C.4.1 SMD of fluids at 25 mm from injector exit .....	108
C.4.2 SMD of fluids 50 mm from injector exit .....	109
C.4.3 SMD of fluids 75 mm from injector exit .....	110
C.5 Droplet Weber Number .....	111
C.5.1 Droplet Weber Number, 25 mm from injector exit .....	111
C.5.2 Droplet Weber Number, 50 mm from injector exit .....	112
C.5.3 Droplet Weber Number, 75 mm from injector exit .....	113
C.6 Droplet Reynolds Number .....	114
C.6.1 Droplet Reynolds Number, 25 mm from injector exit.....	114
C.6.2 Droplet Reynolds Number, 50 mm from injector exit.....	115
C.6.2 Droplet Reynolds Number, 75 mm from injector exit.....	116
Appendix D: Code .....	117
D.1 PDPA Data Extraction Code .....	117
Acknowledgements.....	123

## List of Figures

Figure 1: Cross-sectional view of a liquid-liquid coaxial swirl injector.....	14
Figure 2: Picture illustrating hole formation, hole breaking, ligament formation, and ligament breaking and droplet formation.....	16
Figure 3: Setup for high-speed imaging. A Photron FASTCAM SA5 was used to image spray breakup. A DC light source was used to ensure a diffuse background.....	19
Figure 4: PDPA system. A Spectra-Physics Sabilite 2017 laser emits an Argon-Ion beam which is split in a Fiberlight™ beam separator and then emitted through a transceiver probe. Atomized drops refract light which is recorded at the receiver and processed. .....	21
Figure 5: Absorption coefficient versus KI concentration.....	24
Figure 6: Comparison between unprocessed image on left compared to post-processed image on right. ....	27
Figure 7: Cross section of swirler with 'Recess Design' dimensions shown. ....	28
Figure 8: Scaled images of the different recess designs are shown above. Values for varied parameters can be seen in Table 1. Recess designs are numbered as 1 at far left to 5 at far right.....	29
Figure 9: Exceptional sheet stability demonstrated for Recess Design 4 at the lower injection pressure of 69 kPa psi (left) and large-scale oscillations with heterogeneous breakup visible for Recess Design 5 at 69 kPa (right).....	32
Figure 10: Stable sheet formation with uniform droplet breakup and distribution indicate stable low-pressure atomization for Recessed Design 1, 2 and 3 (left to right). ....	32
Figure 11: A comparison between Recess Design 3 (left) and Recess Design 5 (right) at 344.7 kPa. Recess Design 3 exhibits faster and more uniform atomization. This is observed in the existence of stable fluid sheet segment at increased axial locations .	33
Figure 12: Comparison between breakup length minimum (Recess Design 3 at left) and maximum (Recess Design 4 at right).....	36
Figure 13: Comparison between ligament forming from the liquid sheet (left) and widespread hole merging induced droplet breakup (right). ....	37

Figure 14: A comparison showing visible small-scale instability at left and large-scale instability propagation at right. Fluids are acetone at left, and JP-8 at right. Both are injected at 34.47 kPa and imaged at 12 kHz. ....	42
Figure 15: Closed rim flow illuminated with argon-ion laser showing refracted light internally reflecting interior to the cone.....	43
Figure 16: Comparison between global and local instability wave propagation and droplet formation. Injected fluid at left is Water and Methanol at right. ....	44
Figure 17: Comparison in breakup length between JP-8 (left) and acetone (right) at 137.9 kPa.....	45
Figure 18: PDPA data collection locations. ....	47
Figure 19: Image of injector setup and beam placement verification.....	48
Figure 20: Stored array of radial location, axial location, and quantity of interest. This array is created for each pressure case. ....	49
Figure 21: A comparison of magnitude increase across the fluid sheet with increasing pressure for water (left) and acetone (right) at a fixed axial distance.....	52
Figure 22: Evolution of velocity magnitude over a range of axial distances for water (left) and JP-8 (right) .....	53
Figure 23: Evolution of velocity magnitude for axial distances 75mm from the injector for water (left) and JP-8 (right).....	54
Figure 24: Droplet diameter histogram comparison between different fluids at an identical axial distance and injection pressure of 344 kPa .....	56
Figure 25: Comparison of droplet diameter histograms of JP-8 at an identical spatial coordinates but at injection pressures of 137 kPa and 344 kPa .....	58
Figure 26: Histogram comparison of water at different axial locations across the fluid sheet. ....	60
Figure 27: Sauter Mean Diameter evolution over a range of pressures and radial locations for acetone (left) and JP-8 (right). ....	61
Figure 28 Sauter Mean Diameter evolution over a range of axial distances from the injector. ....	62

Figure 29: Sauter Mean Diameter evolution over a range of axial distances from the injector. .....	63
Figure 30: Comparison between global instability producing consistent drops in a narrow range, to local instability creating a range of droplets at various locations .....	64
Figure 31: Comparisons between axial velocity distributions correlating to breakup type....	64
Figure 32: Comparisons of Sauter Mean Diameter variance correlating to breakup type.....	65
Figure 33: A comparison of axial velocity distribution, evolution over a range of axial distances from the injector .....	66
Figure 34: X-ray radiographs with differencing levels of potassium iodide (KI). Case with 15%, 25%, and 32% are shown on the left, middle, and right, respectively. ....	69
Figure 35: X-ray radiographs cuvettes of air, deionized water, and deionized water mixed with KI at concentrations of 10%, 15%, 20%, 25%, 30%, 35%, 40%, 50% by mass.69	
Figure 36: Absorption coefficient versus KI concentration.....	70
Figure 37: Radiograph of Recess Design 1 (left) and Recess Design 2 (right) at 137.9 kPa .	71
Figure 38: Radiograph of Recess Design 3 (left) and Recess Design 4 (right) at 137.9 kPa .	72
Figure 39: Radiograph of Recess Design 5 at 137.9 kPa.....	72
Figure 40: Recess Design 1 at 68.95 kPa, 137.9 kPa, and 206.8 kPa, from left to right .....	73
Figure 41: Experimental sheet thickness values for different recess numbers .....	74
Figure 42:3-D CT reconstruction of time-averaged spray for Recessed Length 1 at 137kPa injector inlet pressure.....	75
Figure 43: 68.95 kPa flow of deionized water for use in velocity extraction.....	79
Figure 44: Experimentally produced velocity vs. pressure curve.....	80
Figure 45: High Speed images of spray breakup for Recessed Length 1 at 12 kHz. Injection pressures are at 68.98, 137.90 and 206.84 kPa (left to right, top panel), and 275.79, 344.74, 413.68 kPa, (left to right, bottom panel) collected at 12 kHz.....	90
Figure 46: High Speed images of spray breakup for Recessed Length 1 at 20 kHz. Injection pressures are at 482.63, 551.85 kPa, and 620 kPa from left to right. ....	91
Figure 47: High Speed images of spray breakup for Recessed Length 2 at 12 kHz. Injection pressures are at 68.98, 137.90 and 206.84 kPa (left to right, top panel), and 275.79, 344.74, 413.68 kPa, (left to right, bottom panel) collected at 12 kHz.....	91

- Figure 48: High Speed images of spray breakup for Recessed Length 2 at 20 kHz. Injection pressures are at 482.63, 551.85 kPa, and 620 kPa from left to right. .... 91
- Figure 49: High Speed images of spray breakup for Recessed Length 3 at 12 kHz. Injection pressures are at 68.98, 137.90 and 206.84 kPa (left to right, top panel), and 275.79, 344.74, 413.68 kPa, (left to right, bottom panel) collected at 12 kHz..... 92
- Figure 50: High Speed images of spray breakup for Recessed Length 3 at 20 kHz. Injection pressures are at 482.63, 551.85 kPa, and 620 kPa from left to right. .... 92
- Figure 51: High Speed images of spray breakup for Recessed Length 4 at 12 kHz. Injection pressures are at 68.98, 137.90 and 206.84 kPa (left to right, top panel), and 275.79, 344.74, 413.68 kPa, (left to right, bottom panel) collected at 12 kHz..... 93
- Figure 52: High Speed images of spray breakup for Recessed Length 4 at 20 kHz. Injection pressures are at 482.63, 551.85 kPa, and 620 kPa from left to right. .... 93
- Figure 53: High Speed images of spray breakup for Recessed Length 5 at 12 kHz. Injection pressures are at 68.98, 137.90 and 206.84 kPa (left to right, top panel), and 275.79, 344.74, 413.68 kPa, (left to right, bottom panel) collected at 12 kHz..... 94
- Figure 54: High Speed images of spray breakup for Recessed Length 5 at 20 kHz. Injection pressures are at 482.63, 551.85 kPa, and 620 kPa from left to right. .... 94
- Figure 55: Acetone injected at 34.5, 69.0, 137.9 kPa (left to right, top panel), and 207, 276, and 345 kPa, (left to right, bottom panel) collected at 12 kHz. .... 95
- Figure 56: Acetone injected at 413.68 (left panel) and 482.63 kPa (right panel) collected at 20 kHz..... 95
- Figure 57: Methanol injected at 34.47, 68.98, 137.90 kPa (left to right, top panel), and 206.84, 275.79, and 344.74 kPa, (left to right, bottom panel) collected at 12 kHz .... 96
- Figure 58: Methanol injected at 413.68 (left panel) and 482.63 kPa (right panel) collected at 20 kHz..... 96
- Figure 59: JP-8 injected at 34.47, 68.98, 137.90 kPa (left to right, top panel), and 206.84, 275.79, and 344.74 kPa, (left to right, bottom panel) collected at 12 kHz ..... 97
- Figure 60: JP-8 injected at 413.68 (left panel) and 482.63 kPa (right panel) collected at 20 kHz..... 97

Figure 61: Water injected at 34.47, 68.98, 137.90 kPa (left to right, top panel), and 206.84, 275.79, and 344.74 kPa, (left to right, bottom panel) collected at 12 kHz .....	98
Figure 62: Water injected at 413.68 (left panel) and 482.63 kPa (right panel) collected at 20 kHz.....	98
Figure 63: Comparison of median axial velocities 25 mm from injector exit. ....	99
Figure 64: Comparison of median axial velocities 50 mm from injector exit. ....	100
Figure 65: Comparison of median axial velocities 75 mm from injector exit. ....	101
Figure 66: Comparison of composite velocity magnitude, 25 mm from the injector exit....	105
Figure 67: Comparison of composite velocity magnitude, 50 mm from the injector exit....	106
Figure 68: Comparison of composite velocity magnitude, 75 mm from the injector exit....	107
Figure 69: Comparison of Sauter Mean Diameters 25 mm from the injector exit. ....	108
Figure 70: Comparison of Sauter Mean Diameters 50 mm from the injector exit. ....	109
Figure 71: Comparison of Sauter Mean Diameters 75 mm from the injector exit. ....	110
Figure 72: Comparison of Droplet Weber Number, 25mm from the injector exit. ....	111
Figure 73: Comparison of Droplet Weber Number, 50 mm from the injector exit. ....	112
Figure 74: Comparison of Droplet Weber Number, 75 mm from the injector exit. ....	113
Figure 75: Comparison of Droplet Reynolds Number, 25 mm from the injector exit.....	114
Figure 76: Comparison of Droplet Reynolds Number, 50 mm from the injector exit.....	115
Figure 77: Comparison of Droplet Reynolds Number, 75 mm from the injector exit.....	116

## List of Tables

Table 1: Recess Design Parameters. ....	29
Table 2: Spray cone angles for recess length designs. ....	34
Table 3: Fluid properties and dimensional parameters. ....	41
Table 4: Velocity extraction from high speed images .....	79

## Abstract

Thermo-acoustic combustion instability is a problem that has been researched for decades as it is a precursor to sudden catastrophic failure. Meanwhile, the demand for rocket engines that are able to maintain stable combustion over a wider range of thrust levels is increasing. One injector design utilized in Russia and Asia that has demonstrated stable throttling ability is the liquid-liquid co-axial swirl injector.

Simultaneously, interest in alternative hydrocarbon rocket fuels has led to research on a wide range of fuel compositions that deviate from conventional kerosene-based rocket fuel. Hence, it is also necessary to determine how fuel properties will affect the performance of particular injector designs.

The goal of the current work is to characterize the atomization and spray properties of a liquid-liquid co-axial swirl injector to evaluate feasibility for potential use in rocket engines. This work was accomplished through the use of non-invasive optical and X-ray techniques including high-speed imaging, phase doppler interferometry, X-ray radiography, and three-dimensional computed tomography. These techniques provided information about break-up mechanisms, break-up lengths, droplet size distributions, and time-averaged liquid mass distributions. An injector with five different nozzle exit geometries was designed, constructed, and implemented for these experiments. The current work was able to demonstrate that geometrical factors such as design of the recessed nozzle exit segments can be optimized to increase breakup and promote more uniform particle distributions. Additionally, the study quantified flow characteristics of the injector over a large number flow parameters, including injection pressure and liquid properties, allowing for better

estimates on the potential flow characteristics and breakup for use with conventional and alternative rocket fuels.

## Chapter 1. Introduction and Background

Rocket engines play a crucial role in many propulsion applications. As a specific subset of these, bi-propellant hydrocarbon engines are among the most popular types of rocket engines to date. Bi-propellant hydrocarbon engines work by forcibly mixing a hydrocarbon fuel with an oxidizer in such a way as to mix the propellants while simultaneously atomizing or breaking up the mixture sufficiently to provide stable combustion. Because of the complexity of the fuel injection process, new designs and fuel mixtures for bi-propellant hydrocarbon rocket engines are still areas of active research. While many additional fuels such as hydrogen and various hypergolic fuels have been utilized in different combinations over the years, hydrocarbon fuels remain on the forefront of rocket engine design due to their low cost, availability, density, and adequate performance.

While rocket injector design is a large area of active research, there have been increased requirements for engines designed to provide stable thrust over a wide range of thrust levels. One type of rocket engine design that has demonstrated exceptional performance over many operating conditions is the liquid-liquid swirl injector. In the liquid-liquid swirl injector studied in this work, a fuel and an oxidizer are each forced through a separate set of tangential holes with sufficient pressure to create vortices that propagate through the injector housing. The vortices then merge and mix, creating a liquid sheet that atomizes and combusts. Understanding the mixing and atomization of this spray is of interest to scientists looking to utilize this injector and improve upon its theoretical and demonstrated performance.

To effectively study the dynamics of the fluid system, non-invasive experimental techniques have been utilized. In the current work, high-speed optical imaging, laser-based phase Doppler interferometry, X-ray radiography, and three-dimensional computed tomography have been selected to create a composite picture of the fluid dynamics of the liquid-liquid swirl injector without disturbing the flow. High-speed imaging captured the liquid breakup process and the cascade from liquid sheets to large ligaments and droplets. This provided physical insight into the physical processes that control the final droplet and fuel mass distribution. Laser diagnostics allowed for measurements of droplet size and velocity distributions of those droplets, but was limited to point-by-point measurements at various locations within the flowfield. X-ray radiography and computed tomography allowed for line-of-sight and three-dimensional, respectively, time-averaged measurements of the liquid-mass distribution, with the potential for quantitative accuracy for evaluating the effects of various design parameters and for use in model validation. Although a number of recent studies using X-ray radiography have used synchrotron sources, all experimental techniques in this work were performed using a tube source at Iowa State University, which allowed for many different flow conditions to be studied as well as geometric parameters to be varied.

This study represents the first comprehensive study to evaluate the liquid breakup mechanisms, droplet size and velocity statistics, and liquid mass distributions for liquid-liquid swirl injectors. In fact, this represents the first combined use of these optical and X-ray techniques for spray analysis. Furthermore, this study evaluates the effects of the internal geometry and operating conditions (e.g., injection pressure and liquid properties) on the spray behavior.

Additional background on the experimental configuration and techniques is provided in the literature review. The techniques utilized and the experimental setup will be explained further in the following sections. The results will then be analyzed and discussed to characterize the injection process, the dependence on injector design parameters, operating conditions, fluid properties, and the success of the experimental approach. Finally, the thesis will state the overall conclusions and future work that might be conducted as a follow-up to this research.

## Chapter 2. Literature Review

### 2.1 Optical Techniques

#### 2.1.1 High-speed Optical Imaging

High speed imaging allows for optical images of spray breakup to be taken with a repetition rate that can record the fastest occurring phenomena of interest in the fluid system. Early work on high-speed spray imaging relied on high-speed rotating drum cameras (Hamady, et al., 1994) (Welberger & Cartellieri, 1987) and have evolved into current day high-speed CMOS cameras used in this work. A key feature is that the camera should be capable of freezing the fluid motion. This was accomplished in older camera systems using a strobe light, while the current CMOS system can electronically shutter the camera down to 1 microsecond or less. Of course, by shuttering down to a very short detection time, the camera must be sensitive enough to record enough light to see the spray.

While limited in quantitative information, high speed imaging allows for a large amount of qualitative information to be collected in a straightforward, non-invasive manner. One specific advantage of high speed imaging is that it allows for instantaneous macroscopic phenomena to be observed with full frame images with temporal resolution that is on the order of, or faster than, most of the relevant flow phenomena. This macroscopic qualitative data allows for study of the larger, unsteady spray features, in contrast to the other techniques which provide instantaneous data with point measurements or provide time-averaged data over the entire spray field. Additionally, high speed images provide information that is valid

over the full range of flow regimes and regardless of fluid structure (spherical or non-spherical), so long as the fluid structure can be illuminated and resolved by the camera.

In the current work, images were collected at speeds up to 20 kHz without the use of a stroboscope. This high frame rate allowed for quantification of ligament breakup, spray cone angle, and sheet instability propagation. Additionally, other information such as the regime of liquid sheet breakup and relative droplet sizes could be inferred and compared with images of different flow conditions and geometric parameters.

### **2.1.2 Phase-Doppler interferometry**

Phase-Doppler interferometry (PDI) is a technique that utilizes light scattering from the interference fringe pattern produced at the crossing point of two laser beams to extract droplet size, velocity, and associated statistical distributions (Meyer, et al., 2010). PDI has become a standard technique for spray analysis due to its widespread application and has been well documented in the literature. An integrated PDI unit called a Phase Doppler Particle Analyzer (PDPA) was used to conduct the research reported here. A thorough review of the theory and applications of PDPA is given in the literature (Bachalo & Houser, 1987) (Bachalo, 2000). PDI techniques including PDPA provide a non-invasive and highly accurate technique to characterize the spray including droplet size, velocity, time-of-arrival statistics, number density, as well as volume and mass flux, instantaneously and over a wide range of values (Bachalo, 2000).

PDPA works by combining two monochromatic laser beams of known wavelength at a focal point with small half angle. An interference pattern of known size and with known spacing, dependent on the incoming laser beams, is then created. As droplets propagate

through the fringe volume, light is scattered and collected by a receiver, creating a signal of oscillating intensity known as a Doppler burst (Meyer, et al., 2010). This Doppler burst allows for computation of droplet velocity. Since the distance between fringes is known, the rate at which each fringe is scattered yields a highly accurate velocity measurement.

While velocity is a key component of atomization and spray data, simultaneous droplet size and velocity is desired. In order to achieve this, a known phase shift is applied to one beam using a Bragg Cell. Then, using the spherical drop as a refractive lens to focus and expand the beam, an interference pattern is projected and captured by the receiver (Bachalo, 2000); since both beams incident to the droplet approach the drop at different angles, the difference in optical path which has traveled through the droplet produces an interference pattern which is a function of only wavelength, refractive index, angles of incidence, and droplet diameter (Bachalo & Houser, 1987). Thus, the projected fringe pattern can be used to calculate droplet diameter. The Doppler bursts occur each time a droplet passes through the probe volume defined by the region of the crossed beams, and each burst is collected using high-speed photodetectors. Hence, the data rate can be as high as several thousand per second depending on the rate at which droplets cross the probe volume. This depends on the droplet density and velocity. Commercial software is then used to process each burst and provide the aforementioned statistics on droplet size, velocity, time-of-arrival, number density, as well as volume and mass flux.

### **2.1.3 X-Ray Radiography and Computed Tomography**

To fully understand spray breakup and atomization, measurements interior to the spray are required. Information regarding three-dimensional mass distribution throughout the

spray is required to understand the mass transfer to the ambient air and distribution once the fluid has left the injector in the liquid core region of the spray.

The most fundamental difference between visible light and X-ray radiation is the difference in wavelength. In the electromagnetic spectrum, visible light spans from roughly 380 nm to 0.7  $\mu\text{m}$  in wavelength compared to X-rays, which span from 0.1nm to 10nm . One major consequence of this is the dominating interaction mechanisms of the different light with a fluid medium. Unlike visible light which scatters off fluid media and sprays, X-rays of sufficient energy (<20 keV) are mostly absorbed by the fluid medium (Linne, 2012). This holds a significant advantage over optical techniques in that multiple scattering does not significantly weaken the signal or produce false or distorted signals (Kastengren & Powell, 2007); additionally, if scattering is ignored, the X-ray intensity when passing through a sample can be given as (Kastengren & Powell, 2007):

$$\frac{dI(\lambda,t)}{dz} = -\varepsilon(\lambda)I(\lambda,t) \quad [1]$$

where  $I$  is the X-ray intensity,  $z$  is the direction of X-ray propagation, and  $\varepsilon(\lambda)$  is the linear absorption coefficient. This can be solved and written as the Lambert-Beer law (Linne, 2012):

$$\tau = \frac{I_l}{I_o} = e^{-\mu_m l} \quad [2]$$

where  $\mu_m$  is a mass based absorption coefficient,  $l$  is the path length,  $I_l$  is the received beam intensity, and  $I_o$  is the emitted beam intensity. This coefficient represents the local mass of the material of interest for a line of sight between the emitted beam and the sensor. Based on the intensity of the emitted X-ray, the intensity received at the sensor, and a mass based

absorption coefficient unique to the spray of interest, a path length  $l$  can be solved (Linne, 2012).

To implement this technique, X-rays are propagated through the spray of interest and onto a camera and recorded as a radiograph. The camera or spray can then be reoriented to collect more time-averaged images and provide a three-dimensional computed tomographic image of mass absorption (Meyer, et al., 2008) (Heindel, et al., 2008).

## 2.2 Rocket Spray Background

### 2.2.1 Rocketry Background

Aerospace propulsion systems can be divided into 3 main categories: chemical propulsion, nuclear propulsion, and solar propulsion (Sutton & Biblarz, 2001) (Holden, 1990). Stored chemical propulsion has many applications and is widely used in government, private, and commercial applications (Sutton & Biblarz, 2001). Because of their wide utilization, chemical propulsion systems are a major area of academic interest and research. This work is ongoing in many areas including chemical kinetics (Joo & Gülder, 2010) (Glarborg & Nils, 1992), modeling (Beckstead, et al., 2007) (Colket & Spadaccini, 2001), new fuels (Son, 2007), (Rapp & Zurawski, 1988) (Natan & Rahimi, 2001), and applied or experimental testing and implementation (Sun, et al., 2008) (Klimenki, et al., 2002) (Cohn, et al., 2003) (Muss, et al., 2003) (Cheng, et al., 2002).

One specific field of stored chemical combustion is rocketry. Fundamentally, rockets are separated from turbojet combustion by their requirement to use a stored oxidizer instead

of air for combustion. This requirement, while inconvenient because of the requirement for oxygen storage tanks, does lead to the benefit of the exact knowledge and choice of oxidizer to be used in the combustion process. Additionally, with the removal of non-yielding species from the oxidizer such as nitrogen, combustion reaction rates are significantly higher. The very high reaction rates at the high combustion temperatures lead to efficiencies between 95%-99.5% (Sutton & Biblarz, 2001).

A specific subset of stored chemical rockets, are bi-propellant rockets. In a bi-propellant rocket, the fuel and oxidizer are stored in separate tanks and forcibly mixed in the combustion chamber. Bi-propellant rocket engines represent a large percentage of rocket engines manufactured today and can utilize a variety of fuels.

### **2.2.2 Fuel Background**

With the wide range of applications and specific requirements, many types of rocket fuels have been tested for various applications. Hydrocarbons, for example, have been used in production rocket engines since the Thor and Jupiter intercontinental ballistic missiles (ICBM) in the 1950's due to their high energy densities, low cost, and availability (Clark, 1972). In 1957, a kerosene derived fuel tailored for rocketry applications, Rocket Propellant 1 (RP-1), was issued with an olefin content less than 1% and an aromatic content less than 5%. RP-1 has had huge success over time, being successfully implemented as fuel for the main stage F-1 motor on the Saturn V as part of the Apollo Program (Clark, 1972) to today's Space-X Merlin Engine (Space Exploration Technologies Corp, 2012). Even with its historical pedigree, RP-1 is still an active area of research in both experimental applications

(Muss, et al., 2003) and in improving fundamental chemical kinetics (Andersen & Bruno, 2005).

However, with the great number of potential hydrocarbon molecules, research is ongoing on a number of similar hydrocarbon blends for rocketry applications. All will be expected to have similar or increased energy density, favorable coking and corrosion behavior, as well as the ability to withstand high temperatures for regenerative cooling without dissociating and polymerizing (Cohn, et al., 2003).

One fuel that has been considered internationally as a potential hydrocarbon fuel for rocketry applications is methane. Methane has several significantly favorable qualities including: ecological cleanliness, favorable handling qualities, adequate cooling, vast availability, low cost, and potential inner-solar availability (Klepikov, et al., 1997) (Holladay, et al., 2007) (Ash, et al., 1978).

### **2.2.3 Combustion Instability**

While there have been numerous types of bi-propellant rocket injectors, all maintain the same primary goal to mix a fuel and oxidizer while atomizing the mixture into small droplets to facilitate efficient vaporization, mixing, and combustion. However, because atomization is designed to be an inherently unstable process with a wide range of droplet size distributions, combustion instability has occurred in most, if not practically all, rocket development programs (Culick & Yang, 1995) (Yodiz, 1968).

Combustion instability is a diverse and active area of research with disciplines in areas of fundamental understanding (Chehroudi, 2010), numerical analysis (Gotsulenko,

2008) (Ryan, et al., 1995), passive suppression (Greatrix, 2012) (Wicker, et al., 1995), and active control (Saiki, et al., 2011) (Fung & Yang, 1992).

Fundamentally, combustion instability occurs because spray breakup is a finite and periodic process leading to periodic droplet evaporation and heat release, followed by pulsed acoustic wave propagation throughout the chamber (Culick & Yang, 1995). Many injector types, such as impinging jets and swirl injectors, forcibly mix the propellants in such a way to create a liquid sheet which further dissolves. Because this process is periodic, energy release tends to be coupled to this breakup frequency, which drives acoustic wave propagation throughout the chamber. Since most rocket chambers are designed to limit friction and heating along the walls, combustion chambers provide minimal frictional damping to acoustic wave propagation (Culick & Yang, 1995). Moreover, as the wave propagates down through the combustion chamber, the nozzle choke area can create a rebounding effect where the acoustic waves are redirected towards the injector, increasing the local fuel and oxidizer concentrations and consequently increasing the combustion rate. If undamped, this system can grow without bound leading to engine failure. The general process governing this system was first discovered by Lord Rayleigh and is characterized by Rayleigh's Criterion (Culick & Yang, 1995).

In addition to longitudinal wave propagation, forced acoustic wave propagation can occur radially or tangentially and phase lock with the resonant frequency of the chamber, also driving the system to an unstable condition and potentially to failure. Furthermore, acoustic waves can induce non-acoustic, low-frequency instabilities throughout the vehicle.

Much work has gone into preventing combustion instability through various methods. One of the most popular methods is through the use of acoustic baffles to forcibly dampen

propagating acoustic waves (Yang, et al., 1995) and the use of acoustic resonators and cavities which are narrowband absorbers and are tuned to specific eigenvalues of the combustion chamber (Laudien, et al., 1995). Other research has gone into actively controlling pressure and acoustic dynamics internal to the combustion chamber using closed loop controllers (Fung & Yang, 1992).

Despite external control mechanisms, further characterizing and understanding droplet breakup is critical in efforts to reduce combustion instability. Complicating this task is the desire for increasingly robust engines with the ability to stably operate at a much larger range of thrust conditions. This requirement provides significant difficulty for certain injectors, such as impinging jet injectors that utilize a momentum balance of fuel and oxidizer to create stable combustion over a range of thrust levels. New injector designs however, such as liquid-liquid swirl injectors have recently been the subject of much recent work because of theoretically demonstrated throttle stability over a range of throttle points (Soltani, et al., 2005) (Inamura, et al., 2003) (Kim, et al., 2007) (Ismailov & Heister, 2011). However, only limited work has been performed on experimentally investigating the injector. Furthermore, recent work suggests that swirl injector breakup exhibits resonance at particular frequencies, making the injector more susceptible to injector instability (Ismailov & Heister, 2011). However, this phenomena has not been experimentally verified.

## **2.3 Spray Background**

### **2.3.1 Injector Introduction**

Efficient mixing, uniform mass distribution, and efficient atomization are the primary goals of all rocket injectors (Kim, et al., 2007). Many different types of rocket injectors have

been utilized over time, including impinging jet injectors, pintle, and swirl or coaxial injectors, and extensive studies have been carried out to further understand and characterize spray dynamics and droplet breakup. Coaxial injectors have several advantages including high performance, uniform mass distribution and exceptional stability over a wide range of operating conditions. (Kim, et al., 2007) (Soltani, et al., 2005) (Lefebvre, 1989). Coaxial injectors are often classified based on propellant phase and relative propellant motion. For example, a gas-liquid swirl-shear injector indicates that the fuel or oxidizer is gas and the other is liquid; furthermore, the liquid is swirled and the breakup is induced through shear relative to the gas phase.

### **2.3.2 Coaxial Injector Atomization**

Coaxial injectors work by creating a set of overlapped swirling vortices which breakup due to instability. An example is shown in Fig. 1, in which liquid swirl is imparted to the central passage and another liquid swirl is imparted downstream in a mixing zone prior to the nozzle exit. Much work has been done on liquid sheet instability and many detailed reviews exist (Ashgriz, et al., 2011). A brief review on the topic will be given in sufficient detail that flow phenomena of interest will be introduced.

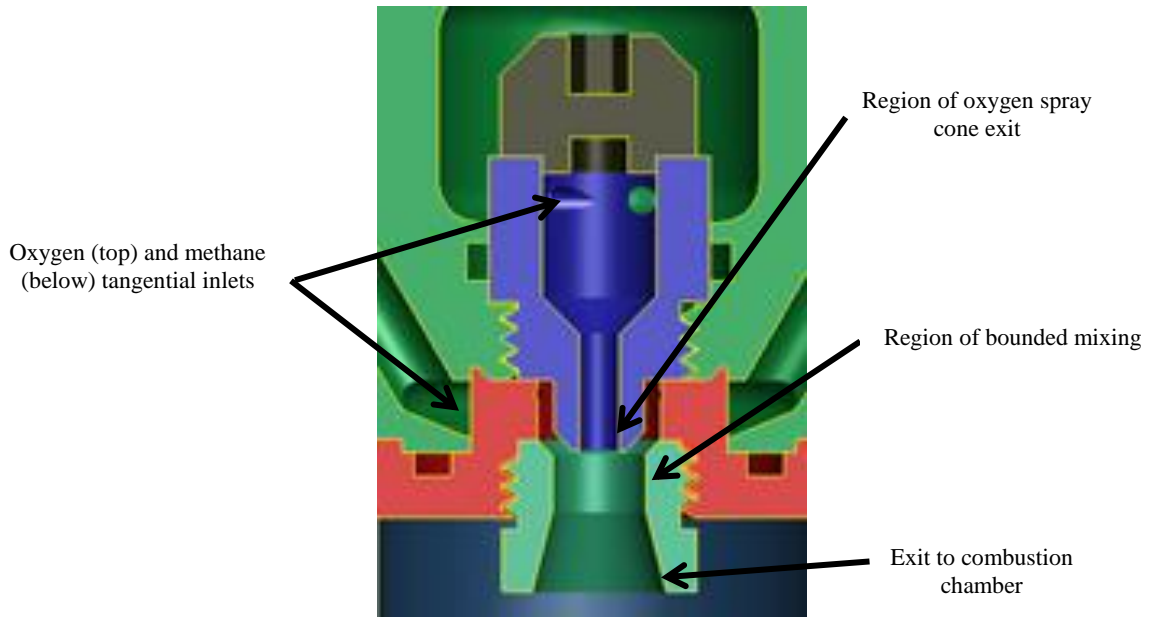


Figure 1: Cross-sectional view of a liquid-liquid coaxial swirl injector.

A liquid sheet is initially stable until it is disturbed by interactions with its surrounding medium. Aerodynamic forces in both gaseous and liquid environments create drag and pressure induced perturbations which propagate along the liquid sheet. (Taylor, 1959). When the sheet is disturbed, surface tension forces work to stabilize the planar liquid sheet. This rebounding force often leads to oscillations which occur in two dominating modes: symmetric and antisymmetric (Taylor, 1959). For an inviscid, irrotational, incompressible liquid sheet, the sheet can be described by a wave equation as:

$$\varphi = [A \cosh(ky) + B \sinh(ky)]e^{ikx - \omega t} \quad [3]$$

where  $k$  and  $\omega$  are the disturbance wave number and frequency, respectively (Ashgriz, et al., 2011). Also,  $A=0$  for an antisymmetric oscillation and  $B=0$  for a symmetric mode. Further, the disturbance frequency is comprised of a real and imaginary component and given as:

$$\omega = \omega_r + i\omega_i \quad [4]$$

where  $\omega_r$  is the real component representing the growth or damping rate and  $\omega_i$  represents the wave velocity of the disturbance. The growth rate can also be found to be:

$$\frac{\omega_r}{kU_0} = \left[ \frac{\varepsilon K}{(\varepsilon+K)^2} - \frac{ka}{We} \frac{1}{\varepsilon+K} \right]^{1/2} \quad [5]$$

where the Weber number is given as  $We = \rho_L U_0^2 a / \sigma$ ,  $\varepsilon = \rho_g / \rho_L$ , and  $K = \tanh(ka)$  for antisymmetric oscillations and  $K = \coth(ka)$  for symmetric oscillations. This equation can be interpreted so that for all density ratios and regardless of oscillation type, disturbance growth increases with increasing Weber number (Ashgriz, et al., 2011) (Sirignano & Mehring, 2000). As this liquid sheet propagates with a growing instability, the oscillation overwhelms the balancing surface tension until a hole in the sheet is created (Dombrowski & Fraser, 1954) (Fraser, et al., 1954). Once a hole is created, surface tension then pulls this edge back thus concentrating the fluid into a roughly cylindrical mass, or ligament (Taylor, 1959). This ligament is again subject to instability creating droplets. An example image of sheet breakup is shown in Fig. 2 below.

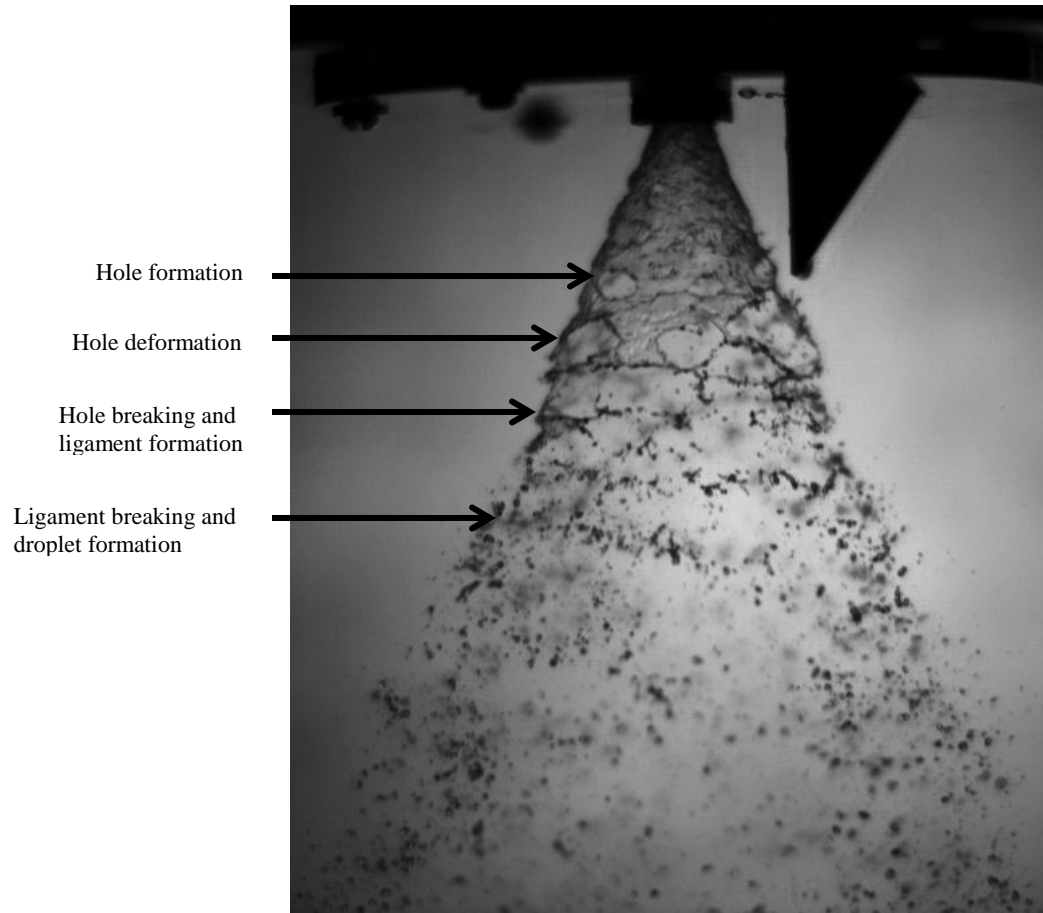


**Figure 2: Picture illustrating hole formation, hole breaking, ligament formation, and ligament breaking and droplet formation.**

One area of recent research is on the interaction and merging of two liquid sheets in atomizing processes (Sivakumar & Raghunandan, 1998) (Soltani, et al., 2005). Their findings have shown that the breakup length of the combined spray is largely dependent on sheet stability prior to mixing and that properties such as spray cone angle, disintegration distance, and mass distribution are all functions of sheet characteristics prior to mixing. However, much work has yet to be performed on quantifying the merged spray characteristics (Sivakumar & Raghunandan, 1998).

Another area of research in coaxial injectors is on the controlled mixing of the propellants prior to injection into the combustion chamber. In a coaxial injector, both propellants are injected tangentially through fluid holes creating a pair of spinning vortices. A recess internal to the injector geometrically binds the radial propagation of the vortex against a flat wall and increases mass and energy transfer between propellants through shear forces. Several studies have investigated this geometrical dependence in gas-liquid injectors with mixed results. Some findings have found that larger recesses and increased internal mixing leads to improved atomization as well as increased evaporation of larger droplets (Mayer & Tamura, 1996), while others have found that wave amplitudes at the injector exit of a long recess segment are smaller than that of a short recess, thereby increasing breakup length (Kim, et al., 2007). Further, work that has preceded this on swirl recess length has mainly focused on the fluid interaction between sheets and the influence on bounded or unbounded mixing along the axis of injection. This work looks to investigate a hybrid mixing geometry where the spray can be bounded linearly or at angles similar to the internal spray cone angle.

## **Chapter 3. Experimental Setup**

### **3.1 Objectives of Laboratory Setup**

Non-invasive techniques are crucial in understanding highly sensitive flow phenomena in atomizing sprays. Even minimally invasive measurement techniques such as force and pressure transducers can alter the “true” flow characteristics irreversibly, potentially leading to inaccurate data and conclusions. In order to avoid such effects, non-invasive optical and X-ray imaging techniques were utilized in the current work.

Another factor that was emphasized in the experiments performed was repeatability in the flow conditions while utilizing the different techniques. All flow conditions studied were measured using standard gauges, and point measurements were taken using coordinates relative to the spray exit from the nozzle. Furthermore, standard laboratory-grade fluids were used in the analysis and ambient exit conditions were ensured for all aspects of the study.

### **3.2 Data Collection Devices**

#### **3.2.1 High Speed Imaging**

To qualitatively measure spray breakup characteristics, high speed images were taken of the spray at speeds exceeding the high-speed flow phenomena occurring in the atomizing spray. This data was collected using a Photron FASTCAM SA5 camera mated with a f/1.2 lens. The FASTCAM SA5 camera utilizes a 12-bit ADC sensor with a 20  $\mu\text{m}$  pixel size. The shutter for the camera is an electronic shutter with a range between 16.7 ms to 1  $\mu\text{s}$  independent of the frame rate (Photron USA, INC). For each flow scenario, 250 images were

taken at both 12 kHz and 20 kHz. Images recorded at 12 kHz were collected with 896x816 resolution while images recorded at 20 kHz were collected with 706 × 632 resolution. All images were saved as Tiff files for transferability across different software platforms. To ensure accurate data, adequate time was given to ensure thermal equilibrium was reached in the camera before data was collected. Additionally, 10 dark current images were collected with the lens covered for each flow case to allow subtraction of baseline electronic noise from each image. A schematic of the laboratory setup is shown below in Fig. 3.

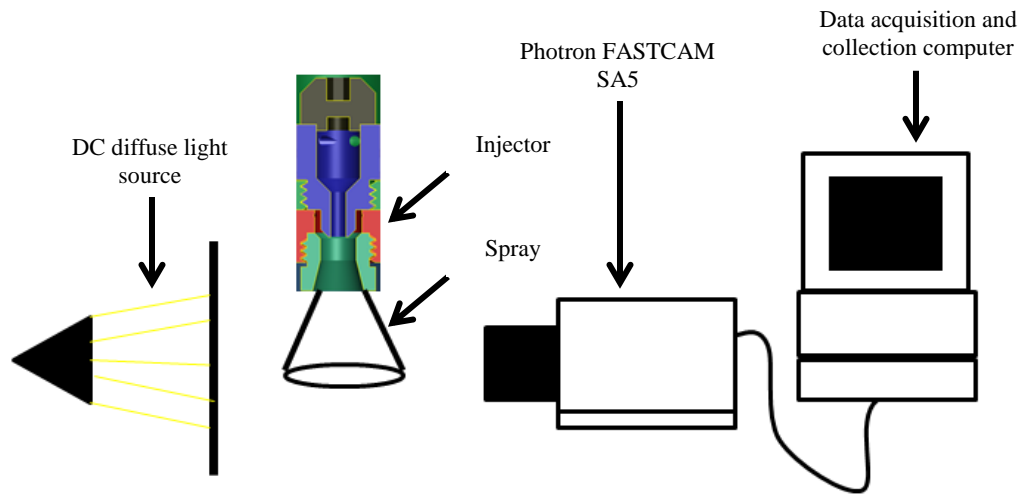


**Figure 3: Setup for high-speed imaging.** A Photron FASTCAM SA5 was used to image spray breakup. A DC light source was used to ensure a diffuse background.

### 3.2.2 Phase Doppler Particle Analyzer: Setup

To collect simultaneous droplet size and velocity measurements, a Phase Doppler Particle Analyzer (PDPA) was used. The Phase Doppler Particle Analyzer consisted of a Spectra-Physics Sabilite 2017, 6.0 Watt Argon laser, a Fiberlight™ Multicolor Beam Separator, a TSI model PDM1000 Photodetector Module, a TSI Model FSA 3500/4000 Signal Processor, and a TSI PDPA Receiver and Transmitting Probe. The data was routed via

firewire to a desktop computer and operated using the TSI FlowSizer™ software. A schematic of the laboratory setup is shown in figure 4 below.

The Spectra-Physics Sabilite 2017 laser was capable of emitting 1.5 Watts of power at 488.0 nm and 2.0 Watts of power at 514.5 nm. The emitted beam diameter was 1.4 mm with a 0.5 mrad divergence at 514.5 nm and with an optical noise less than 0.5% rms (Spectra-Physics, 2002). The emitted laser beam is then sent into a Fiberlight™ Multicolor Beam Separator. Inside the beam separator, the laser passes through a Bragg cell where the angle of the cell and power levels are set to produce two equal-intensity beams; one is unshifted in frequency and the other variably downshifted by 40 MHz. Next, the 2 beams are sent through a dispersion prism where they are separated by color and then steered and focused into a Fiberlight™ beam coupler. The power output as a percentage of laser power is between 80-90% for this process (TSI INC., 2005). The light is then sent via fiber-optic cables and emitted through the transceiver probe. The light emitted through the transceiver is roughly 50-65% of the emitted laser power (TSI INC., 2005).

Once the light is sent through the transceiver, it is focused to a probe volume where it forms an interference fringe pattern. When the interference pattern interacts with droplets, the refracted signal is recorded by the receiver. This signal is then sent to the Model PDM 1000 photodetector module where the optical signal is converted to an electronic signal and then recorded by the Model FSA 3500/4000 signal processor.

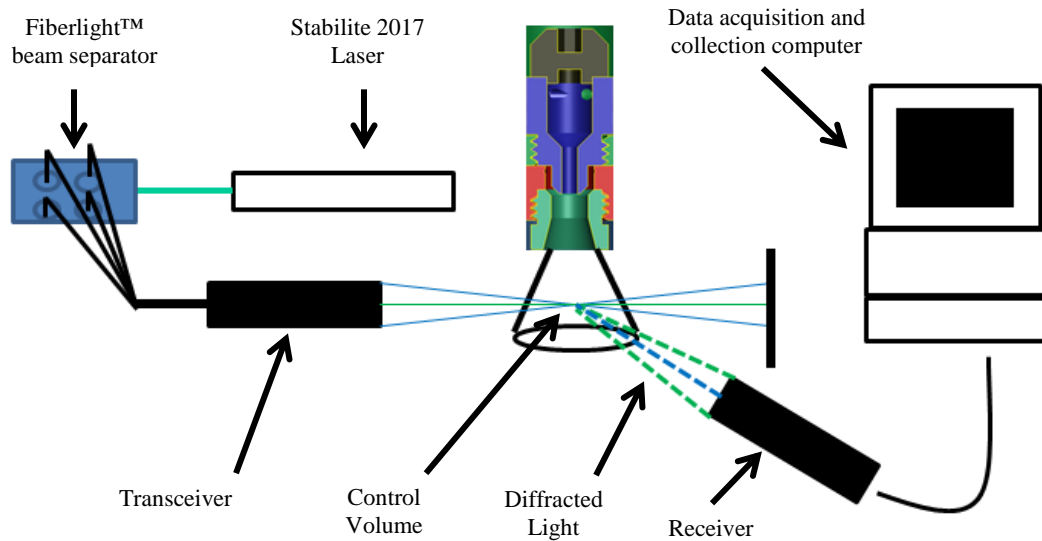


**Figure 4: PDPA system.** A Spectra-Physics Sabilite 2017 laser emits an Argon-Ion beam which is split in a Fiberlight™ beam separator and then emitted through a transceiver probe. Atomized drops refract light which is recorded at the receiver and processed.

### 3.2.3 Phase Doppler Particle Analyzer: Processing

One of the most fundamental aspects of PDPA is the spherical droplet assumption used for particle sizing. Since atomizing sprays have a variety of droplet sizes undergoing varying stages of droplet breakup, it is not realistic to assume that all droplets passing through the probe volume are spherical. Therefore, post processing of received signals must be performed to verify that droplets recorded are in fact spheres. This is performed through phase validation and intensity validation.

Phase validation is a process to verify a signal received at the receiver is actually a spherical drop. This is done by using 3 detectors spaced at different intervals to record the signal intensity of the refracted fringe pattern as well as its phase at the detector. By measuring the intensity value of the incoming signal at three points, signal hit rate can be improved and signal values can be verified at three independent sensors. Further, by having two sensors separated by a small distance  $AB$ , and a third separated a larger distance  $AC$ , the

change in phase of light measured at AB,  $\varphi_{AB}$ , can be compared to the phase change in light between AC,  $\varphi_{AC}$ . Since the change of phase between A and B is encompassed in the change between A and C and the spacing between the sensors is known, the sensors produce two pairs of redundant measurements that can be weighted according to their relative sensitivities and averaged to obtain the mean phase value for the particle (TSI INC., 2005).

The second method used in signal validation is called intensity validation. The main purpose of intensity validation is to help correct for probe volume bias and mixed mode scattering. Probe volume bias is the bias in the preferential detection of large particles. This stems from the fact that scattered light is proportional to diameter squared. Therefore large particles can scatter light on the edges and throughout the probe volume whereas small particles can only scatter enough light to be detected when passing through the center of the probe volume. One technique often used to help mitigate this effect is called intensity validation. Intensity validation involves setting a maximum and minimum intensity limit of refracted radiation and correlating those values with an expected value of diameter for a particle refracting that much light (TSI INC., 2005). By imposing this condition, the software rejects signals that may have been reflected or stem from multiple particle events. These events could manifest as a small droplet with an unrealistically large intensity value or a very large particle with a very low intensity value.

### 3.2.4 X-ray Setup

X-ray computed tomography scans were taken at the Iowa State University X-ray Flow Visualization Facility. The X-ray source utilizes twin LORAD LPX200 portable sealed-tube sources positioned at right angles on a rotating ring. The supply current and

voltage can be adjusted from 0.1 to 10 mA and 10 to 200 kV respectively (Meyer, et al., 2008). Imaging is performed using a  $44 \text{ cm}^2 \times 44 \text{ cm}^2$  cesium-iodide scintillator screen allowing for visible light to be imaged using an Apogee Alta U9 CCD camera capable of variable exposure times at resolutions up to  $3072 \times 2048$  (Meyer, et al., 2008). Digitally reconstructed tomography is possible by taking a series of 360 radiographs at 1 degree of separation. These images can then be reconstructed using a 64 node LINUX cluster in the Iowa State Center for Non-destructive Evaluation.

Due to the low X-ray absorption cross-section of water, the water sprays were mixed with 30% by mass potassium iodide (KI) to increase image contrast. To ensure that the attenuation coefficient ( $\mu_m$  in Beer's law) is linear with the concentration of KI or equivalently the liquid path length ( $l$  in Beer's law), a cuvette study was performed for KI concentrations ranging from 10-50% with a 5 mm cuvette. A linear increase in the attenuation coefficient with KI concentration indicates that the effects of beam hardening are minimal. Beam hardening takes place when lower energy (softer) X-rays are completely absorbed and any additional KI or liquid in the remaining path freely transmits the remaining higher energy (harder) X-rays without any further absorption. In this case, the spectrum of the X-rays becomes harder as they pass through the liquid. This is a potential problem with the use of polychromatic tube-source X-rays and is not a problem when using narrowed synchrotron X-ray radiation. By ensuring that beam hardening (non-linear) behavior is not present from 10-50% KI in the 5 mm cuvette, it ensures that beam hardening will not lead to errors in relating X-ray absorption to the liquid mass, or equivalently liquid path length. Previous works have verified that the attenuation coefficient is linear with KI concentrations up to 15% for 1 cm path lengths (Meyer, et al., 2008). Hence, for one-half the liquid path

length of 5 mm, it is expected that beam hardening can be avoided with KI mass fractions up to 30%.

### 3.2.5 Absorption Coefficient Study

In order to increase contrast for X-ray absorption studies, KI was added to deionized water used in water flows. In order to verify that the absorption coefficient of KI is still linear vs. concentration in the range of path lengths between 2.5 - 5mm, a cuvette study was performed. The study was performed by mixing known concentrations of KI in cuvettes of known path length. The intensity of signal through the fluid medium could then be compared to the intensity of background signal allowing for an absorption coefficient to be calculated in accordance with Beers law.

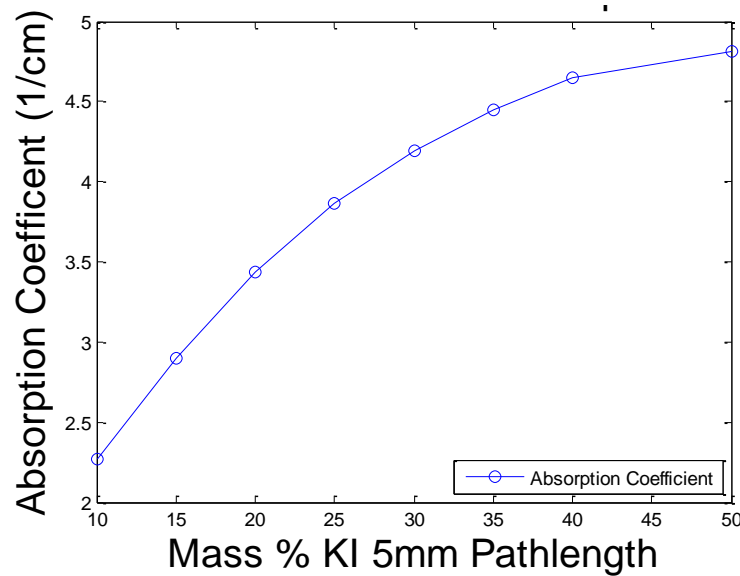


Figure 5: Absorption coefficient versus KI concentration.

As shown in Fig. 5, a slightly nonlinear dependence of the absorption coefficient is noted for KI concentrations ~30% for pathlengths up to 5 mm, indicating that so-called beam

hardening may be taking place. Since the spray at hand has an estimated sheet thickness closer to 1 mm, a 30% solution is assumed to absorb with minimal beam hardening.

## Chapter 4. Results: Effects of Injector Geometry and Injection Pressure

### 4.1 Overview

A series of high speed images of water atomization were collected at different injection pressures and over 5 different geometric parameters. For each injection pressure, 250 images were taken at both 12 kHz and 20 kHz. 12 kHz images were recorded at  $896 \times 816$  resolution and images taken at 20 kHz were recorded at  $704 \times 632$  resolution. A comparison for different liquids was also conducted, including acetone, methanol, and JP-8. The images were then post processed for dark current removal and digital filtering.

### 4.2 Image Processing

Before the images were analyzed, they were digitally post-processed in Matlab. The first step in post processing was removing baseline electrical noise emitted by the camera. To do this, images were collected on the high speed camera between runs with the lens cap blocking all incident visible radiation. These dark images were then subtracted from spray images used for data analysis. Next, the images were median filtered for noise removal and sharpened to increase contrast. Figure 6 shows examples of the unprocessed and processed images, with the processed image showing improved contrast.

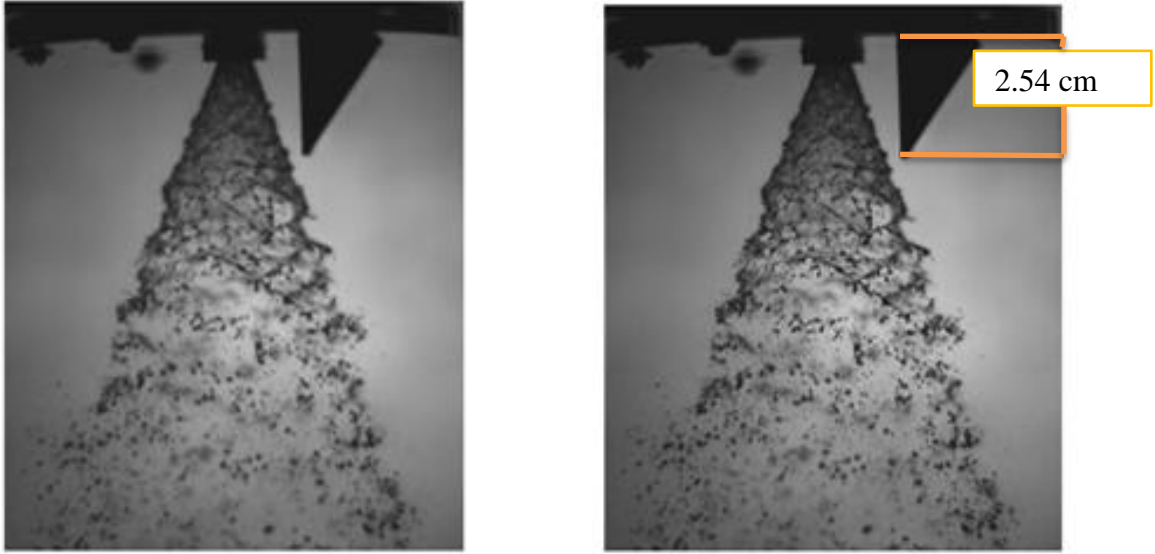


Figure 6: Comparison between unprocessed image on left compared to post-processed image on right.

### 4.3 Investigation of Recess Designs

An investigation into internal mixing was performed using high speed imaging. To perform this investigation, a series of photographs was taken of the spray at the nozzle exit for the 5 different recess designs. The recess design is shown schematically in Fig. 7. Each recess design contains 4 adjustable parameters: cylindrical inner diameter  $D_i$ , cylindrical length  $L_c$ , trumpet length  $L_t$  and trumpet or exit half angle  $\theta$ . For each of the 5 different geometries studied here, the injection pressure was varied from 69 kPa (10psi) – 620 kPa (90 psi) in ~69 kPa intervals. Images were taken at two frame rates with the maximum resolution available.

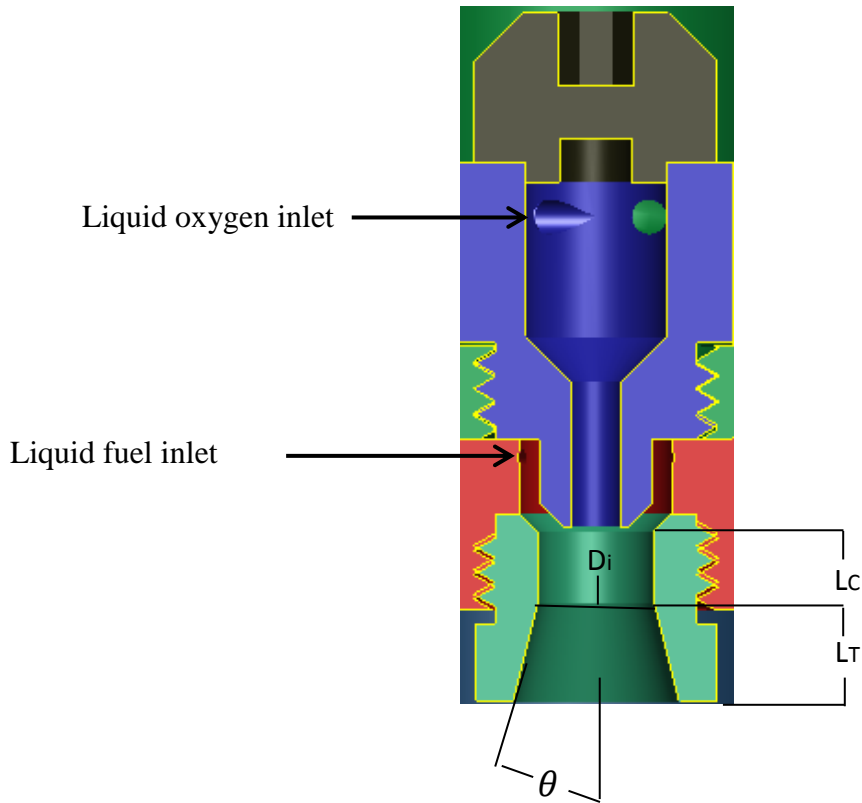
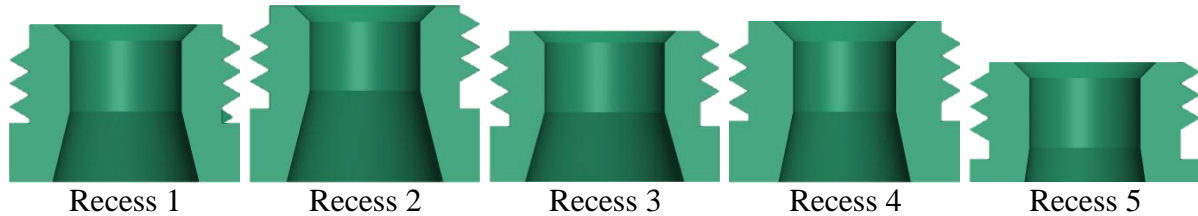


Figure 7: Cross section of swirler with 'Recess Design' dimensions shown.

As is shown in Fig. 7, the liquid fuel and oxidizer enter through tangentially drilled holes creating a pair of swirling vortices. These vortices then propagate through the injector and mix before being injected into the combustion chamber. By increasing the residence time of internal mixing prior to injection, momentum transfer and mixing is increased. However, increasing residence time beyond a certain value could lead to increases in frictional forces that could significantly reduce exit velocities to the point that the spray breakup can become non-uniform. An ideal geometry is desired that promotes internal mixing while producing a uniform distribution of finely atomized drops.

In the study performed, various bound mixing lengths and exit half angles were studied to see if an ideal exit length and exit half angle could be found. To the author's best knowledge, the combined effect of stream-wise mixing length in combination with varied

exit half angle has not been studied. Based on the study at hand, the effects of geometric parameters on liquid sheet stability, droplet size, and droplet distribution are analyzed. The geometries of the different recess designs are shown below in Fig. 8.



**Figure 8:** Scaled images of the different recess designs are shown above. Values for varied parameters can be seen in Table 1. Recess designs are numbered as 1 at far left to 5 at far right.

As shown in Table 1, five different recess designs were analyzed using high speed imaging to compare effects on break-up and atomization.

**Table 1: Recess Design Parameters.**

Recess Design #	$D_i$ (mm)	$L_t$ (mm)	$L_c$ (mm)	$\theta$
1	6.1	3.81	3.81	14
2	6.1	5.08	3.81	14
3	6.60	3.81	3.81	15.7
4	5.59	3.81	3.81	12
5	6.1	1.91	3.81	8.5

## 4.4 Effects of Varying Recess Design and Injection Pressure

### 4.4.1 Overview on Effects of Recess Design

By dictating several geometrical features relevant to internal momentum transfer, the exit conditions of the flow are expected to change noticeably. As noted earlier, each recess design contains 4 adjustable parameters: cylindrical inner diameter  $D_i$ , cylindrical length  $L_c$ ,

trumpet length  $L_t$  and trumpet or exit half angle  $\theta$ . In this study, the cylindrical diameter is varied from 5.59 mm to 6.60 mm with the intended effect of controlling internal radial momentum during the initial mass transfer and mixing. Because a nearly constant mass flow rate and injection pressure was ensured for each recess design, the momentum of all fluids is nearly identical. Consequently, by decreasing the diameter, it is expected that the fluid will have an increased radial and tangential velocity. Of significant consequence, a higher tangential velocity is expected to increase the observed centrifugal force which will work to decrease fluid perturbations by increasing the force which binds the fluid against the recessed design segment. The result of this is an expected increase in stability of the fluid sheet at the exit of the nozzle. The cylindrical length,  $L_c$ , governs internal residence time and is varied by a factor of 2.6 in the study. By controlling residence time, momentum transfer and mixing can be controlled. By increasing residence time, the merging vortices are expected to homogenize and become more acoustically stable. Finally, the trumpet angle is varied by 7.2 degrees in the study. The intended goal of the trumpet length is to provide additional residence time for mixing and momentum transfer while maintaining a proper velocity vector from the injector into the combustion chamber to control droplet distribution outside of the injector.

#### **4.4.2 Discussion of Results at Low Injection Pressures**

All recess design combinations were imaged with water flows at inlet pressures between 69 kPa (10 psi) to 620 kPa (90 psi) in 69 kPa increments. A series of images for

Recess Designs 1-5 and varying pressure can be found in Appendix A. For the purposes of discussion, only illustrative images are included in this discussion.

At low injection pressures (<140 kPa), significant distinctions between atomization of differing recess designs were noticed. It is anticipated that low velocities and, consequently, low Weber numbers allow for stable sheet formation and longer time scales before sheet breakup induced by aerodynamic instability. Indeed, this increased stability at low pressures can be seen prominently by the extended sheet formation of Recess Design 4 in Fig. 9 (left), which provides evidence of exceptional sheet stability. The atomizing fluid from Recess Design 4 maintained continuity in excess of 6 cm from the injector exit which can be contrasted to Recess Design 5, shown in Fig. 9 (right), in which instability, hole growth, and droplet formation occurred within 1.5 cm from the injector. Note that the exit half angles are also somewhat different (12 degrees for Recess Design 4 vs. 8.5 degrees for Recess Design 5); however, because of the short trumpet length for Recess Design 5, it is likely that the exit half angle would not play as significant role in the differences observed here as the differences in the trumpet length. It is also possible that the smaller inner diameter for Recess Design 4 leads to more stable sheet formation than for Recess Design 5.

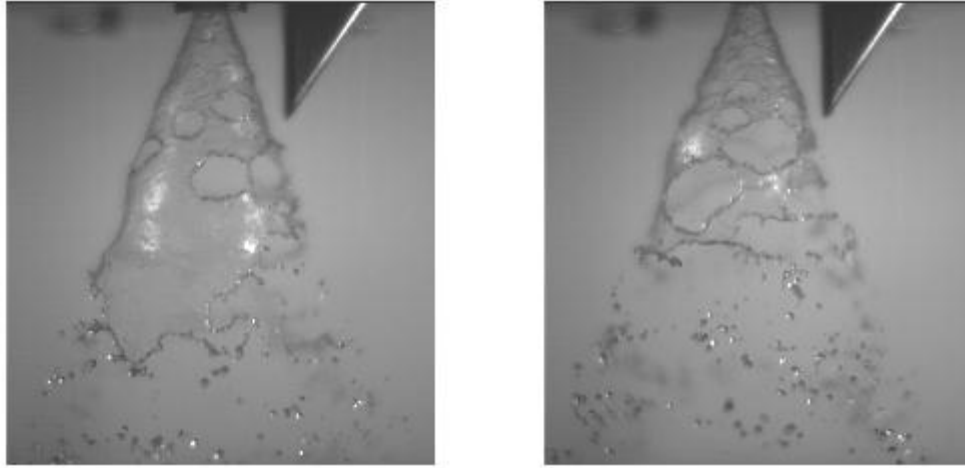


**Figure 9: Exceptional sheet stability demonstrated for Recess Design 4 at the lower injection pressure of 69 kPa psi (left) and large-scale oscillations with heterogeneous breakup visible for Recess Design 5 at 69 kPa (right).**

The atomization of Recess Designs 1, 2, and 3 at low (<140 kPa) pressures also exhibited stable sheet formation, propagation, and ligament breakup. Typical images are shown in Fig. 10 below. Interestingly, Recess Design 3 with the largest inner diameter shows the fastest breakup, consistent with the trend for Recess Designs 4 and 5.

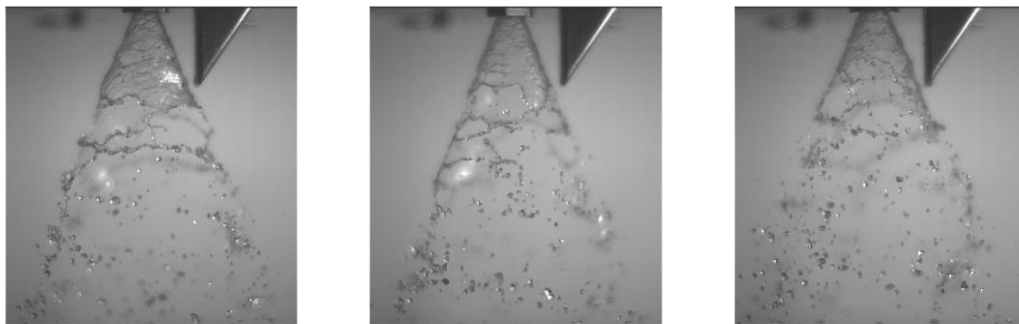


**Figure 10: Stable sheet formation with uniform droplet breakup and distribution indicate stable low-pressure atomization for Recessed Design 1, 2 and 3 (left to right).**

### 4.4.3 Discussion of Results at High Injection Pressures

As injection pressure was increased, the breakup length and time scales decreased as expected. However, the breakup length of Recess Design 4 continued to produce sprays with noticeably longer sheet stability than the other injectors. Similarly, the mass distribution of Recess Design 5 was quite poor with large heterogeneous ligament formation. Recess Designs 1, 2 and 3, however, exhibited very consistent and uniform sheet breakup indicating proper and balanced mixing. This uniform breakup became very noticeable as pressures were increased in excess of 350 kPa, and aerodynamic breakup became the dominating breakup mechanism. A comparison of Recess Design 3 (proper mixing) and 5 (improper mixing) is shown in Fig. 11 below.

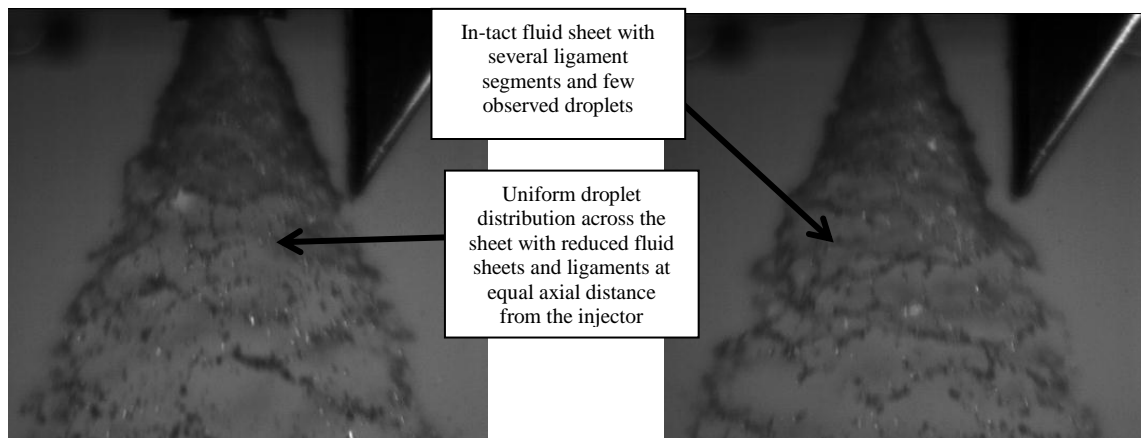


**Figure 11:** A comparison between Recess Design 3 (left) and Recess Design 5 (right) at 344.7 kPa. Recess Design 3 exhibits faster and more uniform atomization. This is observed in the existence of stable fluid sheet segment at increased axial locations

### 4.4.4 Discussion on spray cone angle and sheet stability

While visible wave growth and observed droplet distribution are helpful qualitative observations, quantitative results would also be desired. For stable combustion over a range

of throttle conditions, it is desirable for mass distribution to remain relatively fixed while flow rate is varied. One helpful indicator of combustion stability of a range of thrust levels is spray cone angle. The spray cone angles have been calculated for each recess design below.

**Table 2: Spray cone angles for recess length designs.**

Pressure (kPa)	Spray cone angle, degrees from vertical				
	1	2	3	4	5
69	23	21.7	25.5	22	21.7
137.8	23.5	21.3	24.5	22.7	23
206.8	24.1	22.5	23.6	22.5	22.5
275.8	25.1	22.2	22.9	22.3	23.3
344.7	23	22.5	22.4	22.3	21.6
413.7	23.5	22.9	22.5	22.3	21.3
482.6	22	21.8	22.6	22.4	21
551.1	22.3	21.3	22.2	22.2	21.2
620.5	20	21.1	22.5	22.3	21.2

Based on Table 2 above, several trends are visible indicating geometric correlations. Firstly, Recess Design 4 exhibited little variance in spray cone angle over almost the entire range of parameters, in contrast to Recess Designs 1 and 5, which exhibited significant deviations over a range of pressures. It can also be seen that Recess Designs 2 and 3 vary slightly during low pressures stabilize as pressure is increased. This conclusion indicates that the mixing between fluids is sensitive to both cylindrical length and cylindrical inner diameter and that this sensitivity varies with pressure. It also indicates that the stability of internal mixing varies among the different injector designs and merits additional investigation.

#### 4.4.5 Discussion of Geometric Factors on Breakup and Atomization

By varying the geometry internal to the injector, mixing and atomizing properties that are largely dependent on the internal geometry are hoped to be better understood. The injector studied was designed to allow for specific geometric parameters to be varied, allowing for isolated geometrical correlations to be determined. To help isolate the geometrical parameters relevant to atomization, dimensional and non-dimensional properties were analyzed.

Dimensionally, the internal Diameter,  $D_i$ , cylindrical length  $L_c$ , trumpet length  $L_t$  and trumpet or exit half angle  $\theta$ , were all changed to allow for variations in flow conditions to be studied. After analyzing the high speed images, several quantifiable parameters related to atomization and spray breakup were investigated, including breakup length, breakup type, and apparent stability.

The first parameter studied was breakup length, alluded to earlier. In our study, breakup length was quantified as the distance from the injector that the spray had evolved into a visually uniform distribution of droplets. After analyzing each set of 250 images, it was determined that Recess Design 3 exhibited the shortest breakup length and Recess Design 4 required the longest distance to fully atomize the spray. This is shown in Figure 12 below.

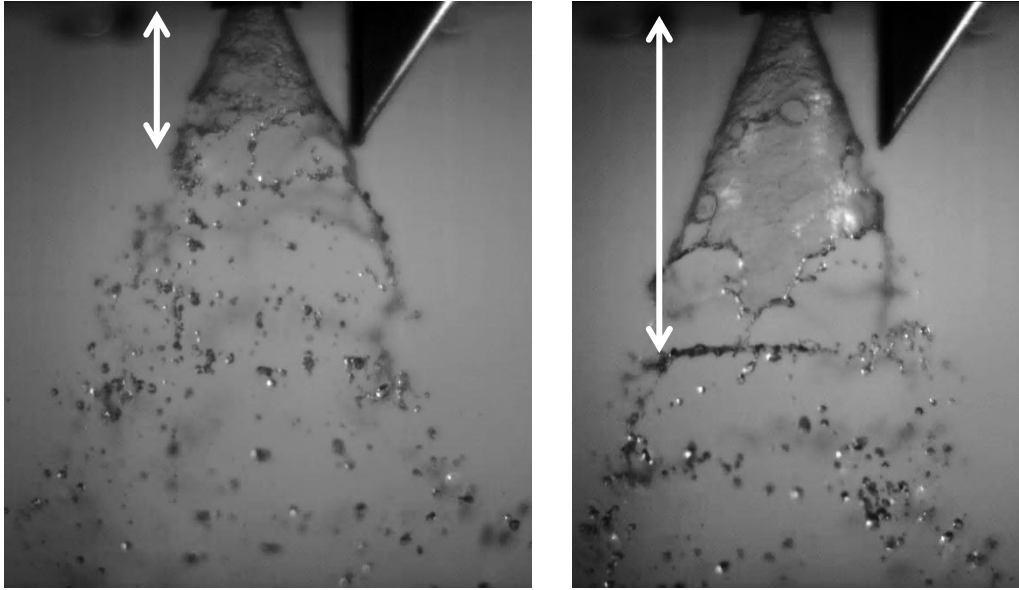


**Figure 12: Comparison between breakup length minimum (Recess Design 3 at left) and maximum (Recess Design 4 at right).**

By comparing this observed flow phenomenon to geometrical parameters, it can be seen that the internal diameter,  $D_i$ , is highest for Recess Design 3, and is lowest for Recess Design 4. Based on this observation, it is likely that a smaller diameter increases the tangential and axial velocities of the fluid, reducing the time available for the fluids to homogenize. Additionally, it is likely that this increase in radial velocity also helps to dampen surface oscillations of the fluids internal to the injector on the unbounded fluid surface. This combination creates for a spray sheet that has increased homogeneity and less surface instabilities.

The next parameter studied was the breakup type. The breakup type parameter is classified as the predominant deterioration mode observed during the atomization of the liquid sheet. The breakup type can further be characterized as the mode at which instabilities cause droplet formation to occur. In some sheets, it was observed that localized instabilities created many holes that grew, merged, and then disintegrated into droplets. In other sheets, it

was observed that liquid ligaments were formed directly from the fluid sheet or from local hole growth. This latter mechanism showed very little transition from hole formation to droplet formation. The physical mechanism causing the difference in breakup mode can be related to global instability wave growth on the sheet causing direct ligament formation as compared to local instability causing hole growth.

This parameter was characterized by evaluating many high speed images and indicating, on average, the dominant breakup mode. The difference in observed breakup mode was then used to determine if droplet formation was dominated by global ligament detachment from the sheet or due to droplet formation from hole merging and combined breakup. As hole growth was observed to some degree in all cases, this comparison is intended to delineate significant observable trends rather than precise values. Examples of the breakup modes leading to droplet formation are shown in Fig. 13 below.

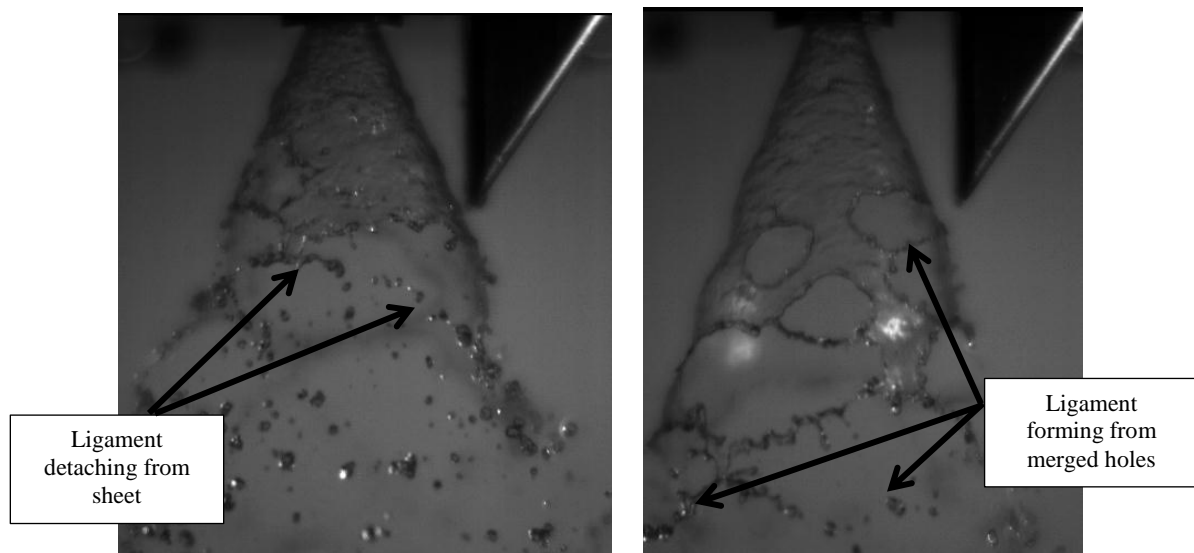


**Figure 13: Comparison between ligament forming from the liquid sheet (left) and widespread hole merging induced droplet breakup (right).**

After ranking values, it was discovered that in the experimental range between half angles of  $8.5^\circ$  and  $15.7^\circ$ , a larger half angle correlated to breakup dominated by ligament detachment from the sheet, while smaller half angles indicate breakup dominated by hole growth. It is hypothesized that this relationship is due to the global Kelvin-Helmholtz instability introduced onto the combined liquid sheet as the fluid propagates from the conical cylindrical diameter section, onto the angled trumpet section. By increasing this angle, the flow is distorted to a larger degree while simultaneously creating a global oscillation frequency as the combined sheet rebounds over the angle. This would be in contrast to a small angle in which a global frequency would not be as dominant, and instability growth would be more localized due to aerodynamic shear stresses. As the recess design with the largest half angle coincided with the largest inner diameter (Recess Design 3), it is possible that there is a synergistic effect between these two parameters leading to improved breakup.

#### **4.4.6 Recess Design Conclusions**

Based on high speed imaging, it was evident that geometric parameters controlling momentum diffusion and mixing residence time play a significant role in droplet distribution and breakup scales. Recess Design 4 exhibited very minimal variance in spray cone angle and exhibited exceptionally stable sheet propagation. This indicates uniform mixing and equilibrium internal to the injector, creating a fluid sheet with few initial perturbations that would lead to sheet breakup. While the trumpet half angle of Recess Design 4 is less than Recess Designs 1, 2 and 3, predictably producing a more stable sheet dominated by hole formation and merging, it should be noted that Recess Design 5, which was characterized by significant oscillations in its liquid sheet, had a smaller trumpet half angle than Recess

Design 4. However, because the trumpet length of Recess Design 5 is nearly half that of other Recess Designs, it is anticipated that this trumpet half angle may not have as significant an effect as was observed for Recess Design 5.

High speed images also indicated that Recess Design 3 exhibited the most consistent visually observed droplet distribution among the different designs. With this noted, an interesting comparison can be made between Recess Design 3, which had the largest cylindrical diameter, shortest breakup time scales, and most efficient droplet formation, to Recess Design 4, which had the smallest cylindrical diameter and exhibited poor breakup and atomization. However, it should also be noted that while those qualities are quite contrasting, Recess Designs 3 and 4 also exhibited the most stable spray cone angles for the range of pressures. It can also be seen that Recess Designs 3 and 4 have identical cylindrical lengths and trumpet lengths with significantly differing cylindrical diameters.

## Chapter 5. Results: Effects of Fluid Properties and Injection Pressure

A study was performed to compare spray atomization and breakup of the liquid-liquid swirl co-axial injector using different fluids. In this study, the breakup and atomization of methanol, acetone, Jet Propellant-8 (JP-8), and distilled water were recorded and analyzed using high-speed imaging and PDPA for a standard geometric injector setup using Recess Design 1. All images were again post processed using Matlab, as described previously.

### 5.1 Fluid Properties

Current research indicates that the breakup of liquid-liquid swirl co-axial injectors is largely dependent on Weber number and sheet thickness (Kim, et al., 2007) given as:

$$We = \frac{\rho u^2 h}{\sigma} \text{ and } h = 2.7 \left[ \frac{d_o \dot{m} \mu}{\rho \Delta P} \right]^{.25},$$

respectively where  $\rho$  is density,  $u$  is a characteristic velocity,  $h$  is a characteristic sheet thickness,  $\sigma$  is surface tension,  $d_o$  is a characteristic injection diameter,  $\dot{m}$  is mass flow rate,  $\mu$  is viscosity and  $\Delta P$  is pressure drop throughout the injector. Since the relevant pressure drop is not known, the sheet thickness will be estimated using high-speed images to capture the sheet velocity and inferring the sheet thickness from the mass flow rate (assuming the fluid density is known and constant). Other fluid parameters in these equations are defined in Table 2 below.

To investigate the effects of fluid properties in terms of these parameters, fluids with significantly differing properties were studied using high speed imaging and PDPA. High speed images were collected between 34 and 482.6 kPa and PDPA measurements were collected between 103 and 344 kPa. The fluid properties were chosen so that trends could be

inferred for spray characteristics of liquid oxygen and a wide range of liquid hydrocarbons that are of significant interest for rocket applications.

**Table 3: Fluid properties and dimensional parameters.**

Fluid	Water	Methanol	Acetone	JP-8	Liquid Methane
Surface Tension, $\sigma$ (N/m)	0.073	0.023	0.023	0.027	0.014
Density, $\rho$ (g/cm <sup>3</sup> )	1.000	0.791	0.791	0.805	0.425
Dynamic Viscosity, $\mu$ (Pa*s)	0.001	0.001	0.000	1.610	0.000
$\rho/\sigma$ (unit Weber number for fixed velocity)	13.74	34.85	34.69	29.82	30.34
$\rho/\mu$ (unit Reynolds number for fixed geometry and velocity)	1124	1454	2585	0.500	3500
$(\mu/\rho)^{0.25}$ (sheet thickness of Lefebvre (Kim, et al., 2007))	0.173	0.162	0.140	1.189	0.130

## 5.2 Survey of Images Varying Fluid Properties and Injection Pressure

To collect quantitative data regarding spray breakup and atomization of different fluids and to quantify the effects of fluid properties on injection and atomization from swirl-swirl injectors, high-speed images were collected for acetone, methanol, JP-8, and water at injection pressures of 34.5, 69.0, 137.9, 206.8, 275.8, and 344.7 kPa at 12 kHz, and at injection pressures of 413.7 and 482.6 kPa at 20 kHz. A complete collection of these images can be seen in Appendix A.

### 5.2.1 Results: High Speed Images Varying Fluid Properties and Injection Pressure

An analysis of high-speed images collected of liquid atomization and spray breakup with varying fluid properties and pressures was performed. These results indicate that

different fluid properties can be shown to have a specific impact on spray breakup and atomization. The work looks to quantify the atomization for potential use of liquid methane; consequently, fluid properties were selected such that potential spray characteristics of methane breakup could be inferred.

As was shown with the survey of Recess Design geometries, low injection pressures allow for quantification of flow phenomena with little aerodynamic induced instability. Additionally, because of the low injection pressure, flow phenomena occurring within the spray occurs at slower rates allowing for easier identification. Specifically, both small-scale and large-scale instability waves propagate at lower speeds, allowing for increased visual identification. This is shown in Fig. 14.

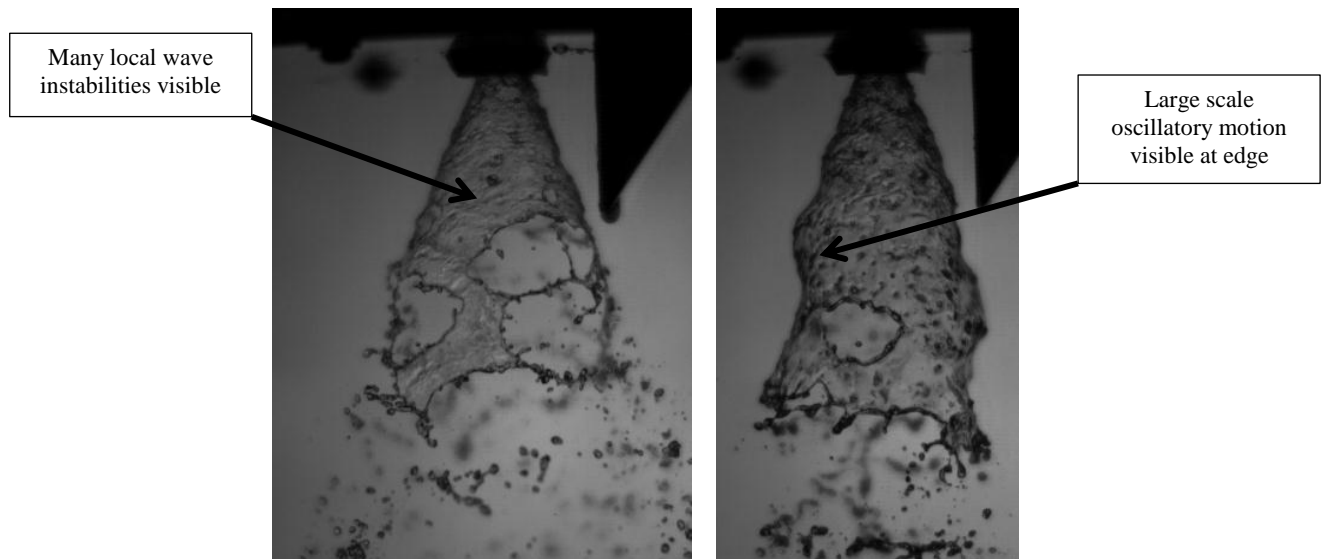


**Figure 14: A comparison showing visible small-scale instability at left and large-scale instability propagation at right. Fluids are acetone at left, and JP-8 at right. Both are injected at 34.47 kPa and imaged at 12 kHz.**

What is also evident at low pressures is the collapse of the fluid sheet into a cone and further into a closed hollow oval. This flow phenomenon is likely due to initial outward

radial velocities succumbing to contraction of the fluid sheet due to surface tension. An image of this flow phenomenon is shown below.

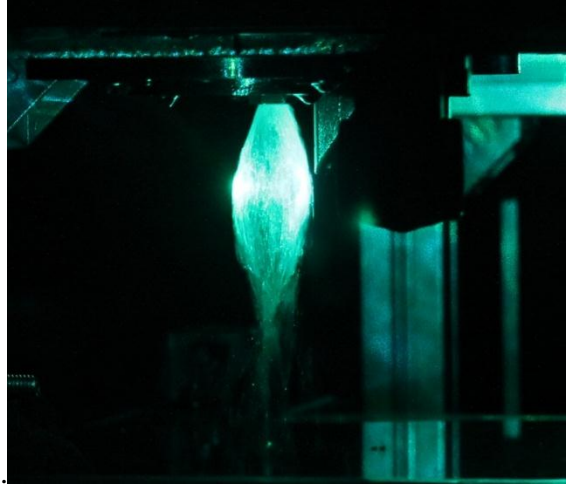


**Figure 15: Closed rim flow illuminated with argon-ion laser showing refracted light internally reflecting interior to the cone.**

As injection is increased to 69.0 kPa, spray cone angles fully develop allowing for more accurate comparisons to be made between injected fluids. One of the first differences between fluids is in the breakup type previously mentioned in the Recess Design survey. As mentioned previously, breakup type can be characterized by either a dominating global instability or local instability mode which leads to droplet formation. A comparison between global instability breakup and local instability breakup is shown below.

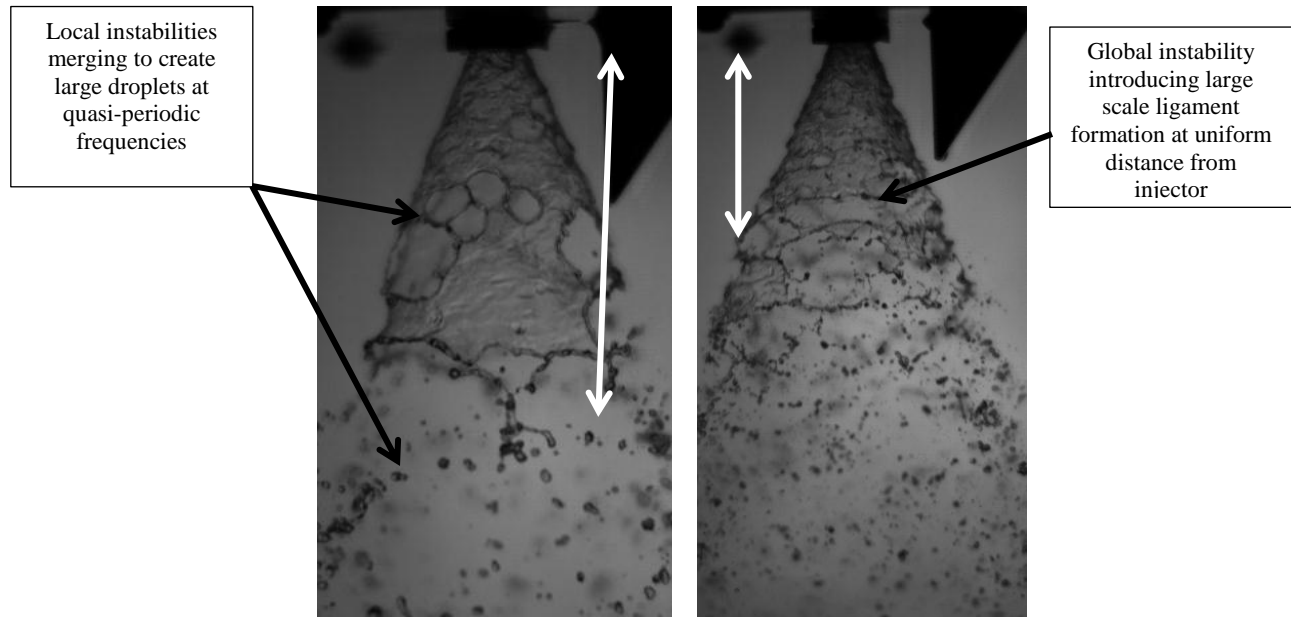


**Figure 16: Comparison between global and local instability wave propagation and droplet formation. Injected fluid at left is Water and Methanol at right.**

The images shown in Fig. 16 also shed light on the differences between the fluids. In the image of water, little global instability can be seen as indicated by the heterogeneous location of droplets within the fluid sheet. However, uniform dislocation of fluid ligaments indicate a global instability appears to be the dominating mode for breakup in the image at right. Since the geometrical parameters are constant for the fluids, differing fluid properties must lie at the root of the difference. A hypothesized explanation of the difference is that as the fluids are propagating through the cylindrical section of the Recess Design and into the angled trumpet section, the flow over the angle introduces a discontinuity in the boundary layer. For each fluid, this discontinuity is damped by the surface tension in the fluid, creating a rebounding effect. However, since the surface tension of the methanol is almost 4 time less than that of water, the oscillation is damped considerably less. The result of this is that instability growth around this corner creates a significantly larger effect on the instabilities

present in the liquid sheet at the injector exit. Similar global flow instability is also present in both acetone and JP-8, all of which have considerably smaller surface tension values compared to water. This result indicates that liquid methane, which has a surface tension value almost half of that as methanol and acetone, would exhibit even larger global instability. This would manifest in periodic and uniform ligament and droplet breakup.

Further evaluation of differences between fluids can be drawn by further isolating the number of different fluid parameters and studying the observed differences. In this case, a comparison between JP-8 and Acetone is made. Both fluids have comparable surface tension, and global instability modes can be observed in each. However, as is shown in Fig 17. below, the breakup length for JP-8 is considerably longer than for acetone as observed by the average location of the last stable fluid ligament.

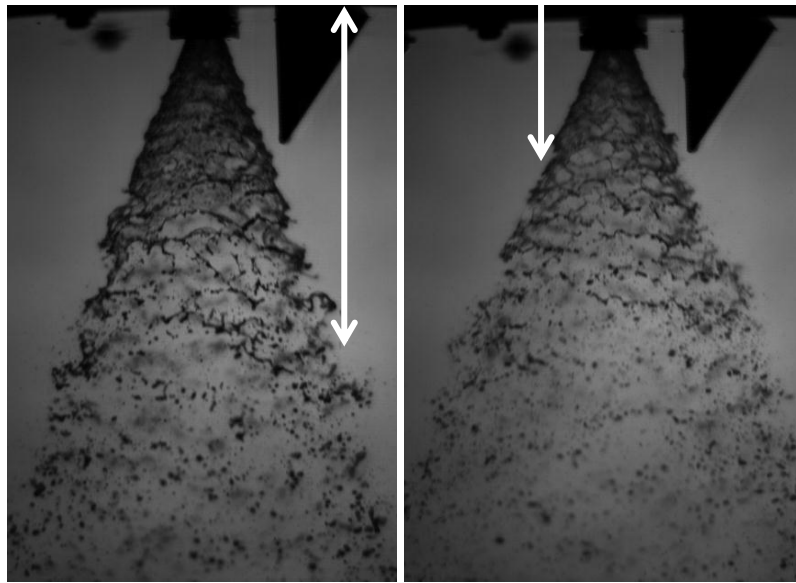


**Figure 17: Comparison in breakup length between JP-8 (left) and acetone (right) at 137.9 kPa.**

While the surface tension and injection pressure for both JP-8 and acetone are similar, the viscosity of JP-8 is considerably higher. Because of this, for flow rotating internal to the

injector, the Navier-Stokes equation for incompressible fluid predicts a larger boundary layer for the JP-8, effectively shrinking the cylindrical diameter,  $D_i$ , and, as was indicated in the Recess Design Survey, results in an increase in the average breakup length. Again, as before, this trend is shown among Acetone and Methanol which have comparable fluid properties allowing for hypothetical expansion to potential utilization with Methane.

### 5.3 PDPA Data Collection and Processing

In order to quantify droplet size and velocity statistics, PDPA was performed on the injector while varying fluid properties and injection pressure. PDPA data was collected in 3 horizontal slices across the atomizing liquid sheet. Based on high-speed images, it was inferred that horizontal slices closer than 25 mm to the injector would not reveal accurate flow structure because of a large percentage of the flow would still be entrapped in stable liquid sheet structures that had not atomized, particularly at low pressures. It was then inferred that slices at 50 mm and 75 mm from the nozzle exit would effectively quantify differences in atomization evolution. It was anticipated that finely atomized sprays would have higher droplet counts and wider distributions of diameters and velocities, while sprays still atomizing would produce larger droplets still in the process of breaking up. A schematic of the data collection locations is shown in Fig. 18 below.

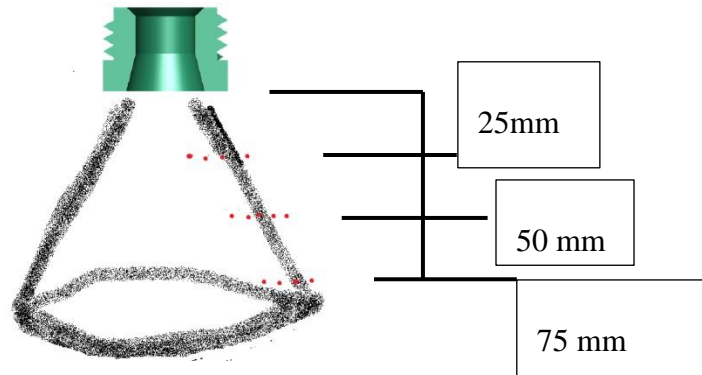


**Figure 18: PDDPA data collection locations.**

The values recorded using the PDDPA system were subject to intensity validation to reduce probe volume bias and false and reflected signals. They were then output as CSV files and loaded into Matlab for post processing.

One of the major points of interest in this study is to understand droplet size distributions, along with droplet velocities at specific locations throughout the spray. Data was collected at several injection pressures to fully characterize droplet breakup evolution for 4 different fluids to further develop understanding of the physical parameters driving droplet breakup and atomization.

To maintain high spatial accuracy, a two-dimensional adjustable steel truss system was built as the platform for stably mounting the injector. In addition to damping out vibrations, adjustable rails allowed for accurate and repeatable vertical placement in the spray and prevented movement of the spray into and out of the convergence volume of the 4 incident beams. The placement of the point measurements along the rail was achieved using a caliper and verified using digital photographs taken with a Canon DSLR camera. A picture of the setup can be seen in a sample placement verification image shown in figure 19..

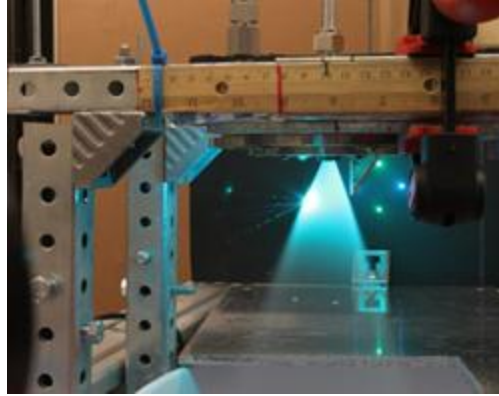


**Figure 19: Image of injector setup and beam placement verification.**

360 data runs were recorded as part of the PDPA analysis. For each run, a minimum of 2000 valid sample points were collected. The statistics of these samples was collected using the TSI FlowSizer software and exported back into Matlab. To understand the evolution of the spray, high spatial accuracy was maintained throughout the analysis. To process the data, the exported CSV files and corresponding locations were loaded into Matlab. Next, the stored unit data of interest was obtained, and an array of radial location, axial location (vertical distance from nozzle exit), and the quantity of interest was created and is shown in Fig. 20.

```

psi =
    15    20    30    40    50

>> points

points =

    10.0000    25.0000    194.3976
    11.0000    25.0000    210.7167
    12.0000    25.0000    221.5853
    13.0000    25.0000    213.9123
    14.0000    25.0000    211.4719
    13.0000    50.0000    178.8517
    15.0000    50.0000    182.9252
    18.0000    50.0000    199.1840
    20.0000    50.0000    209.5270
    22.0000    50.0000    211.2361
    24.0000    50.0000    206.2557
    20.0000    75.0000    186.6734
    23.0000    75.0000    193.9574
    25.0000    75.0000    197.8749
    27.0000    75.0000    201.4510
    29.0000    75.0000    207.7267
    31.0000    75.0000    205.5329

```

**Figure 20: Stored array of radial location, axial location, and quantity of interest. This array is created for each pressure case.**

Each data sample was collected at a singular point without movement or manipulation of the spray apparatus or laser for the range of fluid operating conditions of interest. This allows for statistics of different injection pressures to be compared at identical locations.

## 5.4 Spray Characterization Methods

Understanding the droplet size and velocity statistics is vital in understanding and characterizing the effects of various spray operating parameters. One of the most important quantifiable characteristics of the atomizing spray is the axial velocity of the fluid, which can be correlated with non-dimensional parameters of interest, allowing for further characterization of the spray. It is important to note that droplet statistics collected from PDPA represent data that the detection and analysis system have verified to come from near-spherical shapes. This is worth noting because samples collected, especially in areas prior to

complete atomization, may miss non-spherical liquid structures. As such, the PDPA data only captures the droplet phase and may have a quantifiable difference to the mean or average flow of the system.

Two common parameters used to quantify fluid flows are Weber number,  $We = \frac{\rho V^2 l}{\sigma}$  and Sauter Mean Diameter,  $D_{32}$ , where  $\rho$  is density,  $V$  is a characteristic velocity,  $l$  is a characteristic sheet thickness, and  $\sigma$  is surface tension. Each of these parameters sheds light into distinct flow phenomena. The Weber number is used to quantify the ratio of inertial to surface tension forces acting on a fluid, and the Sauter Mean Diameter (SMD) is a statistically computed value which represents the mean particle size and is more rigorously defined as the diameter of a sphere that has the average volume-to-surface-area ratio of the ensemble droplets recorded by the detection system. With each of the non-dimensional values, characteristic length and velocity scales are important in accurately quantifying the data. For Weber number calculations, information regarding the interface between the droplet and the ambient environment is desired. In order to quantify this, the characteristic length scale used is the SMD of the spray and the characteristic velocity is given as the average axial velocity of the spray. This is written as:

$$We = \frac{\rho V_{Mean}^2 D_{32}}{\sigma} \quad [6]$$

## 5.5 PDPA Results

Results of the PDPA experiments provide insight into the atomization process at different pressures and at different locations within the spray. These results can be correlated

with the flow phenomena observed in the high speed images discussed in Chapter 4. A full survey of the available data is included in Appendices B and C, with a smaller subset included below for the purposes of discussion. Data points were taken at spatial locations which contained enough spherical droplets for detection using the PDPA system. Data rates were recorded to ensure that data was collected on the periphery where few drops existed, through the local maxima within the spray, and then back to a local minimum in the hollow cone regions of the spray. As a consequence of the different spray cone angles, radial values between fluids may not be identical though sufficient data was taken to ensure for a uniform comparison.

### **5.5.1 Discussion of Axial Velocity Result**

As mentioned previously, the axial velocity of a spray plays a significant role in droplet breakup and atomization. The axial velocity for different fluids is affected by a combination of several factors, such as pressure drop across the injector and viscosity. As noted in Fig. 18, droplet statistics were collected across the spray sheet from the interior to the exterior region. An example of this is shown by comparing the profile of axial velocity of acetone and water at a distance of 50 mm from the injector exit. This is shown in Fig. 21 below.

As anticipated, higher pressures lead to higher droplet velocities. It is interesting to note that the curves for each pressure closely parallel each other from the interior to the exterior of the spray. This indicates that the average velocity measurements are highly repeatable. The shot-to-shot velocity uncertainty could not be calculated, however, because

the droplet velocities are naturally varying. Hence, it would be difficult to separate the uncertainty from the natural variation in droplet velocity.

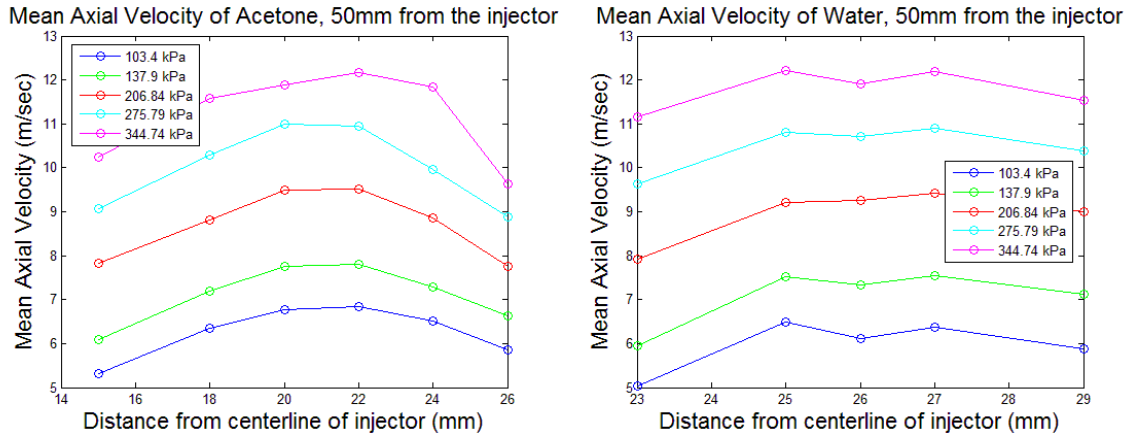


**Figure 21: A comparison of magnitude increase across the fluid sheet with increasing pressure for water (left) and acetone (right) at a fixed axial distance.**

Regarding the effects of fluid type, it is evident from Fig. 21 that the droplet statistics are comparable between the two water and acetone. The axial velocity for the lower pressure condition, for example, varies from approximately 5 m/s on the interior to between 6-7 m/s on the exterior for both water and acetone. However, the water statistics are located from 23 to 29 mm from the centerline whereas the acetone data are located from 15 to 26 mm from the centerline, indicating a wider spatial extent. This implies that the acetone spray experiences a higher spreading rate perhaps due to improved atomization. It is also evident that both fluids exhibit an increase in axial velocity of 1-2 m/s across the sheet for each of the experimental pressures. However, there is a notable difference in the shape of the magnitude of axial velocity across the liquid sheet for the two fluids. In the acetone spray distributions, it can be seen that the axial velocity continues to rise from the interior to the exterior of the sheet up to a peak value before decreasing. This is in contrast to the water spray in which the mean axial velocity increases more gradually and even dips slightly near the center of the

radial profile before dropping again towards the exterior region of the spray. This pattern is evident for all the pressure conditions. A possible explanation for this is that the water spray is dominated by hole formation, and the merged ligaments may not propagate at the same rate as ligaments formed by global instabilities.

Another interesting flow characteristic that was observed was the evolution of velocity magnitude rise across the centerline of the injector at increasing axial distances from the nozzle exit as shown below. In this case, the data show differences between water and JP-8 at 25, 50, and 75 mm from the nozzle exit.

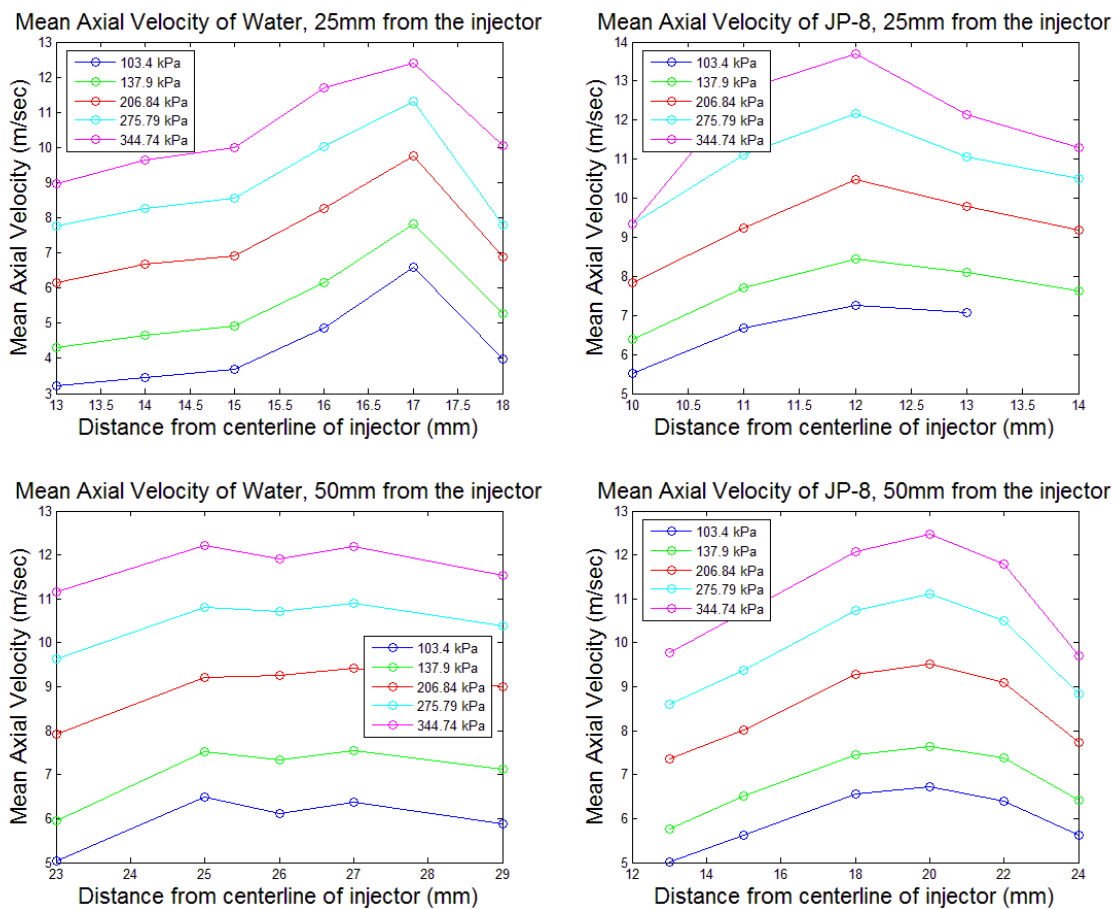
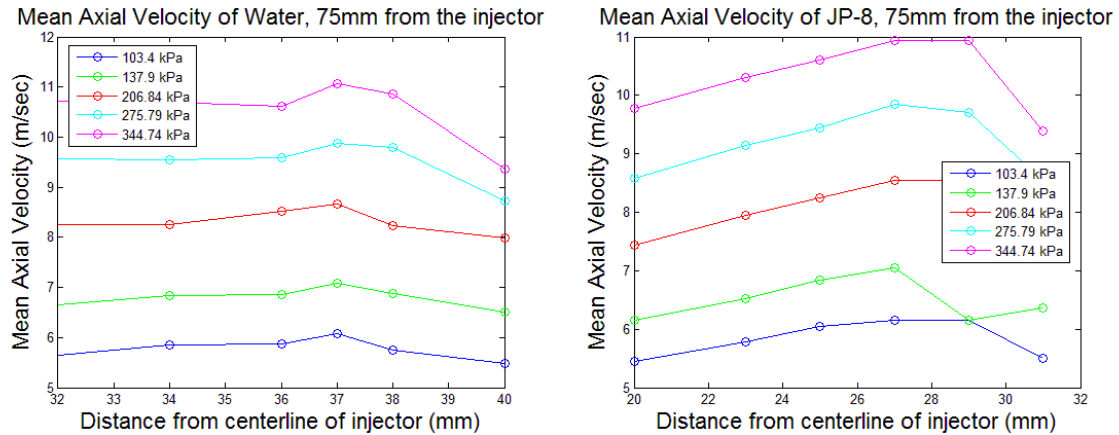


Figure 22: Evolution of velocity magnitude over a range of axial distances for water (left) and JP-8 (right)



**Figure 23: Evolution of velocity magnitude for axial distances 75mm from the injector for water (left) and JP-8 (right)**

Interestingly, the radial profile for JP-8 at 50 mm is very similar in character to that of acetone, although the axial velocity is slightly lower for JP-8 (Fig. 22) as compared to acetone (Fig. 21). Note that both fluids have similar surface tensions that are about one-third that of water. Hence, the Weber numbers for acetone and JP-8 are expected to be similar and much larger than the Weber number for water.

For the water spray, at 25 mm from the injector exit, a significant spike in axial velocity is quite pronounced indicating a narrow radial distribution of droplets. The narrow radial distribution may result from fact that the sheet is quite stable and that the droplets produced primarily by hole formation along the sheet are propagating in a narrow spatial range. However, as the spray propagates and spreads downstream, the radial distribution becomes much more broad and homogeneous, as expected. For the JP-8, at axial values close to the injector, the radial distribution does not have a spike in the axial velocity. Instead, there is a smooth and continuous increase and decrease in axial velocity. The broader spatial distribution is consistent with a breakup mode that is dominated by global aerodynamic

effects rather than local sheet instabilities. The aerodynamic instabilities lead to fluctuations in the radial sheet location and the location of ligament and droplet formation.

Unlike the water, as axial distance is increased to 50 mm and then to 75 mm, the radial distribution of axial velocity maintains similar characteristics, meaning that the spray is simply spreading as it propagates downstream. Physically, the differences demonstrated for mean axial velocity over a range of axial locations, indicate difference in the breakup behavior for water as compared to JP-8. The initially narrow radial profile for water, indicative of a narrow spatial distribution, has variations of 3-4 m/s at different radial locations, as shown in Fig. 22 at 25 mm from the injector exit. This becomes much more uniform downstream, such that the velocity varies by less than 0.5 m/s at different radial locations at 75 mm downstream from the injector exit and for the three lowest injection pressures. At higher injection pressures, the radial distribution of velocities varies more significantly because of aerodynamic forces. This is consistent with a narrower size range of droplets occurring from local instabilities within the water sheet and is in contrast with the JP-8 radial profiles, which show a self-similar broad radial profile from 25 to 75 mm. The JP-8 profiles are consistent with a wider range of droplet velocities from aerodynamic instabilities, which are then spreading as they propagate downstream.

### **5.5.2 Droplet Diameter Results**

Droplet diameter measurements provide insight into the droplet formation of the atomizing spray. Several statistical techniques were used to analyze droplet data of the injector over a range of fluids and pressures. Droplet size histograms were used to investigate droplet diameter distributions at points within the spray. By studying the distributions, insight

into the variations of droplets sizes at points can be studied providing insight into physical mechanisms driving breakup. Additionally, sauter mean diameter values provide insightful point averaged droplet statistics. The SMD point values allow for baseline comparisons between different fluids and different pressures.

Insightful information into the physical mechanisms governing the spray breakup of the fluids was obtained by comparing droplet histograms of different fluids at locally identical positions within the spray at identical injection pressures.

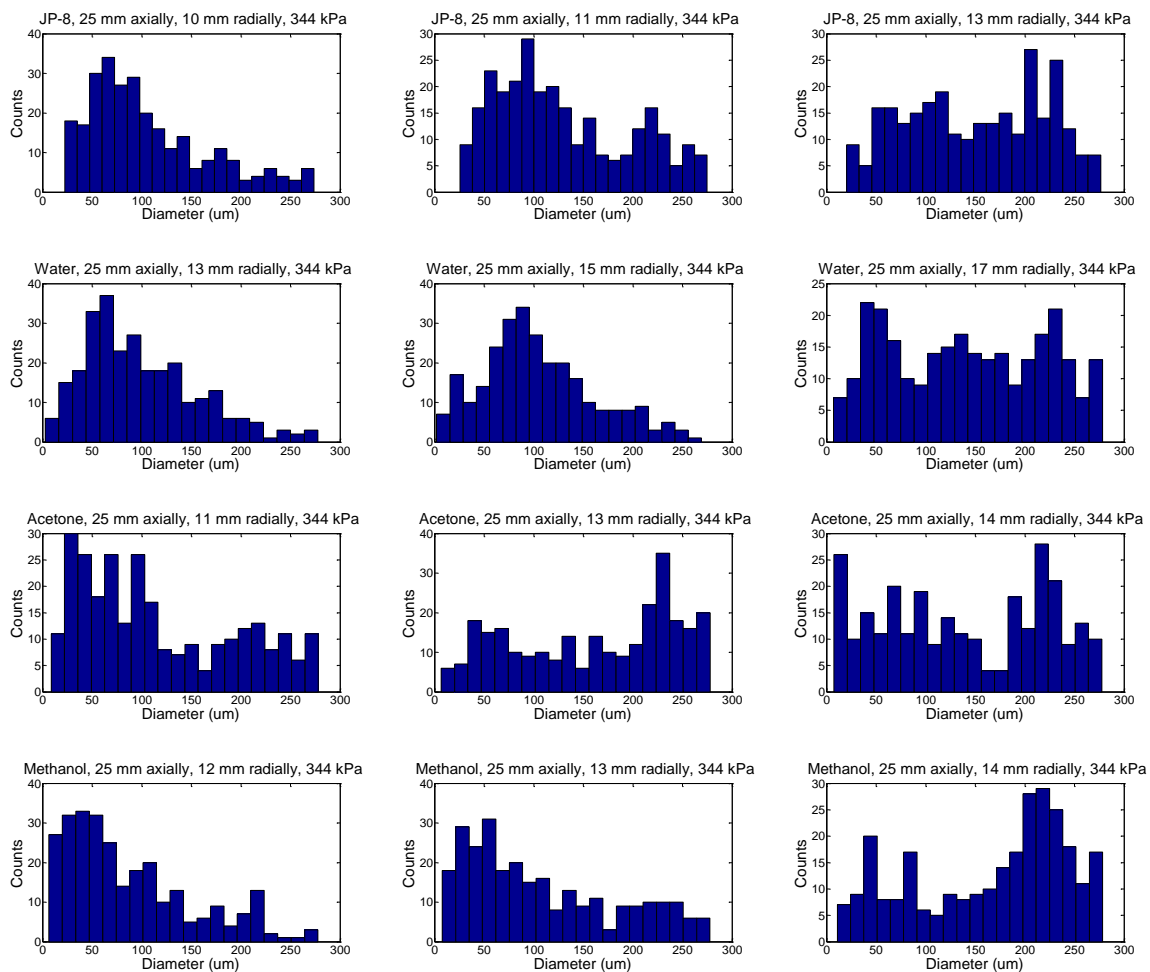


**Figure 24: Droplet diameter histogram comparison between different fluids at an identical axial distance and injection pressure of 344 kPa**

As shown in Figure 23, the droplet distribution over the range of radial locations across the fluid sheet are statistically similar among all sample fluids. In some cases, the spray is comprised mostly of small droplets less than 125 $\mu\text{m}$ . As the radial location is increased into the center of the sheet, a more uniform distribution is found though variations are present. Some insight can be found by comparing water at its central location which is uniformly left skewed to that of Acetone which is varied with a weakly statistically significant bi-modal distribution. However, at locations on the outer edge of the fluid sheet, distributions become primarily right skewed with an increased number of droplets with a diameter between 200 and 250  $\mu\text{m}$ . Of primary interest in this plot is the transition between large droplets on the outer regions of the fluid sheets to smaller droplets on the inner region of the spray. Because the transition is similar across all of the sample fluids, it is suggested that the differences indicate a transition between the dominant physical mechanism driving sheet breakup.

This physical mechanism driving breakup can be further investigated by comparing the transition from small droplets internal to the injector to larger droplets on the periphery on the fluid sheet over different pressures. This evolution can be clearly indicated by making a side by side comparison of droplet diameter histograms at identical spatial coordinates at different injection pressures.

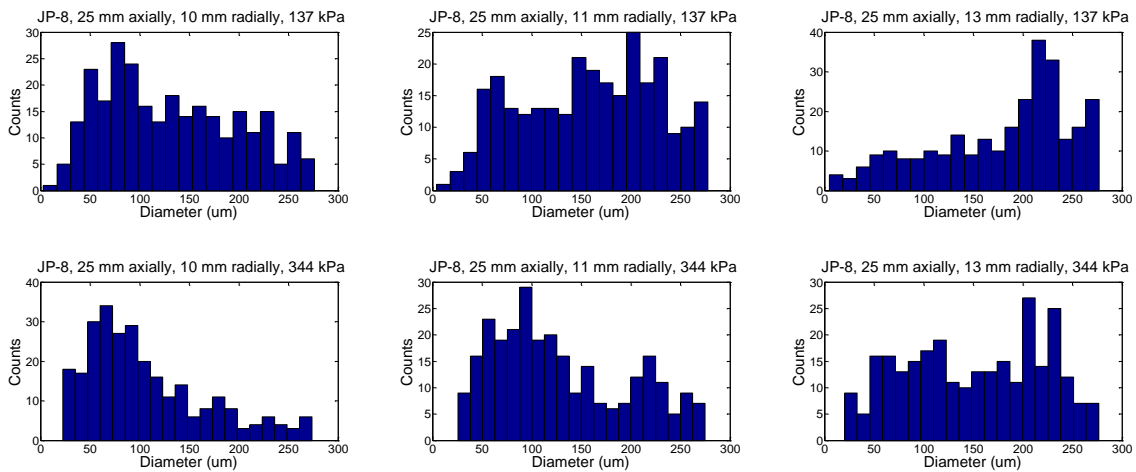


**Figure 25: Comparison of droplet diameter histograms of JP-8 at identical spatial coordinates but at injection pressures of 137 kPa and 344 kPa**

As shown in the top row of images in Fig. 24, with an injection pressure of 137kPa, the outer region of the spray cone is largely comprised of drops between 200 and 250 um. In the median region of the spray, a wide distribution of droplet sizes can be found ranging from 50-275 um. Continuing inwards, a wide distribution is again found, however, a local peak can be found for droplets between 50-100 um.

As pressure is increased to 344kPa, shown in the bottom row of Fig. 24, large droplets are again found in the outer regions of the spray cone; however, the magnitude of the shift above the median value is statistically significant. Moving through the spray cone, a significant shift in the droplet distribution from large drops to small drops is observed. Additionally, the histogram reveals a bimodal distribution with a small but statistically significant peak around 225 um and a larger peak centered around 100 um. The histogram continues to evolve with droplets continuing to decrease in size and forming left skewed distribution centered on 75um in size.

While this evolution is expected based on the previous discussion, what is interesting to note is the rate at which the transition from left skewed to right skewed and the magnitude of the largest peak within the histogram. In the 137kPa case, the droplets evolve from a strongly right skewed distribution comprised of large droplets in the outer regions of the spray cone to a weakly left skewed distribution within the spray cone. This is in contrast to the 344 kPa case which evolves from mixed and uniform distribution on the outside region of the spray cone to a strongly left skewed distribution comprised mainly of small droplets.

The change in droplet distribution across the fluid sheet at 25 mm from the injector, over a range of pressure allows for physical insight into the spray. At both injector pressures, a right skewed distribution comprised of droplets between 200-250  $\mu\text{m}$  can be found in the outer regions of the spray and a left skewed distribution with droplets between 50-100 $\mu\text{m}$  in size can be found at locations internal to the spray. Interestingly, however, distributions at locations internal to the fluid sheet indicated a bimodal distribution. This would indicate that the physical mechanism driving the droplet production of large drops is dominate at lowed injection pressures and in the outer regions of the spray whereas smaller droplets are produced faster at higher injection pressure where shear forces between adjacent cones is more significant and aerodynamic forces are creating more drag.

Droplet histograms also allow for insight into droplet distribution evolution over a range of increasing axial locations. A comparison between droplet distributions over a range of axial conditions is shown below in Fig. 25.

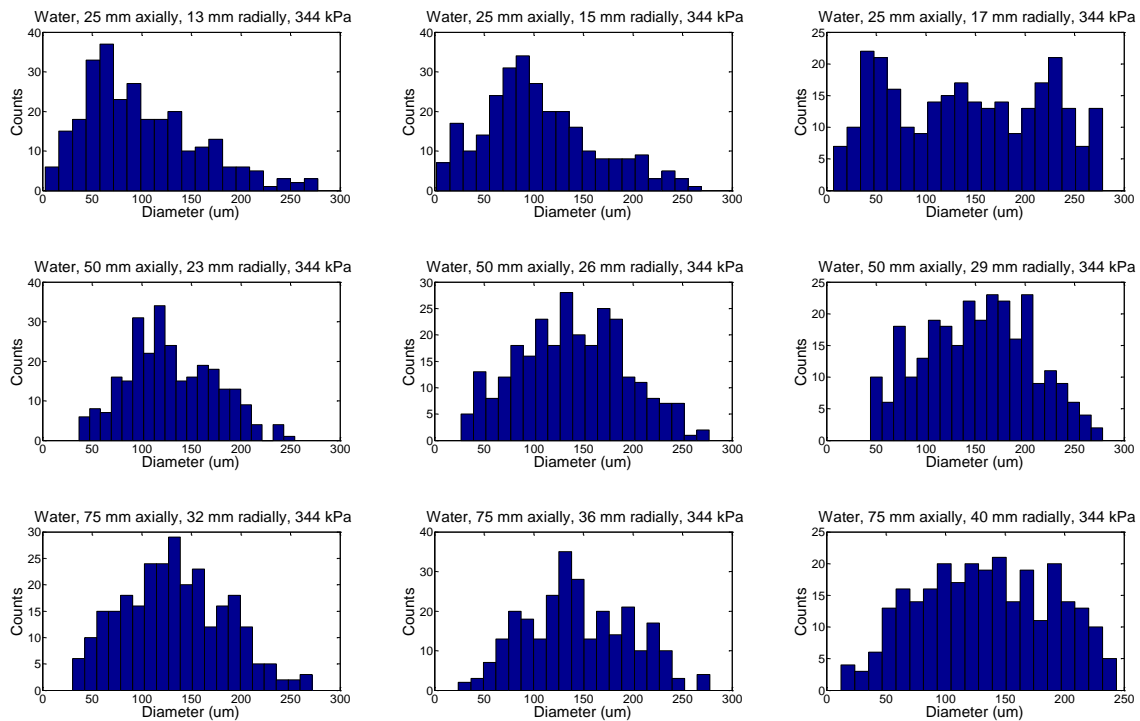


**Figure 26: Histogram comparison of water at different axial locations across the fluid sheet**

As shown in Fig. 25 above, at an axial location of 25mm, the droplet distributions of water have a left skewed distribution at radial locations near the inside of the fluid sheet. As radial value is increased, the distribution becomes more widespread and eventually becomes largely bi-modal as mentioned in the previous discussion. However, by increasing the axial location and studying the evolution across the fluid sheet, it is observed that the droplet distribution becomes more uniformly distributed across the fluid sheet. This transition from a shifting distribution across the fluid sheet indicates mixing of droplets in the area of the fluid sheet as the show increases in axial distance from the injector. Additionally, the increase in centrally located droplets could be a product of new droplets formed from the liquid sheet that were not spherical and consequently not detected by the PDPA system.

As is shown in Fig. 26, SMD measurements taken with different fluids indicate that droplet formation remains remarkably consistent for a range of fluids. However, the dependence of SMD on pressure differs for each fluid.

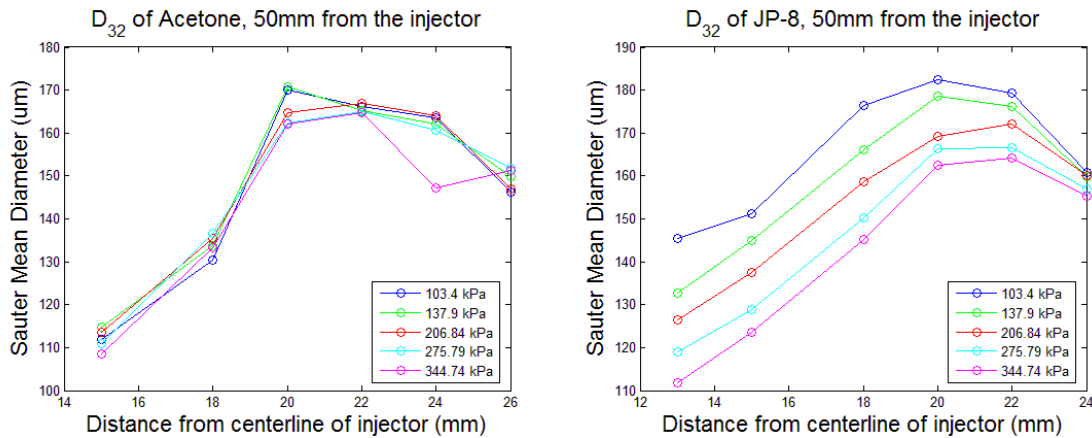


Figure 27: Sauter Mean Diameter evolution over a range of pressures and radial locations for acetone (left) and JP-8 (right).

Data taken of Acetone shows that SMD values are surprisingly similar over a range of pressures. For JP-8, however, there is a clear and consistent increase in SMD with decreasing pressure. The similarities between the SMD values over a range of pressures indicate that the physical mechanism driving droplet breakup for acetone is consistent on the interior region of the spray, producing droplets of nearly identical size independent of flow rate. This is in contrast to the breakup of JP-8 which has a significantly varying median droplet size indicating that the physical mechanism driving breakup is pressure dependent on the interior region of the spray. However, progressing radially outward, the droplet sizes have a smaller range of median values over a range of pressures indicating that the breakup mechanism is pressure independent.

Interestingly, the droplet size distributions are fairly consistent from 25 to 75 mm downstream of the injector exit, indicating that the droplets are either not breaking up to a significant extent as they travel downstream or droplets are being formed with similar characteristics at various downstream locations.

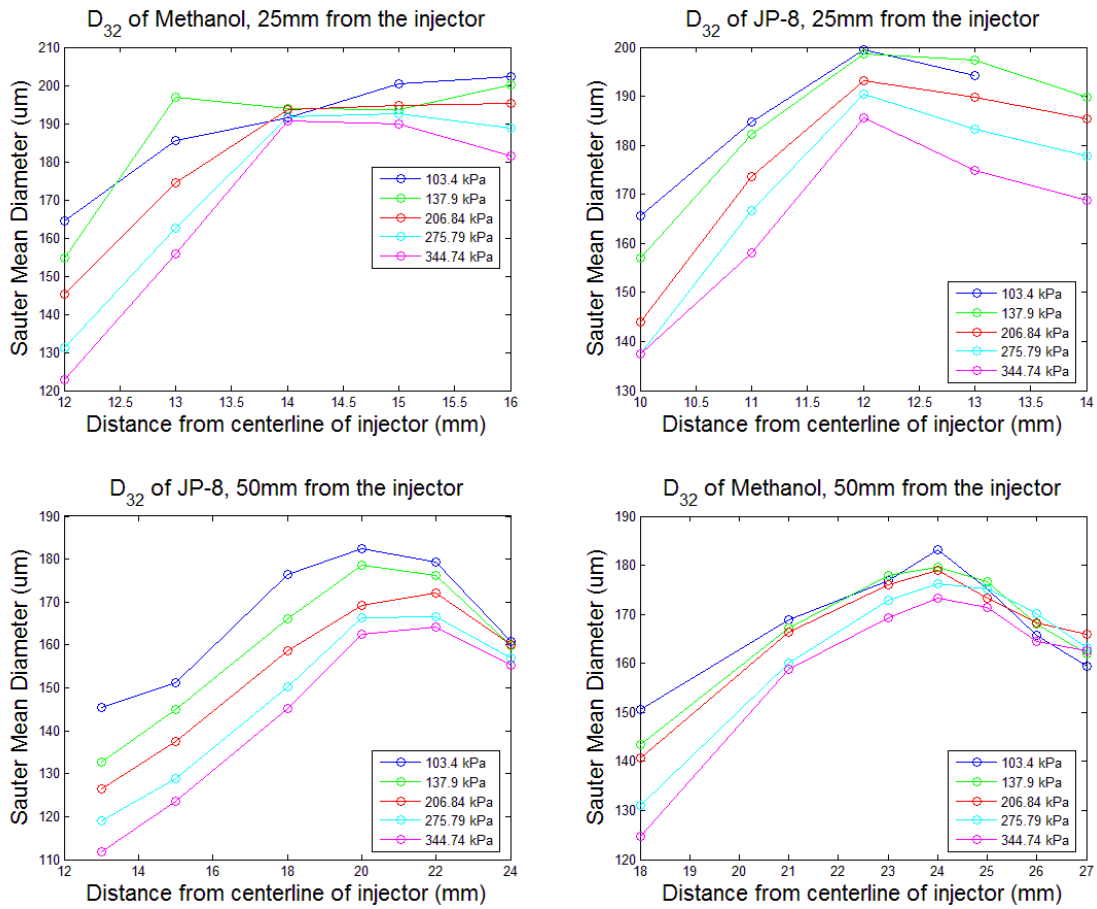
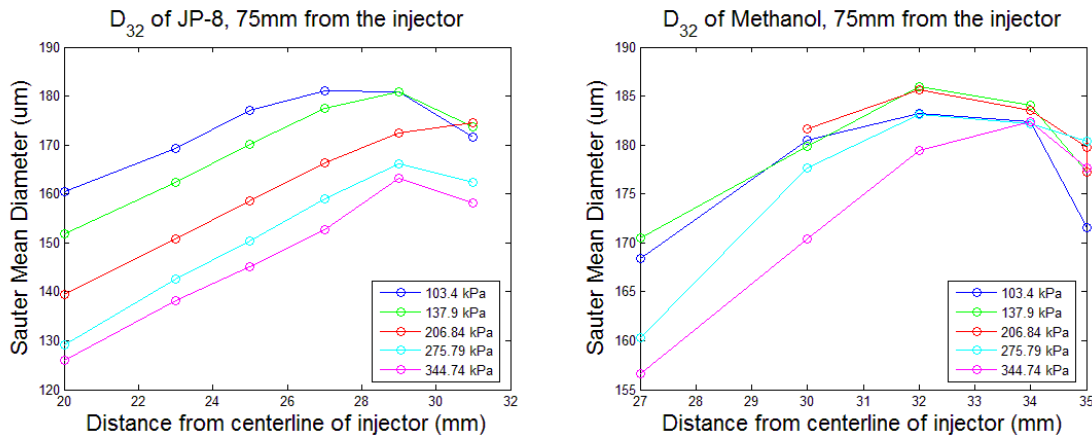


Figure 28 Sauter Mean Diameter evolution over a range of axial distances from the injector.



**Figure 29: Sauter Mean Diameter evolution over a range of axial distances from the injector.**

As can be seen in Fig. 27, it can be shown that the SMD values of droplets interior to the liquid sheet are significantly smaller than values towards the exterior. This may be the result of a recirculation region within the interior of the spray that brings smaller droplets back towards the injector exit, while larger droplets simply propagate downstream.

### 5.5.1 Discussion of Breakup Type from PDPA Analysis

A previously observed breakup phenomena classified as breakup type was investigated to see if correlations could be found among different types of fluids. Based on PDPA results, it was observed that breakup type has a noticeable impact on velocity and SMD variation. This conclusion is deduced by comparing the distribution of both velocity and SMD values over the radial locations passing through the liquid sheet. It was hypothesized that breakup type is dictated by global vs. local instability propagation. Physically, global or symmetric instabilities would produce uniform, continuous distributions of droplets in radial values near the fluid sheet. This would contrast breakup by local instabilities which would lead to a large variation in droplet size, droplet distribution and

velocity. A pictorial of this effect is drawn in Figure 25. These effects were visible in comparisons between acetone and methanol and water.



**Figure 30: Comparison between global instability producing consistent drops in a narrow range, to local instability creating a range of droplets at various locations**

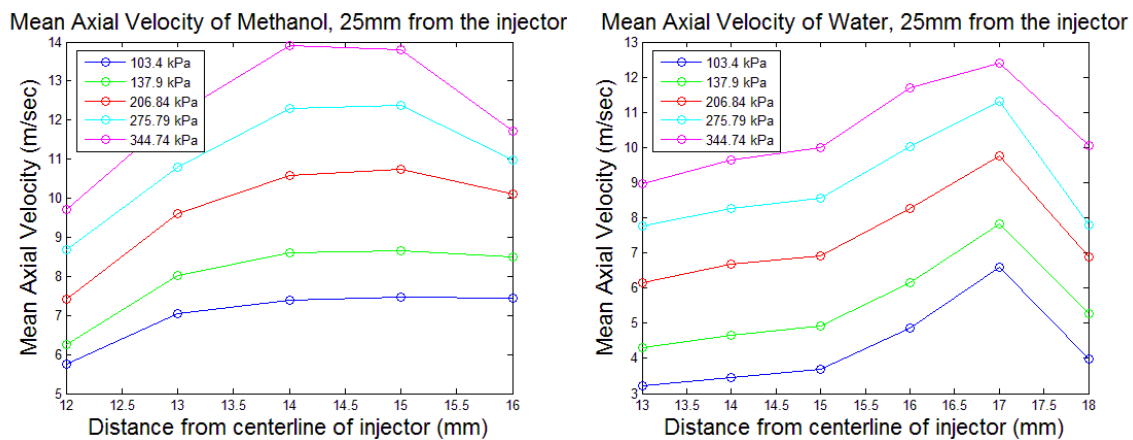


**Figure 31: Comparisons between axial velocity distributions correlating to breakup type.**

Figure 29 above shows that of the droplets that are formed for water, most of them fall into a very narrow range of radial distribution compared to methanol. This point can be further extended by comparing the variance in SMD between water and methanol at an identical axial condition.

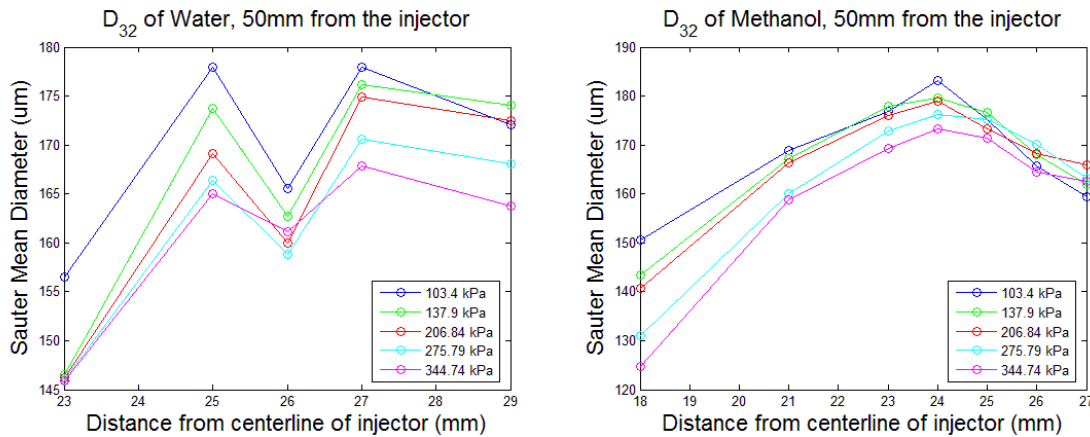


**Figure 32: Comparisons of Sauter Mean Diameter variance correlating to breakup type**

As shown above in Fig. 30, the large variance of SMD values for water over different pressures indicates quasi-periodic breakup frequencies. Additionally, the inconsistent variation in magnitude difference between flows at different pressures indicates a non-linear breakup mechanism.

Since local instabilities were most readily seen in high speed images on water atomization, this correlation with data is further made. Also following along with the fluid property comparison, it is most readily noticed that the physical property that changes the most throughout the comparison between methanol and water is surface tension. This collection of data when coupled with the high speed images helps to conclude that the variation in surface tension creates a differing breakup type which can be both qualitatively and quantitatively verified.

### 5.5.2 PDPA Analysis of Breakup Length

Analysis of high speed images comparing fluids showed that viscosity of the fluids can have noticeable effect on the breakup length. This effect was also observed using PDPA

by comparing radial mass distribution, evolution over a range axial distances. A clear comparison can be shown by comparing the fluids with highly contrasting viscosity. A comparison was done comparing the evolution of methanol to JP-8 at different axial locations.

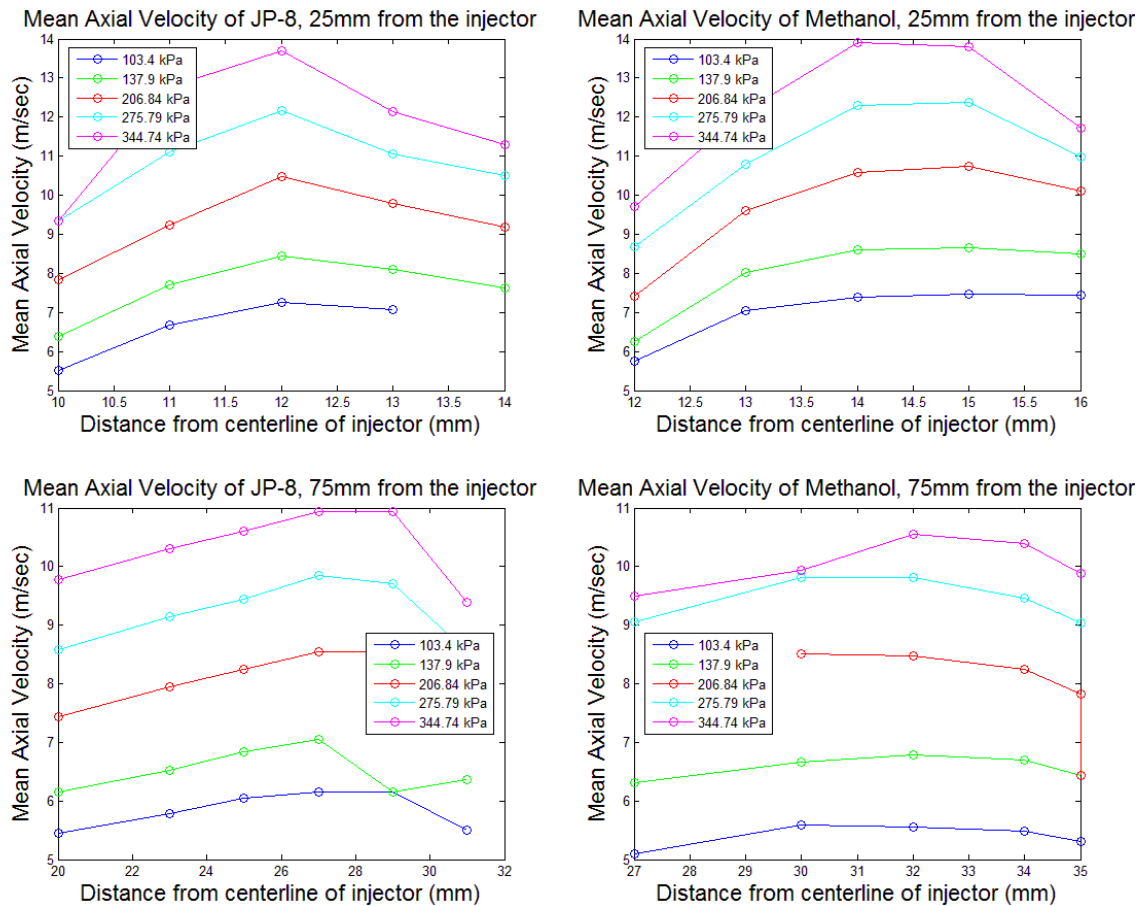


**Figure 33: A comparison of axial velocity distribution, evolution over a range of axial distances from the injector**

A comparison between axial velocity distribution evolution over the fluid sheet is shown between methanol and JP-8. As is shown in figure 31, median axial velocities between fluids are relatively uniform and quite similar for a given radial location, 25 mm from the exit. However, at 75 mm from the exit, it is shown that there is still variation in axial velocity values along an axial location in JP-8 sprays compared to methanol. This indicates that the

methanol is a fully atomized flow with many droplet interactions while the JP-8 is still undergoing droplet evolution along a radial location.

## Chapter 6. Results: X- Imaging

### 6.1 Overview

In addition to high speed imaging and PDPA, further information is desired on mass distribution throughout the atomizing fluid volume. Two techniques that have proven the ability to measure mass distributions is X-ray radiography and 3-D X-ray computed tomography (CT). X-ray analysis was performed at the Iowa State University X-ray Flow Visualization facility. The source used twin LORAD LPX200 portable sealed-tube sources provided a polychromatic source which was converted to visible light using a  $44 \text{ cm}^2 \times 44 \text{ cm}^2$  cesium-iodide scintillator screen, which allowed for visible light to be imaged using an Apogee Alta U9 CCD at resolutions up to  $3072 \times 2048$ . To increase contrast, a potassium iodide (KI) contrast enhancing agent was mixed with the fluid prior to each experiment.

### 6.2 Experimental Considerations

The first step performed prior to each spray study was a quantification of the amount of contrast enhancing agent that would be needed to complete the study. To do this, a 2 gallon mixture of deionized water was sprayed through the injector with differing levels of KI. Previous studies (Meyer, et al., 2008) indicated that solutions of KI levels up to 50% have yielded sufficient absorption levels for successful 3-D tomographic reconstruction. Radiographs were taken at solutions of 15%, 25%, and 30% as shown in Figure 29.

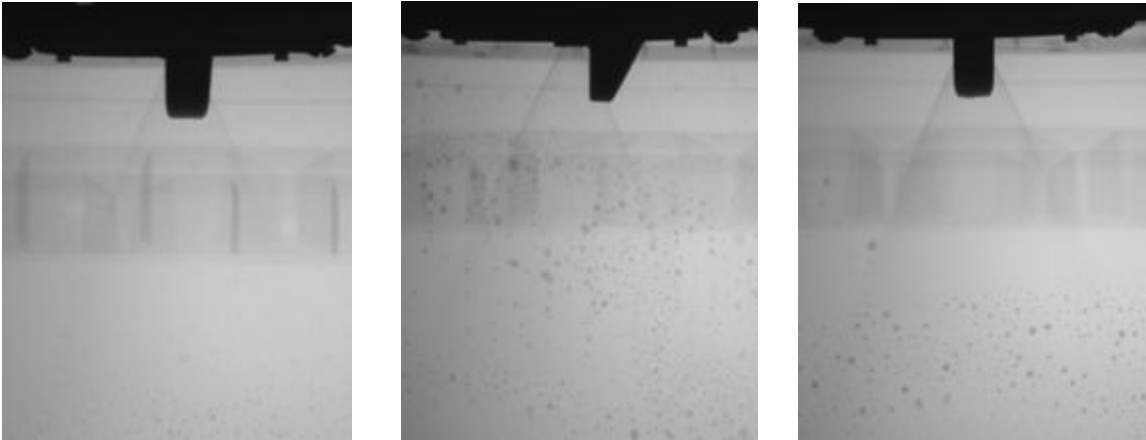


**Figure 34: X-ray radiographs with differencing levels of potassium iodide (KI). Case with 15%, 25%, and 32% are shown on the left, middle, and right, respectively.**

After analyzing the results, it was determined that a 30% solution would provide sufficient absorption.

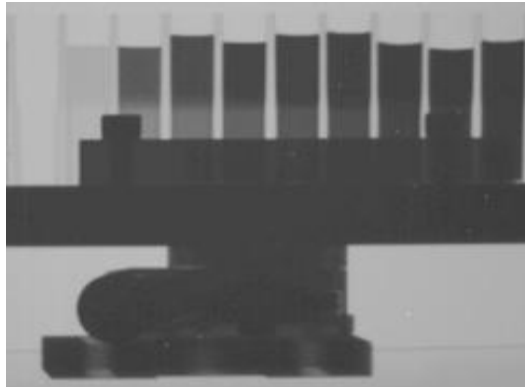


**Figure 35: X-ray radiographs cuvettes of air, deionized water, and deionized water mixed with KI at concentrations of 10%, 15%, 20%, 25%, 30%, 35%, 40%, 50% by mass.**

In order to verify that the absorption coefficient of KI is still linear with KI concentration in the range of path lengths between 2.5-5mm, a cuvette study was performed. The study was performed by mixing known concentrations of KI in cuvettes of known path length. The intensity of signal through the fluid medium can then be compared to the

intensity of background signal allowing for an absorption coefficient to be calculated in accordance with Beers law. An image of the cuvette radiograph is shown in figure 33.

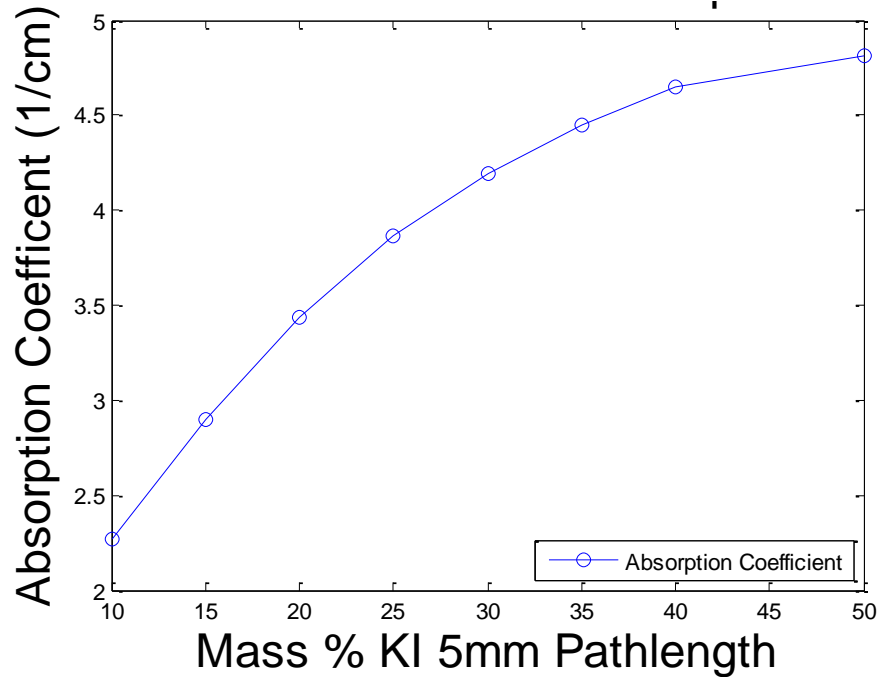


**Figure 36: Absorption coefficient versus KI concentration.**

As shown in Fig. 34 above, a slightly nonlinear dependence of the absorption coefficient on KI concentration is noted for KI concentrations ~30% for pathlengths up to 5 mm, indicating that so-called beam hardening may be taking place. Since the spray at hand has an estimated sheet thickness closer to 1 mm, a 30% solution is assumed to absorb with minimal beam hardening.

## 6.3 Radiograph Data

### 6.3.1 Radiographs

Once a graph of absorption versus Mass % KI was created which indicated that for sheet thickness close to 1 mm, beam hardening was minimized, radiographs were taken to

investigate variations in sheet thickness among different recess design segments. Example recess design radiographs are shown in the figures 35-38 below.

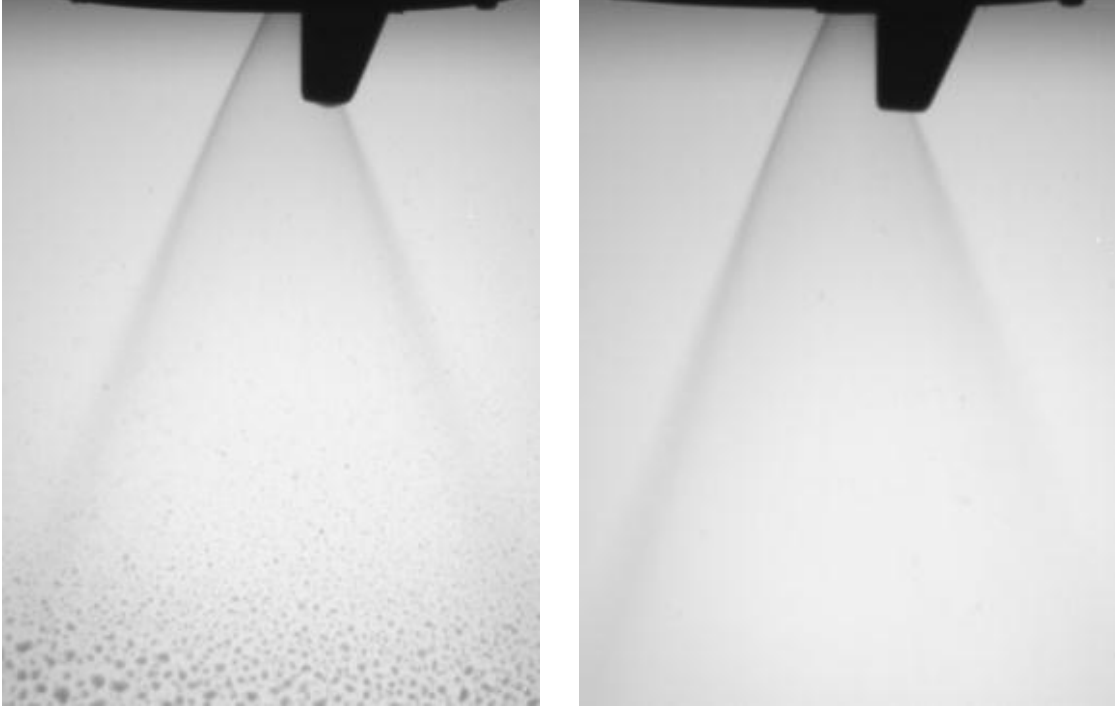


**Figure 37: Radiograph of Recess Design 1 (left) and Recess Design 2 (right) at 137.9 kPa**

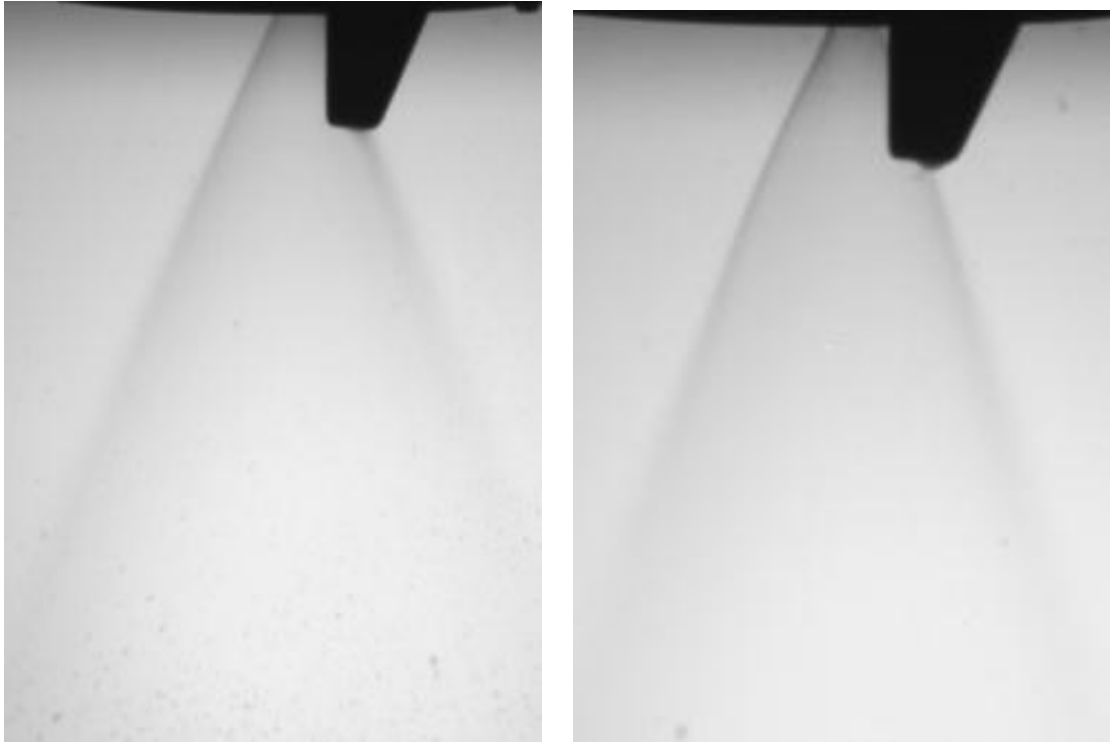


**Figure 38: Radiograph of Recess Design 3 (left) and Recess Design 4 (right) at 137.9 kPa**



**Figure 39: Radiograph of Recess Design 5 at 137.9 kPa**

Further investigation was also desired into spray sheet thickness of a common geometry at several pressure points. In order to help better understand this sheet thickness evolution, radiographs of KI doped water sprays were taken with Recess Design 1 at 68.95 kPa, 137.9 kPa, and 206.8 kPa. These radio graphs are shown below:

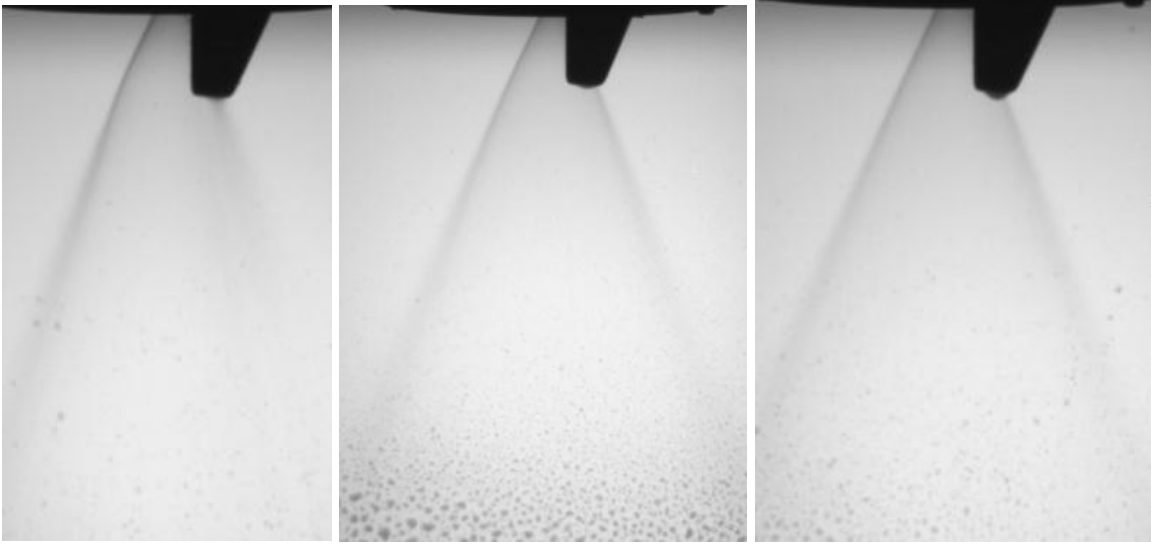


**Figure 40: Recess Design 1 at 68.95 kPa, 137.9 kPa, and 206.8 kPa, from left to right**

### 6.3.2 Radiograph Results

Experimental values for sheet thickness were computed by comparing signal intensity at axial locations in the spray to signal values immediately adjacent to the spray. This ratio of signal was then correlated into a path length equal to both fluid sheets by using the previously found absorption coefficient. Values of sheet thickness are shown below.

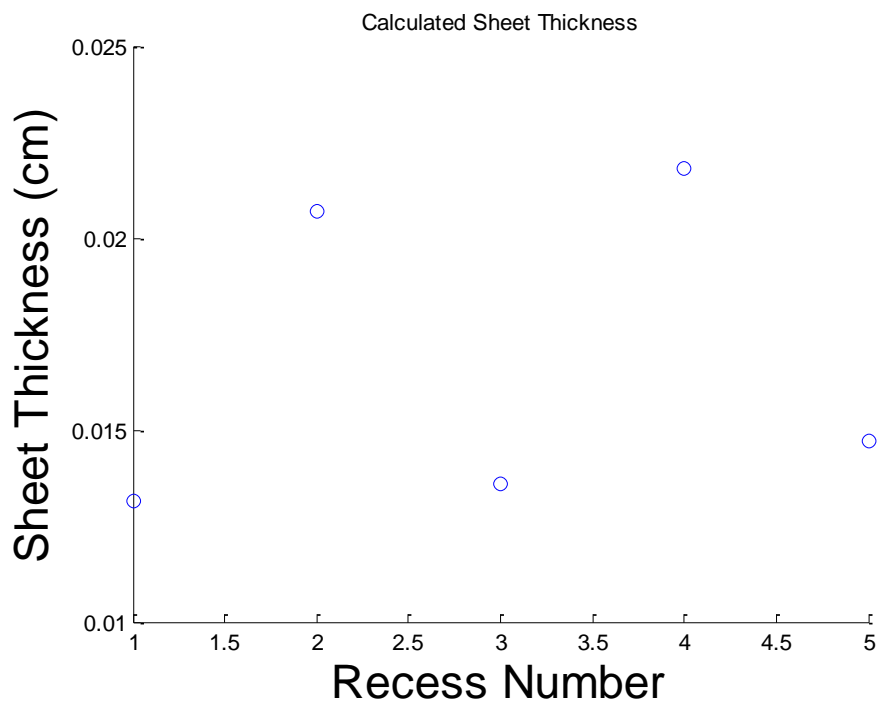


Figure 41: Experimental sheet thickness values for different recess numbers

## 6.4 X-ray CT Data

After linearity was confirmed, CT scans were performed on the injector with Recessed Length 1 at 103 kPa inlet pressure. The resulting image is shown below.

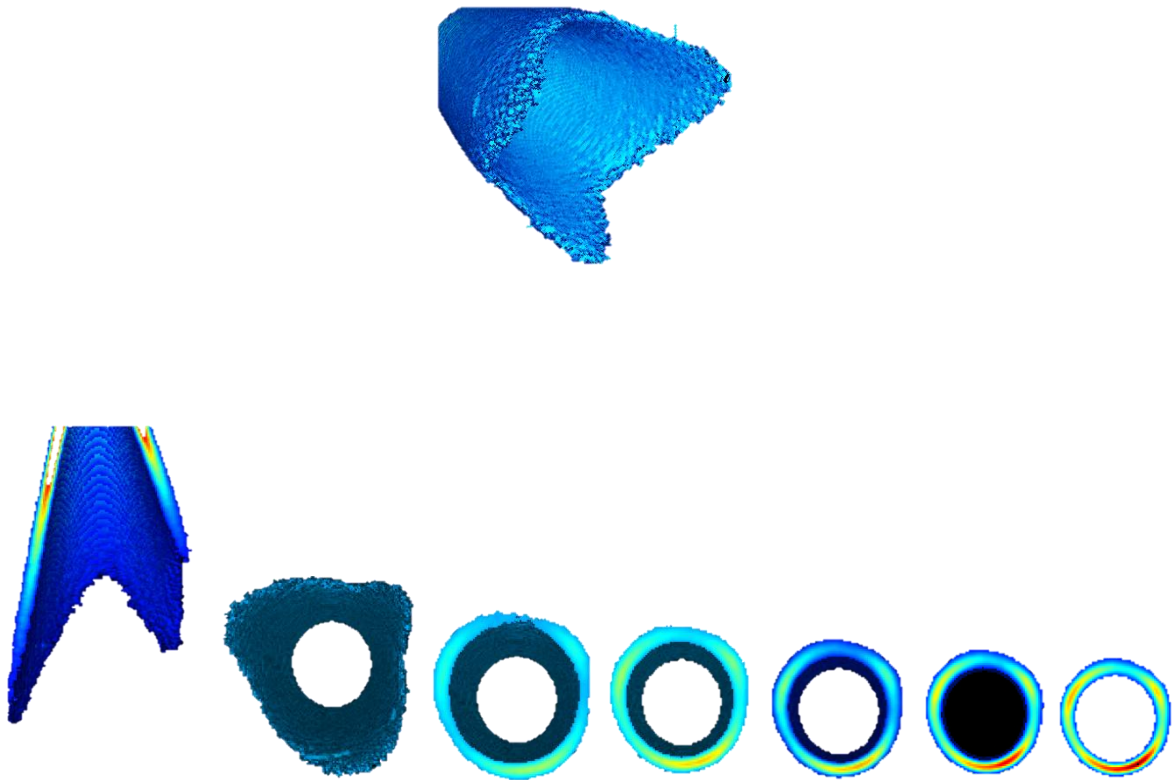


Figure 42:3-D CT reconstruction of time-averaged spray for Recessed Length 1 at 137kPa injector inlet pressure.

## 6.5 Discussion

X-ray radiography experiments helped reveal the optically dense regions of the spray. This region of the spray cone is often a solid liquid sheet and quantifiable and extractable knowledge is not possible with either of the techniques previously discussed. This region is of significant interest in determining effectiveness of fluid mixing as well as quantifiable extraction of mass distribution and sheet thicknesses

Several quantifiable characteristics were revealed from 3-D CT reconstructions. Firstly, results indicate that fluid density in the liquid sheet region of the spray is not axisymmetric. This is indicated by 3 regions of increased density in the midline of the spray. An explanation of this phenomenon is not immediately available. However, several hypotheses have been proposed.

Previous work on acoustic stability (Sivakumar & Raghunandan, 1998) has shown that wave propagation from initial sheet formation regions internal to the geometry may be creating an acoustic resonance leading to flow bias. However, because CT scans used in the production of this reconstruction were taken using 1 second exposures, any acoustic phenomena would need to interact on time scales is near or in excess of the 1 second integration time.

Another hypothesis proposed is that small differences in geometrical factors relevant to the injection, such as injection diameters or internal length scales of the fluid may have resulted in flow bias through one, or several injection orifices. While all geometrical quantities of interest were manufactured within narrow tolerances, discrepancies within these ranges may still exist, resulting in this error

Finally, it is worth noting that these discrepancies seem to have an effect in the distribution of mass along the axis of travel. It is seen from the iso-metric view of the cone, that the mass fraction has 3 local maximums that stem from regions of increased density at the top. This indicates that not only does the flow discrepancy affect regions of solid or continuous liquid sheets, but that the bias is maintained in regions of aerodynamic breakup

It should be noted that the density bias could create acoustic instability if present at injection conditions used at operation. Because of this implication, further investigation is desired to help better understand the nature of this flow bias

## **6.6 A novel use of high speed images as a supplement to CT scans for sheet thickness**

### **6.6.1 Motivation**

As we have seen, high speed imaging allows for significant qualitative information to be extracted in regards to liquid breakup and atomization. However, utilization of its' high precision time stepping ability allow for further expansion of its role in extracting quantitative information, such as sheet thickness out of images.

### **6.6.2 Development**

High speed images allow for high speed flow phenomena to be captured and investigated. One feature of significance is instability propagation as well as hole formation. While high speed imaging allows for these structures to be better understood, in the tool development at hand, these locations of local inhomogeneous flow conditions allow them to

be utilized as flow markers. This flow marker, in addition with the highly accurate time stamp on each image allow for sheet velocity to be calculated. This is of particular interest because of the breakdown of PDPA's effectiveness in regions of stable sheet formation. While PDPA requires spherical droplets, high speed imaging has little bias.

### **6.6.3 Results**

High speed images of deionized water were taken to help better understand high speed flow phenomena in the spray. However, these images were also able to be used to compute flow velocity by marking where instability is first seen, and measuring the distance that the instability moves in a small time step. By leveraging this fact, it is hoped that a verification of liquid sheet thickness can be made without the use of CT scans due to the expense of dopants often required for imaging of water sprays.

In order to test this tool, a series of high speed images would be used to collect velocity information from fluid sheets. These values are then compared to PDPA values and used in the calculation of sheet thickness from mass conservation.

The first step in collecting velocity measurements from high speed images is the identification of stable flow feature. An example of this is shown in figure 40 below..

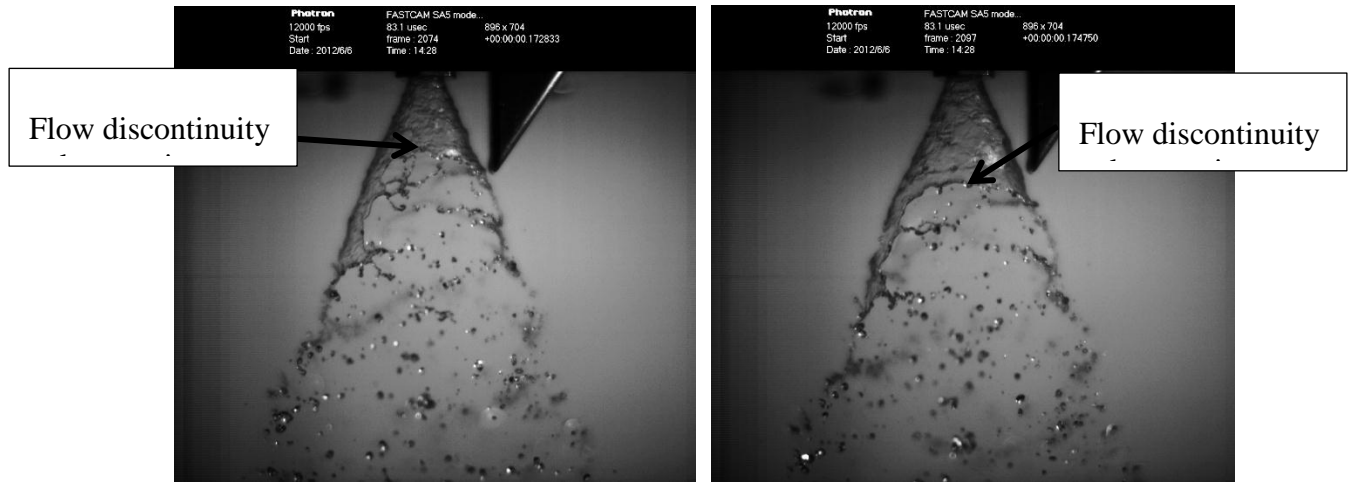


**Figure 43: 68.95 kPa flow of deionized water for use in velocity extraction**

As is seen in Figure 41, a flow feature is observed in an area of solid fluid sheet. The pixel value of the discontinuity is recorded at both locations. Then, by using geometrical features of known size in the field of view, a metric relating pixel size and physical distance can be created. The change in pixel size can then be turned into a change in physical size, and since the time is known with significant accuracy, a velocity can be computed. This processes was done 2 times at 4 pressure cases allowing for an average value to be used to create a curve of pressure versus velocity. The values used are shown in the Table 4.

**Table 4: Velocity extraction from high speed images**

Pressure	68.9 kPa		137.9 kPa		206.9 kPa		275.8 kPa	
Time 2	0.173	0.1815	0.179	0.1673	0.1672	0.1705	0.1680	0.171917
Time 1	0.1748	0.1846	0.1787	0.1666	0.1666	0.1699	0.1675	0.1712
Pixel 2	251	223	284	271	279	276	246	260
Pixel 1	305	303	295	302	316	314	289	316
Difference	54	80	11	31	37	38	43	56
Pixel to Physical Space	0.0071	0.0105	0.0014	0.0041	0.0048	0.0050	0.0056	0.0073
Velocity (m/s)	3.687	3.307	5.760	6.093	8.308	8.532	11.26	10.99

Once these values were collected, the averages of the 2 runs were taken, and the values were plotted versus pressure shown in Figure 42.

As can be seen in figure 42 velocity, increases as a function of pressure. What is also interesting is the changing trend that can be observed as pressure is increased. A hypothesized reason for this would be a significantly increasing drag force or increase in frictional drag. It also allows us to be able to compute a velocity at any given pressure. Since a CT scan was performed at 103.4 kPa, the technique will be verified using previous CT scans.

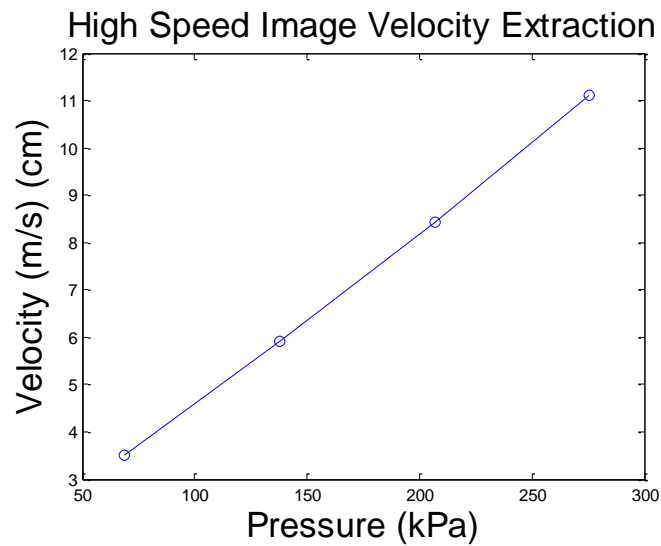


Figure 44: Experimentally produced velocity vs. pressure curve.

From the curve fit, and the desired pressure of 103.4 kPa, an estimated velocity of 4.69 m/s was computed. From this velocity and a conservation of mass for a control volume which can be written as:

$$\dot{m} = \rho V A$$

Where  $\dot{m}$  is the known mass flow rate,  $\rho$  is the density of the fluid,  $V$  is the axial velocity and  $A$  is the cross sectional area of the fluid volume. Since  $\dot{m}$ ,  $\rho$ , and  $V$  are known, the cross sectional area of the fluid volume can be determined. From this, the sheet thickness was shown to be 0.0004 m thick. This value, however, does compare with radiographs taken of the spray which indicated the spray to be approximately .000762 m thick. While this difference is almost a factor of 2, the ready availability of this technique as well it's complimentary significance with PDPA for velocity measurements merits further exploration and verification.

## Chapter 7. Summary and Future Work

The atomization characteristics of a liquid-liquid swirl injector was characterized using non-invasive optical techniques. Each technique provided insight into an aspect of fluid breakup within the injector

High speed images were taken of the injector at different flow conditions looking to characterize the significance of geometric factors in droplet breakup. Five geometries were studied and significant differences in breakup characteristics were observed in breakup length as well as droplet distribution in the region of interest. Additionally, information from the images collected allowed for the specific geometrical parameters to be isolated.

Additionally, high speed images were used to help characterize breakup phenomena of different fluids at comparable flow conditions for a fixed geometrical setup. This study was performed to shed light on potential use of the injector for combustion of cryogenic liquid methane as well as other potential fuel sources.

### 7. 1 Conclusions

Several conclusions were able to be inferred from the experimental survey that was performed. The geometrical parameters of several Recess Length geometries were varied and a parametric study was performed. The result of this study indicated that the dominant geometrical factors were trumpet half angle and cylindrical diameter. It was shown that trumpet half angle was the geometric parameter governing breakup type and cylindrical diameter governed breakup length.

These geometrical parameters were further investigated by performing a study with several different fluid types. This study showed that properties such as surface tension can create noticeably different spray results that can be quantified high speed images and radiographs.

Next, X- ray radiographs were used to investigate the internal structure and distribution of sprays near the exit. Of particular note was the discovery of 3 local maximums in an axially symmetric position. The root cause of this has yet to be discovered; however, this anomaly could potentially lead to combustion instability. Because of this, further CT analysis is desired for investigation as to the source of this discrepancy. A wider range of pressure inputs would be desired to see if density distributions normalize at higher pressures or are more pronounced at lower pressures.

Finally, high speed images were used to estimate sheet thickness of the spray in regions available for high volume data collection by PDPA. This complementary utilization of high speed imaging as a verification of computed tomography and X-ray radiography suggests future redundant measurement availability. Furthermore, the technique utilized also suggests the potential for velocity measurements from radiographs. While velocity measurements would be time averaged, significant advantages of X-ray and their ability to probe optically unavailable environments suggest future work on this topic would be desired.

## **7.2 Future Work**

Non-invasive laser, optical and X-ray diagnostic techniques provided information on flow phenomena in spray breakup. Results of the study performed allowed for quantification of the roles of the geometric configuration of the injector, as well as the dependence on the

fluid being atomized by the injector. However, future work is desired to expand upon on the results and conclusions obtained in the study performed.

First, further investigation into the roles of non-dimensional parameters is desired. Non-dimensional analysis could shed light into the governing fluid phenomena of the spray and atomization process. Further, it would allow for better parametric comparisons of the sprays studied.

Next, additional CT scans, and CT scans taken with higher resolution sensors would provide better insight into average mass distributions over a range of injection pressures. The added resolution would provide new insights to mass distributions across the liquid sheet, and could also reduce exposure time allowing for instantaneous mass distribution studies to be performed.

Finally, hot fire tests over a range of pressures and geometries would allow for conclusions reached in this study to be validated. Additionally, the relative magnitude of the geometric parameters could be further quantified.

## Chapter 8: Works Cited

- (SNECMA), S. N. D. & D. C. D. M. D., 2006. Methane rocket engine proves worthy of study. *Flight International*, 6 April.
- Andersen, P. C. & Bruno, T. J., 2005. Thermal Decomposition Kinetics of RP-1 Rocket Propellant. *Ind. Eng. Chem. Res.*, pp. 1670-1676.
- Ashgriz, N., Li, X. & Sarchami, A., 2011. Instability of Liquid Sheets. In: *Handbook of Atomization and Sprays*. New York: Springer, pp. 75-95.
- Ash, R. L., Dowler, W. L. & Varsi, G., 1978. Feasibility of rocket propellant production on Mar. *Acta Astronautica*, pp. 705-724.
- Bachalo, W., 2000. Spray Diagnostics for the Twenty-First Century. *Atomization and Sprays*, Volume 10, pp. 439-474.
- Bachalo, W. & Houser, M., 1987. Spray Drop Size and Velocity Measurements Using the Phase Doppler Particle Analyzer. *International Journal of Turbo and Jet Engines*, p. 207\*215.
- Beckstead, M. W., Puduppakkam, K., Thakre, P. & Yang, V., 2007. Modeling of combustion and ignition of solid-propellant ingredients. *Progress in Energy and Combustion Science*, pp. 497-551.
- Chehroudi, B., 2010. Physical Hypothesis for the Combustion Instability in Cryogenic Liquid Rocket Engines. *Journal of Propulsion and Power*, 26(6), pp. 1153-1160.
- Cheng, G. C., Johnson, C. W., Muss, J. A. & Cohn, R. K., 2002. *Swirl Coaxial Injector Development Part II CFD Modeling*. Destin, s.n.
- Clark, J. D., 1972. *Ignition!: An informal history of liquid rocket propellants*. s.l.:Rutgers University Press.
- Cohn, R. K., Danczyk, S. A. & Bates, R. W., 2003. *A Comparison of the Performance of Hydrocarbon Fuels in a Uni-element Combustor*. Huntsville, s.n.

- Colket, M. B. & Spadaccini, L. J., 2001. Scramjet Fuels Autoignition Study. *Journal of Propulsion and Power*, pp. 315-323.
- Culick, F. E. C., 1988. *Combustion Instabilities in Liquid-Fueled Propulsion Systems- An Overview*. s.l., s.n., p. 450.
- Culick, F. E. & Yang, V., 1995. Overview of Combustion Instabilities in Liquid-Propellant Rocket Engines. In: *Liquid Rocket Engine Combustion Instability*. Washington DC: AIAA, pp. 3-37.
- Dombrowski, N. & Fraser, R. P., 1954. A Photographic Investigation into the Disintegration of Liquid Sheets. *Philosophical Transactions of the Royal Society of London*, pp. 101-130.
- Fraser, R., Dombrowski, N. & Eisenklam, P., 1954. Vibrations as a Cause of Disintegration in Liquid Sheets. *Nature*, p. 495.
- Fung, Y. T. & Yang, V., 1992. Active Control of Nonlinear Pressure Oscillations in Combustion Chambers. *Journal of Propulsion and Power*, pp. 1282-1289.
- Glarborg, P. & Nils, L. I., 1992. *A reduced mechanism for nitrogen chemistry in methane combustion*. s.l., s.n., pp. 889-898.
- Gotsulenko, V. V., 2008. Distinctive Features of the intrachamber instability of combustion in liquid-propellant rocket engines. *Journal of Engineering Physics and Thermophysics*, 81(5), pp. 935-940.
- Greatrix, D. R., 2012. Multisized Inert Particle Loading for Solid Rocket Axial Combustion Instability Suppression. *International Journal of Aerospace Engineering*, Volume 2012.
- Hamady, F. J., Hagn, J. P., Hellman, K. H. & Gray Jr., C. L., 1994. *High-Speed/High-resolution Imaging of Fuel Sprays from Various Injector Nozzles for Direct Injection Engines*, s.l.: EPA/AA/TGD.
- Heindel, T. J., Gray, J. N. & Jensen, T. C., 2008. An X-ray system for visualizing fluid flows. *Flow Measurement and Instrumentation*, pp. 67-78.
- Holden, C., 1990. A Sailing Race to Mars?. *Science*, p. 965.
- Holladay, J. D. et al., 2007. Microreaction development for Martian in situ propellant production. *Catalysis Today*, pp. 35-44.

- Inamura, T., Tamura, H. & Sakamoto, H., 2003. Characteristics of Liquid Film and Spray Injector from Swirl Coaxial Injector. *Journal of Propulsion and Power*, pp. 632-639.
- Ismailov, M. & Heister, S., 2011. Dynamic Response of Rocket Swirl Injectors, Part I: Wave Reflection and Resonance. *Journal of Propulsion and Power*, pp. 402-411.
- Joo, H. I. & Gülder, Ö. L., 2010. *Structure of Laminar Methane-Oxygen Diffusion Flames at High Pressure*. Orlando, s.n.
- Kastengren, A. & Powell, C. F., 2007. Spray density measurements using X-ray radiography. *Journal of Automobile Engineering*, pp. 653-661.
- Kim, D. et al., 2007. Effect of Recess on the Spray Characteristics of Liquid Liquid Swirl Coaxial Injectors. *Journal of Propulsion and Power*, pp. 1194-1203.
- Klepikov, I. A., Katargin, B. I. & Chvanov, V. K., 1997. The new generation of rocket engines, operating by ecologically safe propellant "liquid oxygen and liquefied natural gas (methane)". *Acta Astronautica*, pp. 209-217.
- Klimenki, D. N. et al., 2002. CARS temperature mapping in a cryogenic LOX-H<sub>2</sub> rocket combustion chamber under supercritical conditions. *Journal of Raman Spectroscopy*, pp. 900-905.
- Laudien, E., Pongratz, R., Pierro, R. & Preclik, D., 1995. Experimental Procedures Aiding the Design of Acoustic Cavities. In: *Liquid Rocket Engine Combustion Instability*. s.l.:AIAA, pp. 377-399.
- Lefebvre, A. H., 1989. *Atomization and Sprays*. Washington, D.C.: Hemisphere.
- Linne, M., 2012. Analysis of X-ray radiography in atomizing sprays. *Exp. Fluids*.
- Mayer, W. & Tamura, H., 1996. Propellant Injection in a Liquid Oxygen/Gaseous Hydrogen Rocket Engine. *Journal of Propulsion and Power*, pp. 1137-1147.
- Meyer, T. R. B. M. J. S. H. a. G. J. R., 2010. Formation and Diagnostics of Sprays in Combustion. In: *HANDBOOK ON COMBUSTION*. s.l.:s.n., p. 291-322.
- Meyer, T. R., Schmidt, J. B., Drake, J. B. & Heindel, T. J., 2008. *Three-Dimensional Spray Visualization using X-ray Computed Tomography*. Orlando, s.n.
- Moses, C., 2011. *Properties of Russian Jew Fuels, CRC Project AV-12-10*, Alpharetta: Coordinating Research Council.

- Muss, J. A., Johnson, C. W., Kruse, W. & Cohn, R. K., 2003. *The Performance of Hydrocarbon Fuels with H<sub>2</sub>O<sub>2</sub> in a Uni-element Combustor*. Huntsville , s.n.
- Natan, B. & Rahimi, S., 2001. The Status of Gel Propellants in Year 2000. *Combustion of Energetic Materials*.
- Oefelein, J. C. & Yang, V., 1993. Comprehensive Review of Liquid-propellant Combustion Instabilities in F-1 Engines. *Journal of Propulsion and Power*, pp. 657-677.
- Photron USA, INC, n.d. *FASTCAM SA5 Ultra High-Speed Video System*. [Online] Available at: [http://www.photron.com/datasheet/FASTCAM\\_SA5.pdf](http://www.photron.com/datasheet/FASTCAM_SA5.pdf) [Accessed 22 July 2012].
- Rapp, D. C. & Zurawski, R. L., 1988. *Characterization of Aluminum/RP-1 Gel Propellant Properties*. Boston, s.n.
- Ryan, H. M., Anderson, W. R., Pal, S. & Santoro, R. J., 1995. Atomization Characteristics of Impinging Liquid Jets. *Journal of Propulsion and Power*, pp. 135-145.
- Saiki, Y., Kurimoto, N., Suzuki, Y. & Kasagi, N., 2011. Active control of jet premixed flames in a model combustor with manipulation of large-scale vortical structures and mixing. *Combustion and Flame*, Volume 158, pp. 1391-1403.
- Sirignano, W. A. & Mehring, C., 2000. Review of theory of distortion and disintegration of liquid streams. *Progress in Energy and Combustion Science*, pp. 609-655.
- Sivakumar, D. & Raghunandan, B. N., 1998. Hysteretic interaction of conical liquid sheets from coaxial atomizers: influence on the spray characteristics. *Physics of Fluids*, pp. 1384-1397.
- Soltani, M. R., Ghorbanian, K., Ashjaee, M. & Morad, M. R., 2005. Spray characteristics of a liquid-liquid coaxial swirl atomizer at different mass flow rates. *Aerospace Science and Technology*, pp. 592-604.
- Son, S. F., 2007. Introduction: Nanoscale Composite Energetic Materials. *Journal of Propulsion and Power*, pp. 643-644.

- Space Exploration Technologies Corp, 2012. *Falcon 9 Overview*. [Online]  
Available at: [http://www.spacex.com/falcon9.php#merlin\\_engine](http://www.spacex.com/falcon9.php#merlin_engine)  
[Accessed 21 July 2012].
- Spectra-Physics, 2002. *Spectra-Physics Stabilite Series Laser Beam Specifications*.  
[Online]  
Available at: <http://assets.newport.com/webDocuments-EN/images/11987.pdf>  
[Accessed 22 July 2012].
- Sun, H., Catoire, L. & Law, C. K., 2008. Thermal Decomposition of Monomethylhydrazine: Shock Tube Experiments and Kinetic Modeling. *International Journal of Chemical Kinetics*, pp. 176-186.
- Sutton, G. P. & Biblarz, O., 2001. *Rocket Propulsion Elements, 7th Edition*. s.l.:John Wiley & Sons.
- Taylor, G., 1959. *The dynamics of thin sheets of fluid III. Disintegration of fluid sheets*. London, The Royal Society, pp. 33-321.
- Technology, N. I. o. S. a., 2011. *Thermophysical Properties of Fluid Systems*.  
[Online]  
Available at: <http://webbook.nist.gov/chemistry/fluid/>  
[Accessed 20 July 2012].
- TSI INC., 2005. *Phase Doppler Particle Analyzer (PDPA)/ Laser Doppler Velocimeter (LDV) Operations Manual*. Shoreview: TSI INC..
- Welberger, P. & Cartellieri, W., 1987. Fuel Injection and Combustion Phenomena in a High Speed D.I. Diesel Engine Observed by Means of Endoscopic High Speed Photography. *Society of Automotive Engineering*.
- Wicker, J. M., Yoon, M. W. & Yang, V., 1995. Linear and Nonlinear Pressure Oscillations in Baffled Combustion Chambers. *Journal of Sound and Vibration*, pp. 141-172.
- Yang, V., Wicker, J. M. & Myong, Y. W., 1995. Acoustic Waves In Combustion Chambers. In: *Liquid Rocket Engine Combustion Instability*. s.l.:AIAA, pp. 357-376.
- Yodiz, C. W., 1968. Engines for Manned Spacecraft. *AIAA*, pp. 68-567.

## Appendix A: Data for Different Recess Designs and Varying Pressure

### A.1 Data for Recess Design 1

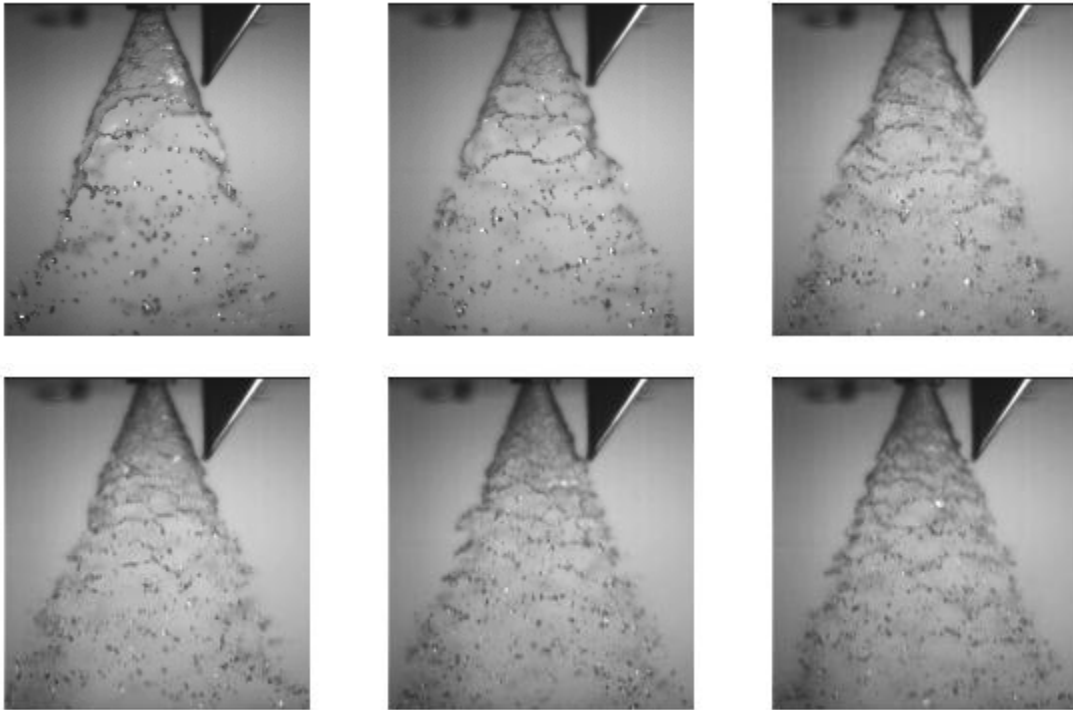


Figure 45: High Speed images of spray breakup for Recessed Length 1 at 12 kHz. Injection pressures are at 68.98, 137.90 and 206.84 kPa (left to right, top panel), and 275.79, 344.74, 413.68 kPa, (left to right, bottom panel) collected at 12 kHz

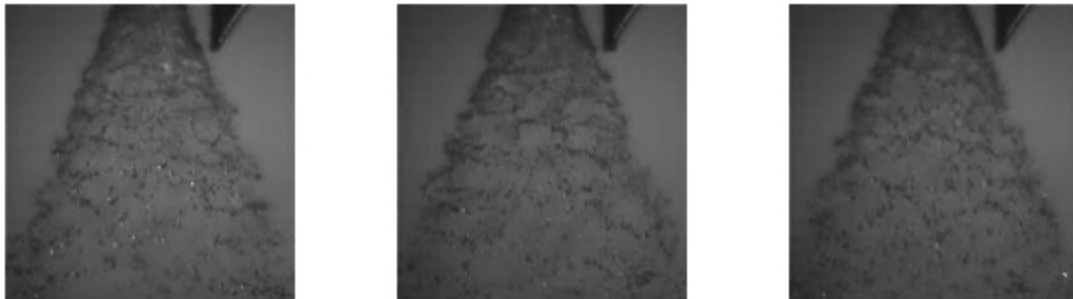


Figure 46: High Speed images of spray breakup for Recessed Length 1 at 20 kHz. Injection pressures are at 482.63, 551.85 kPa, and 620 kPa from left to right.

### A.2 Data for Recess Design 2



Figure 47: High Speed images of spray breakup for Recessed Length 2 at 12 kHz. Injection pressures are at 68.98, 137.90 and 206.84 kPa (left to right, top panel), and 275.79, 344.74, 413.68 kPa, (left to right, bottom panel) collected at 12 kHz

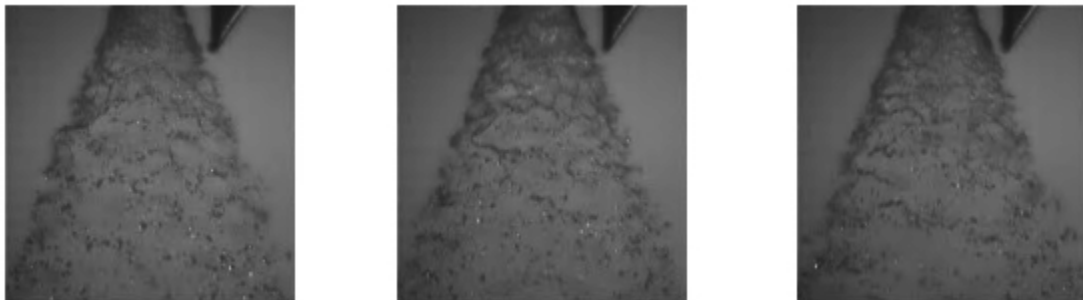


Figure 48: High Speed images of spray breakup for Recessed Length 2 at 20 kHz. Injection pressures are at 482.63, 551.85 kPa, and 620 kPa from left to right.

### A.3 Data for Recess Design 3

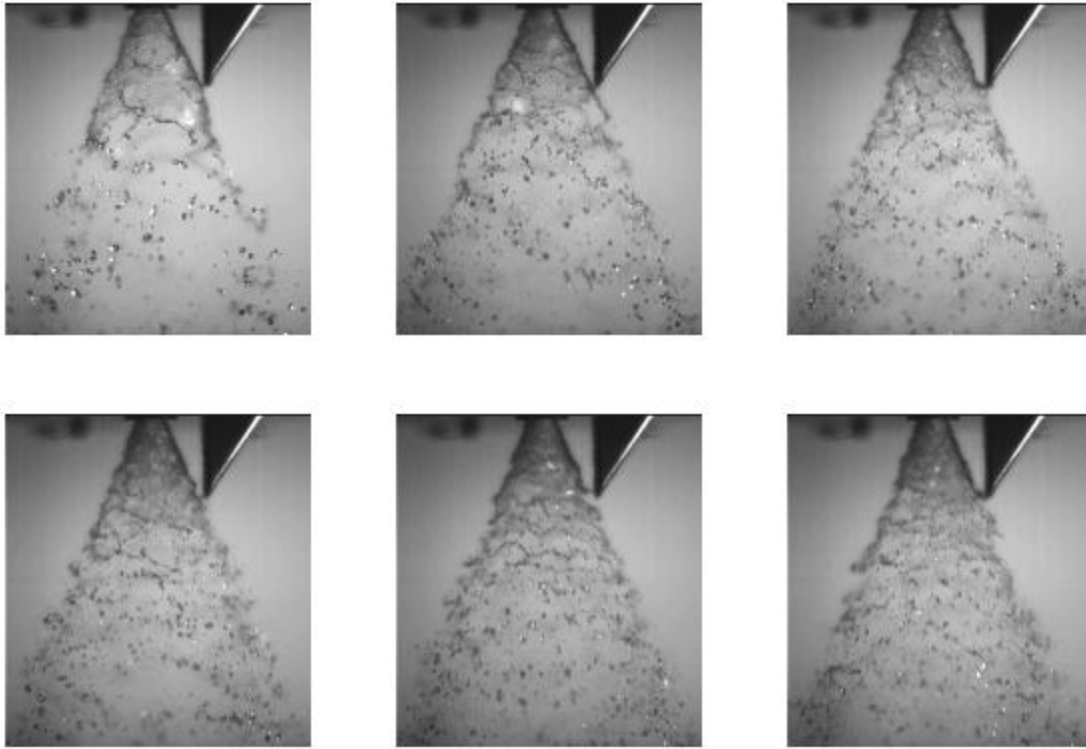


Figure 49: High Speed images of spray breakup for Recessed Length 3 at 12 kHz. Injection pressures are at 68.98, 137.90 and 206.84 kPa (left to right, top panel), and 275.79, 344.74, 413.68 kPa, (left to right, bottom panel) collected at 12 kHz



Figure 50: High Speed images of spray breakup for Recessed Length 3 at 20 kHz. Injection pressures are at 482.63, 551.85 kPa, and 620 kPa from left to right.

#### A.4 Data for Recess Design 4

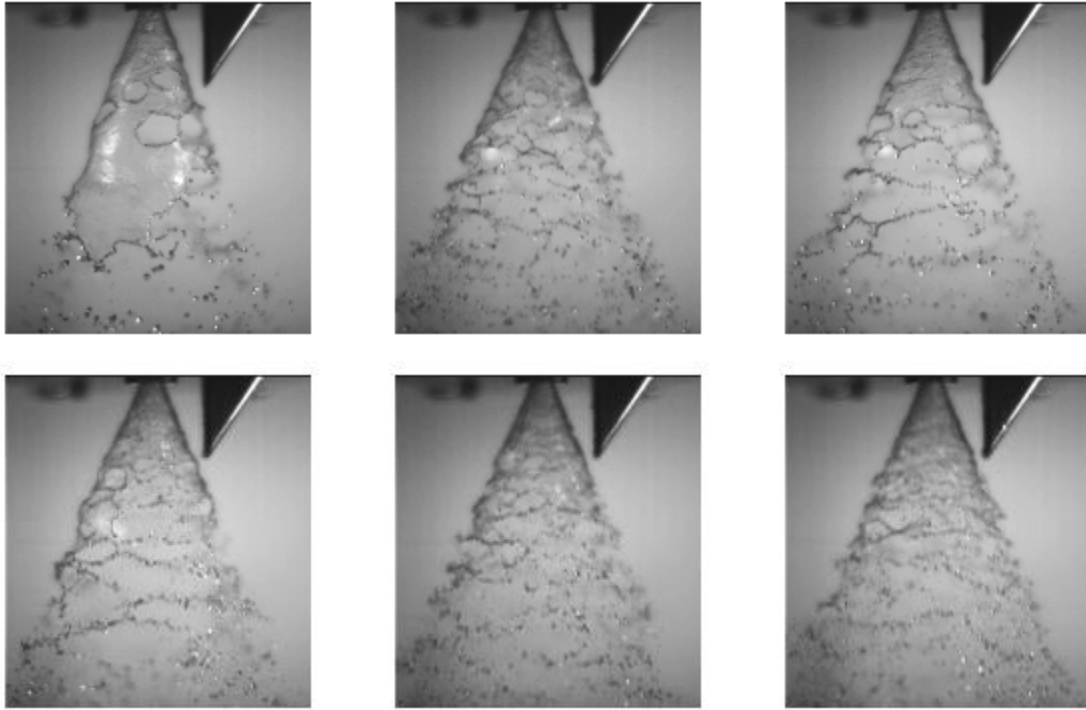


Figure 51: High Speed images of spray breakup for Recessed Length 4 at 12 kHz. Injection pressures are at 68.98, 137.90 and 206.84 kPa (left to right, top panel), and 275.79, 344.74, 413.68 kPa, (left to right, bottom panel) collected at 12 kHz

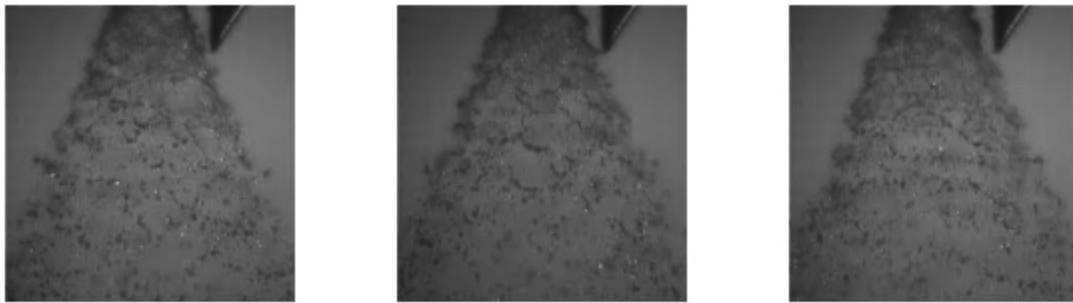


Figure 52: High Speed images of spray breakup for Recessed Length 4 at 20 kHz. Injection pressures are at 482.63, 551.85 kPa, and 620 kPa from left to right.

### A.5 Data for Recess Design 5

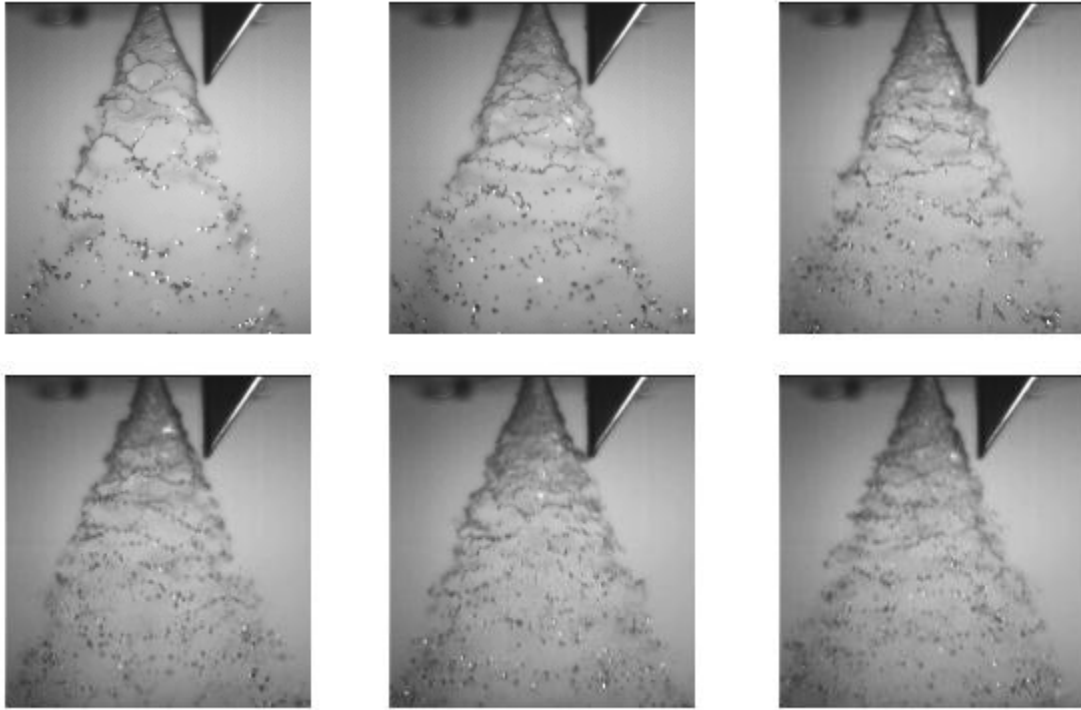


Figure 53: High Speed images of spray breakup for Recessed Length 5 at 12 kHz. Injection pressures are at 68.98, 137.90 and 206.84 kPa (left to right, top panel), and 275.79, 344.74, 413.68 kPa, (left to right, bottom panel) collected at 12 kHz

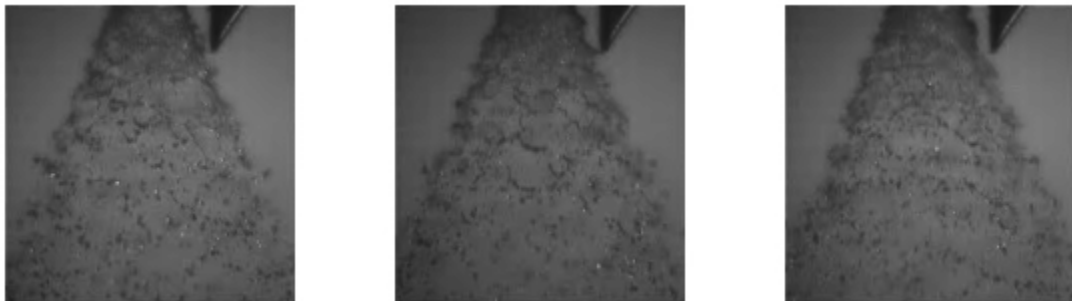


Figure 54: High Speed images of spray breakup for Recessed Length 5 at 20 kHz. Injection pressures are at 482.63, 551.85 kPa, and 620 kPa from left to right.

## Appendix B: Data for Different Fluids and Varying Pressure

### B.1 Data for Acetone

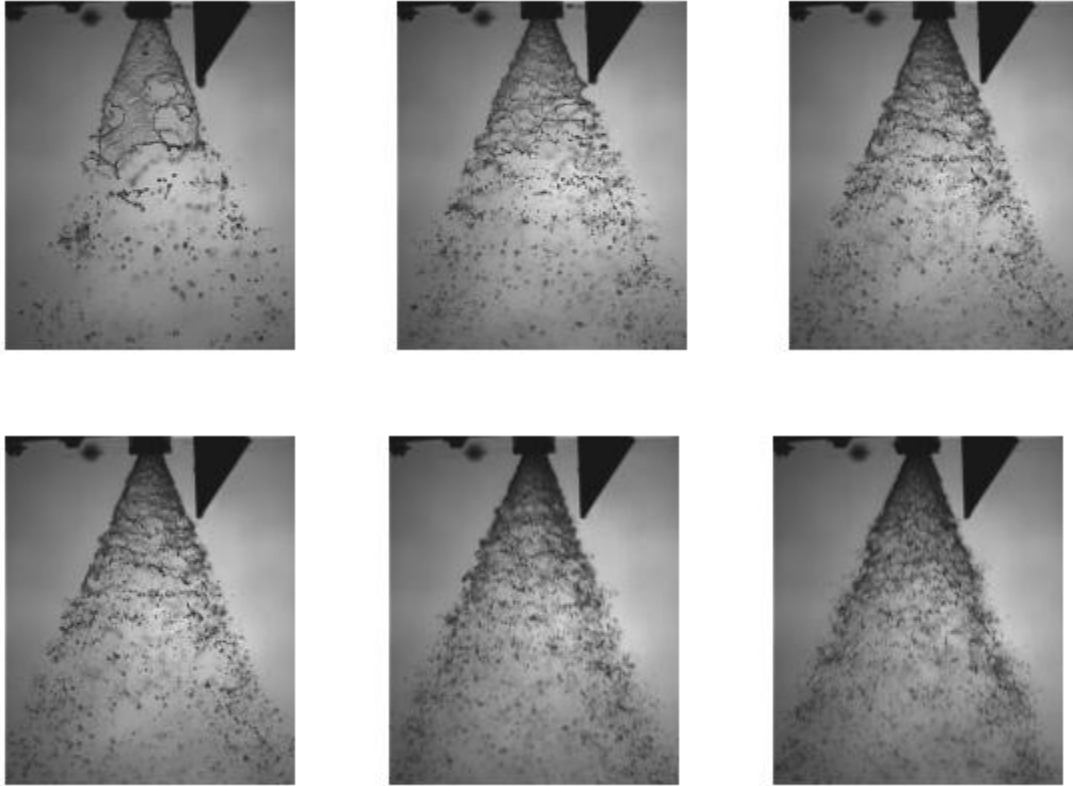


Figure 55: Acetone injected at 34.5, 69.0, 137.9 kPa (left to right, top panel), and 207, 276, and 345 kPa, (left to right, bottom panel) collected at 12 kHz.

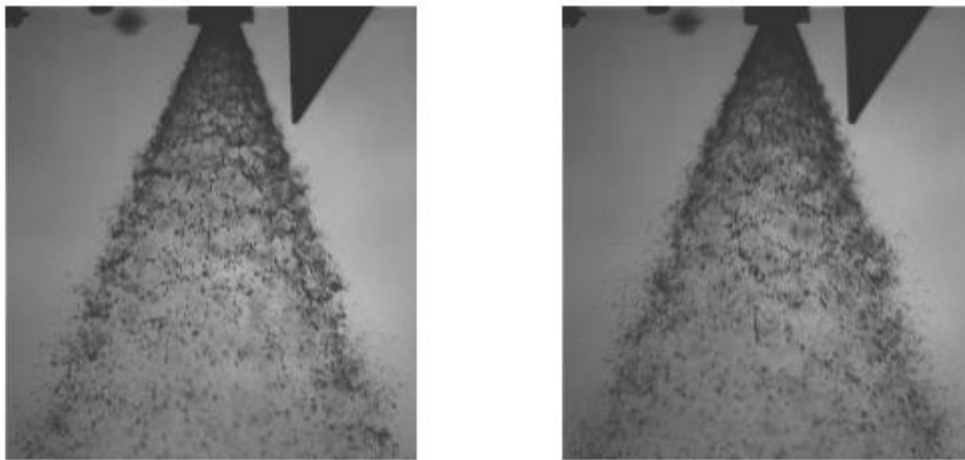


Figure 56: Acetone injected at 413.68 (left panel) and 482.63 kPa (right panel) collected at 20 kHz

## B.2 Data for Methanol

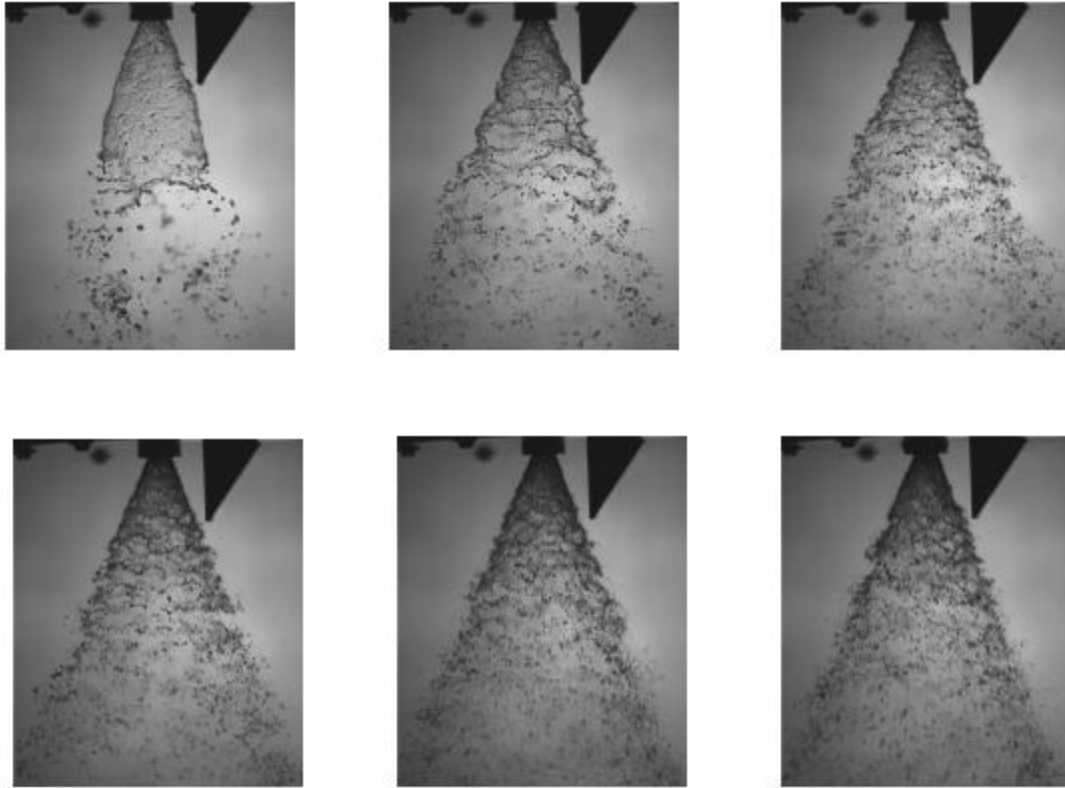


Figure 57: Methanol injected at 34.47, 68.98, 137.90 kPa (left to right, top panel), and 206.84, 275.79, and 344.74 kPa, (left to right, bottom panel) collected at 12 kHz

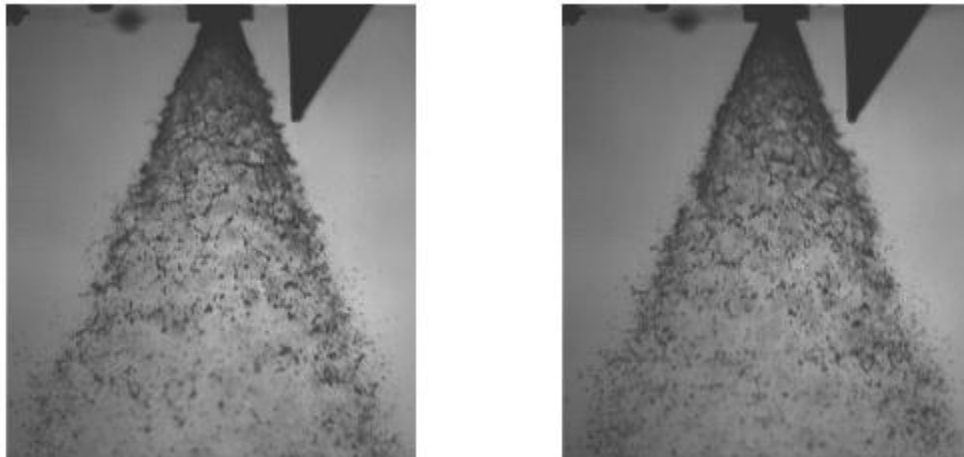


Figure 58: Methanol injected at 413.68 (left panel) and 482.63 kPa (right panel) collected at 20 kHz

### B.3 Data for JP-8

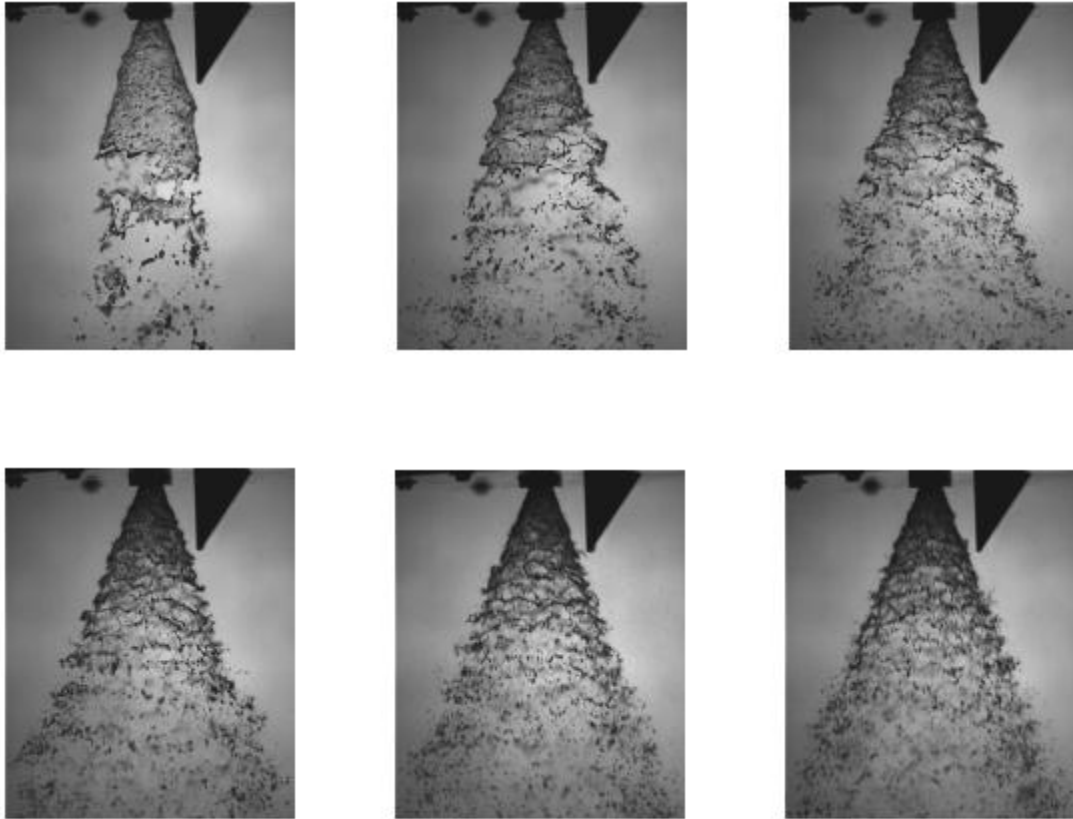


Figure 59: JP-8 injected at 34.47, 68.98, 137.90 kPa (left to right, top panel), and 206.84, 275.79, and 344.74 kPa, (left to right, bottom panel) collected at 12 kHz

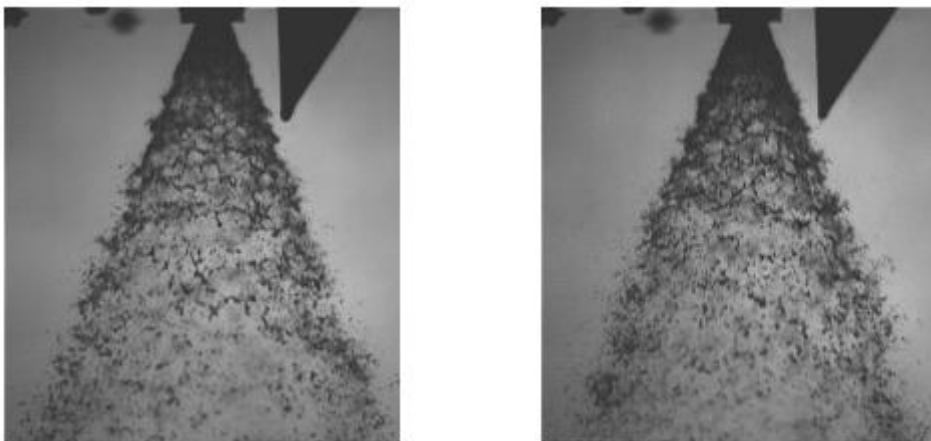


Figure 60: JP-8 injected at 413.68 (left panel) and 482.63 kPa (right panel) collected at 20 kHz

#### B.4 Data for Water

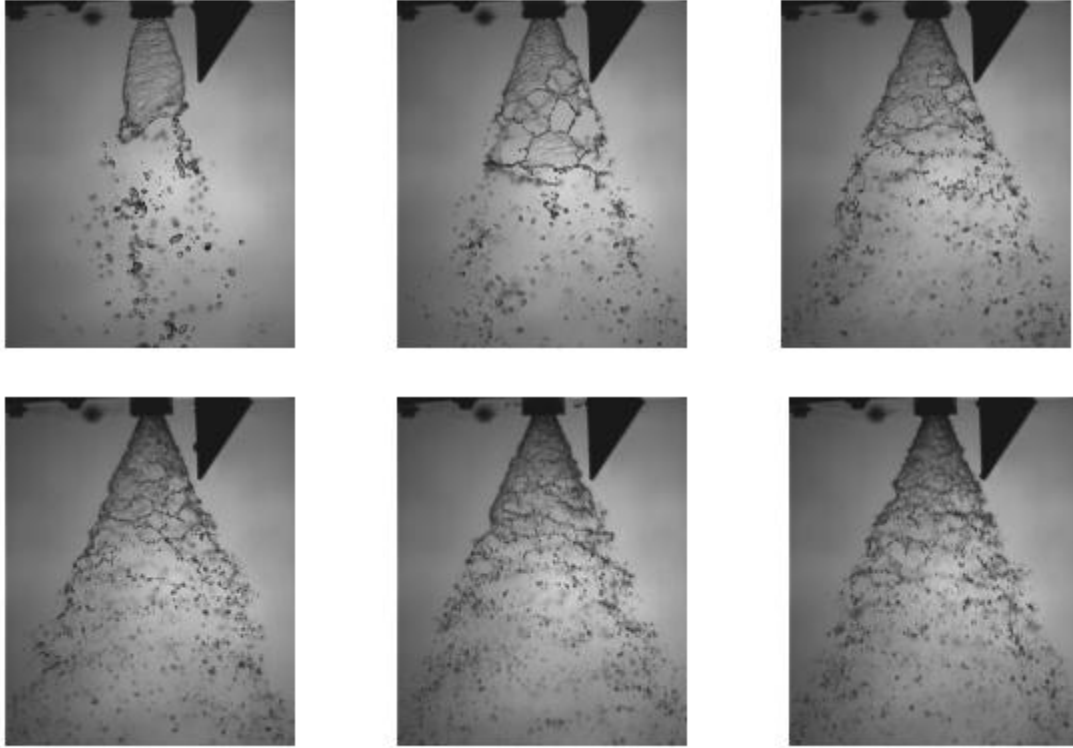


Figure 61: Water injected at 34.47, 68.98, 137.90 kPa (left to right, top panel), and 206.84, 275.79, and 344.74 kPa, (left to right, bottom panel) collected at 12 kHz

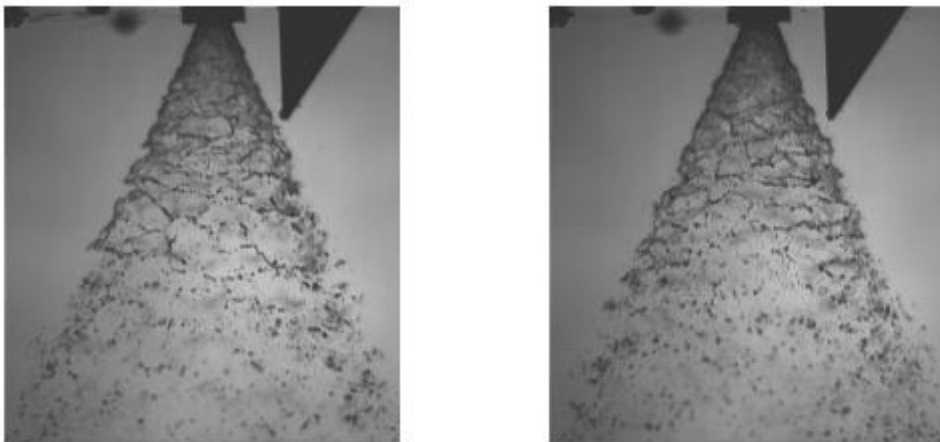


Figure 62: Water injected at 413.68 (left panel) and 482.63 kPa (right panel) collected at 20 kHz

## Appendix C: PDPA data

### C.1 Effects of Fluid Properties on Droplet Velocity

#### C.1.1 Mean Axial Velocity, 25mm from injector exit

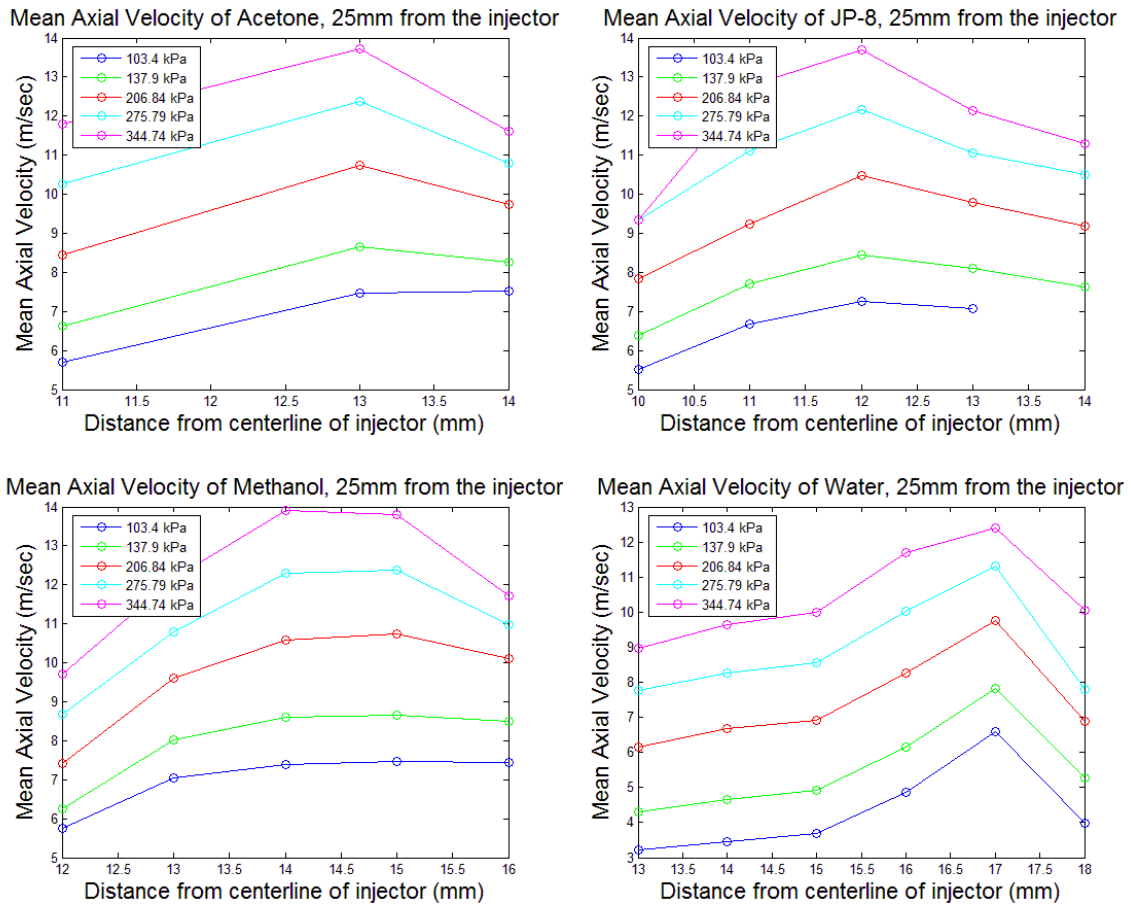


Figure 63: Comparison of median axial velocities 25 mm from injector exit.

### C.1.2 Mean Axial Velocity, 50 mm from injector exit

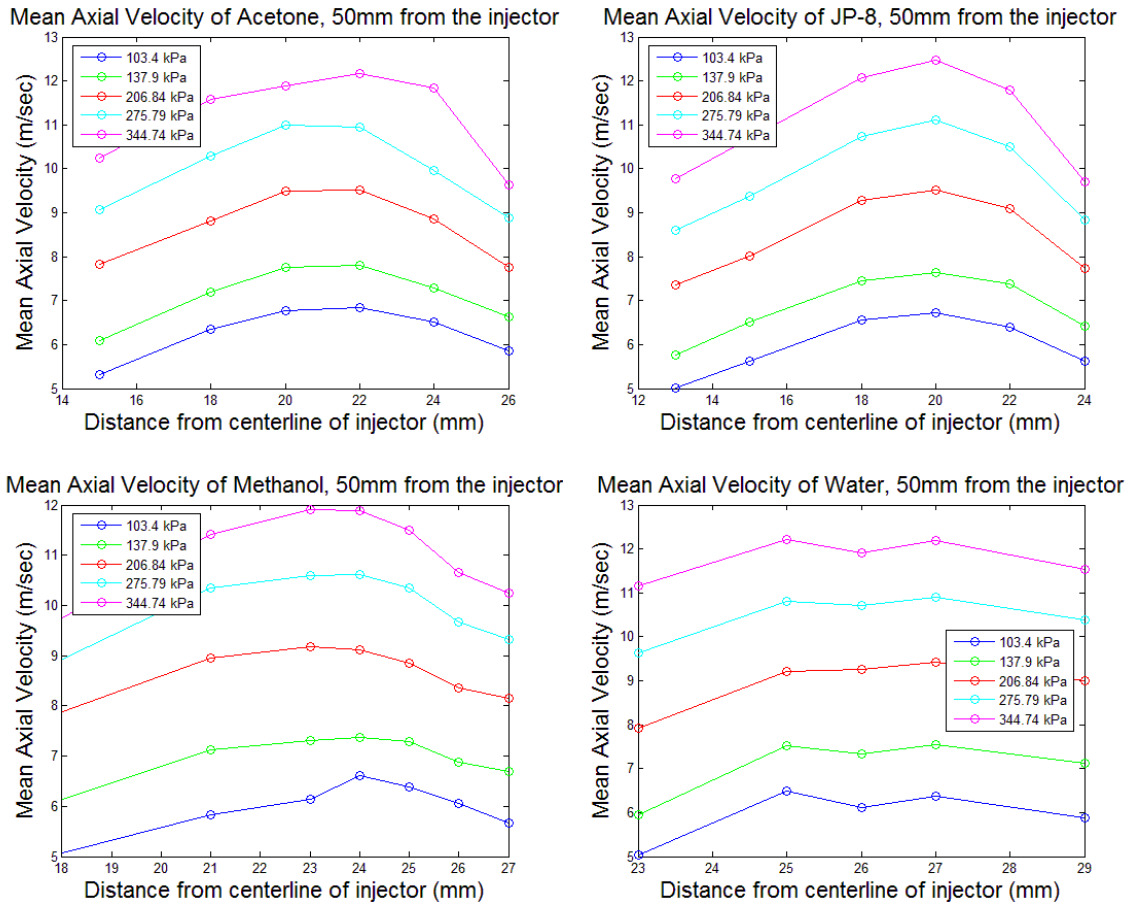
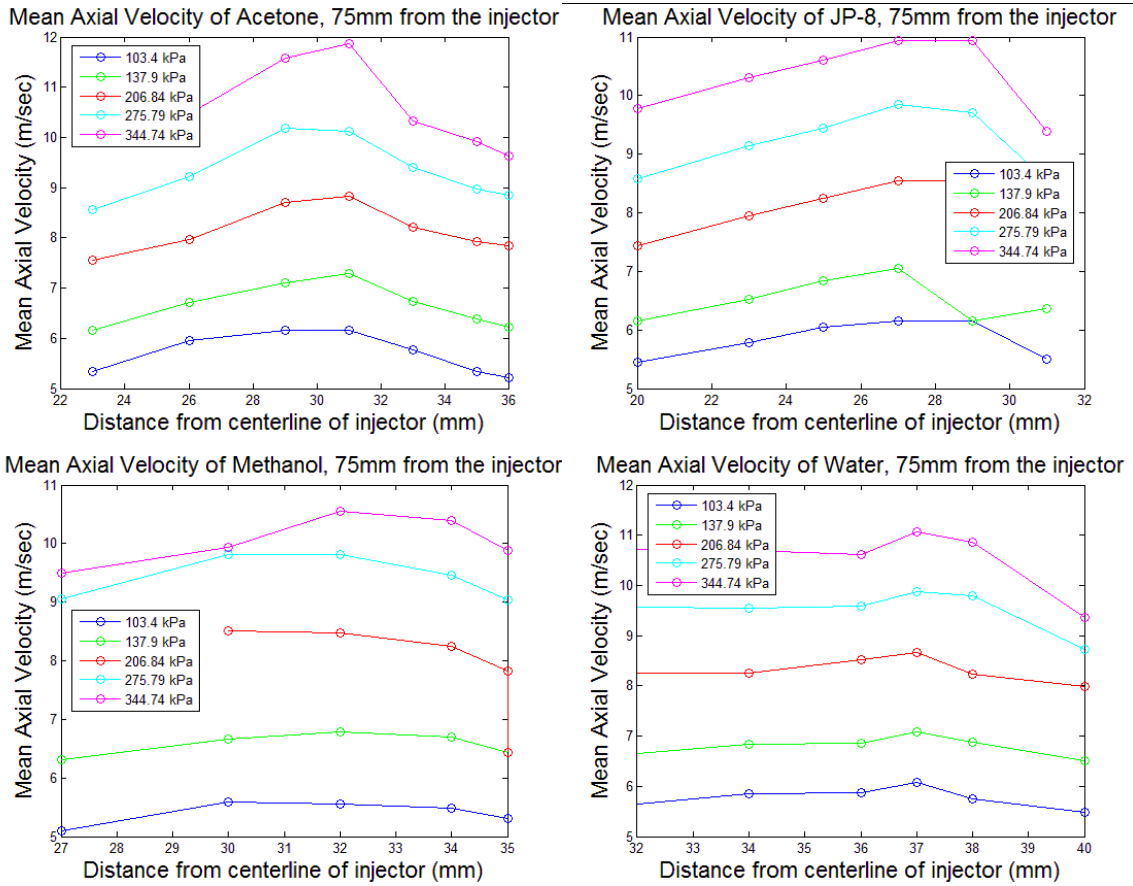


Figure 64: Comparison of median axial velocities 50 mm from injector exit.

**C.1.3 Mean Axial Velocity, 75 mm from injector exit**

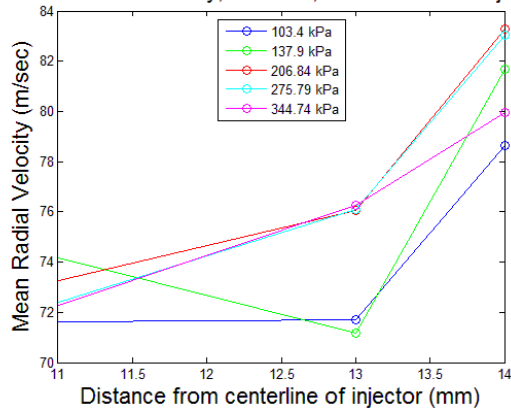


**Figure 65: Comparison of median axial velocities 75 mm from injector exit.**

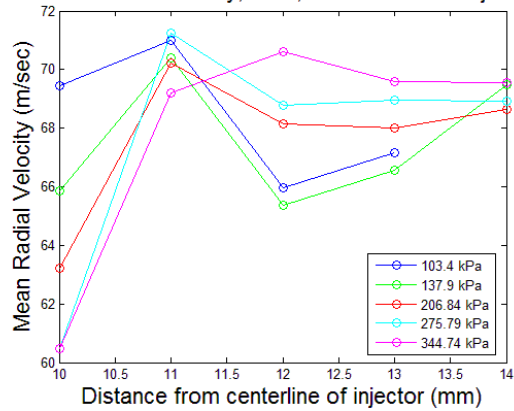
## C.2 Effects of Fluid Properties on Droplet Velocity

### C.2.1 Mean Radial Velocity, 25mm from Injector Exit

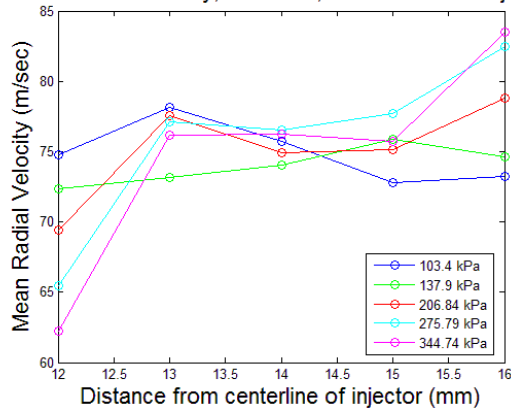
Mean Radial Velocity, Acetone, 25mm from the injector



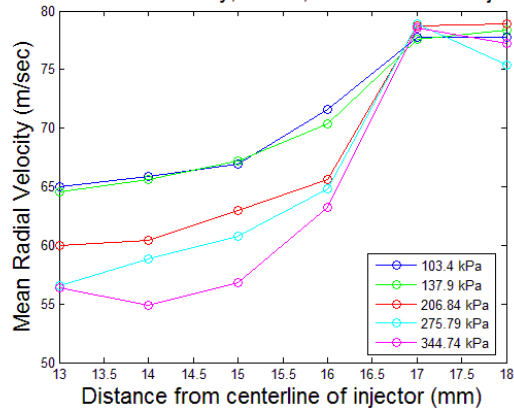
Mean Radial Velocity, JP-8, 25mm from the injector



Mean Radial Velocity, Methanol, 25mm from the injector

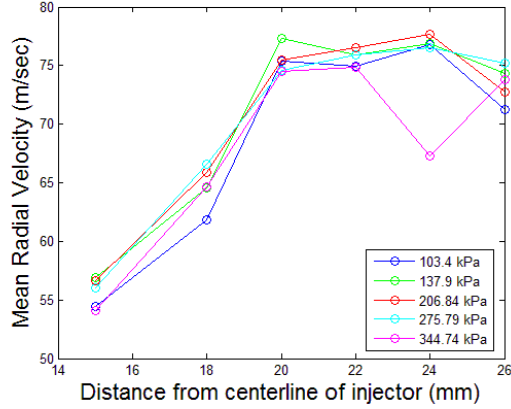


Mean Radial Velocity, Water, 25mm from the injector

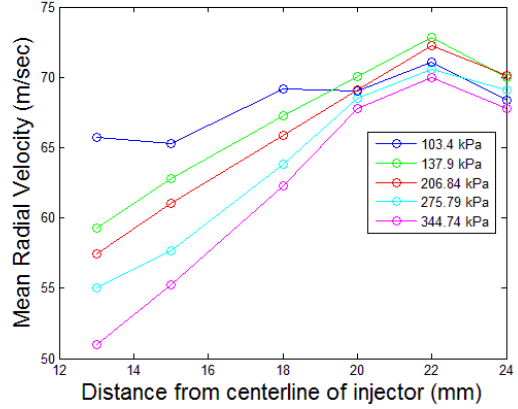


### C.2.2 Mean Radial Velocity, 50mm from injector exit

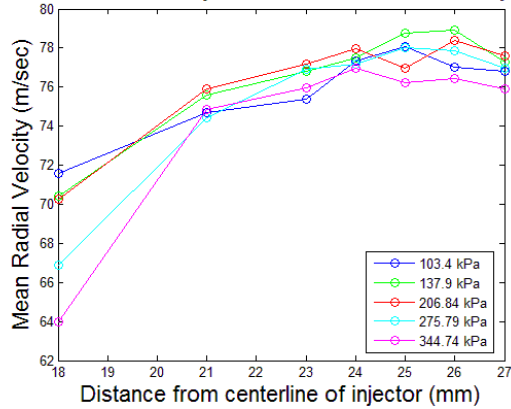
Mean Radial Velocity, Acetone, 50mm from the injector



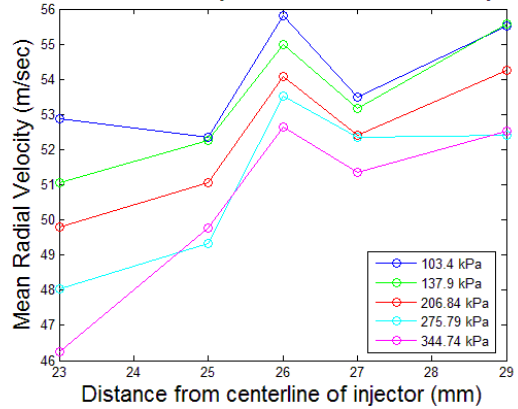
Mean Radial Velocity, JP-8, 50mm from the injector



Mean Radial Velocity, Methanol, 50mm from the injector

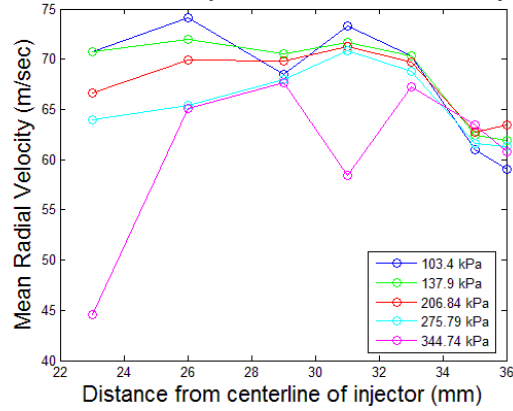


Mean Radial Velocity, Water, 50mm from the injector

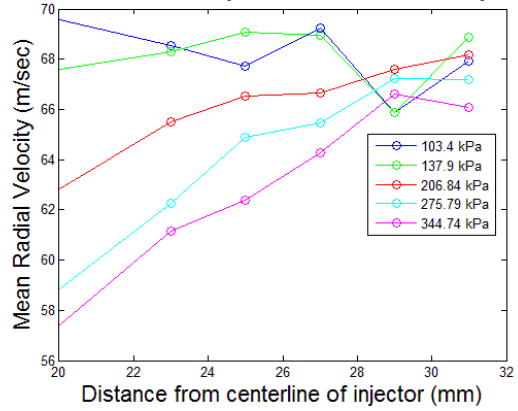


### C.2.3 Mean Radial Velocity, 75mm from injector exit

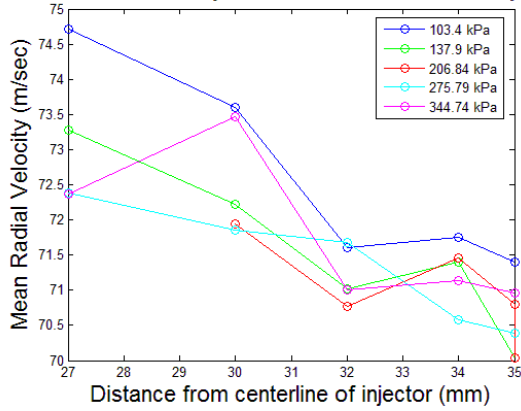
Mean Radial Velocity, Acetone, 75mm from the injector



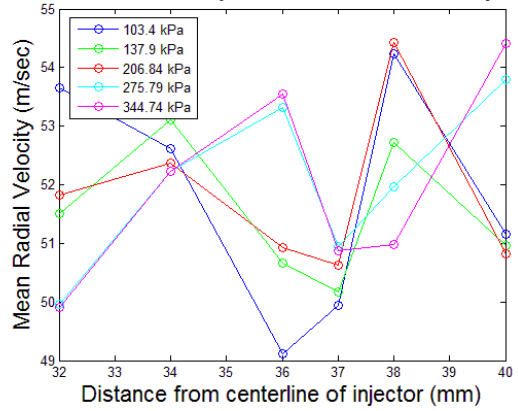
Mean Radial Velocity, JP-8, 75mm from the injector



Mean Radial Velocity, Methanol, 75mm from the injector



Mean Radial Velocity, Water, 75mm from the injector



### C.3 Composite Velocity Magnitude

#### C.3.1 Composite Velocity Magnitude, 25 mm from injector exit

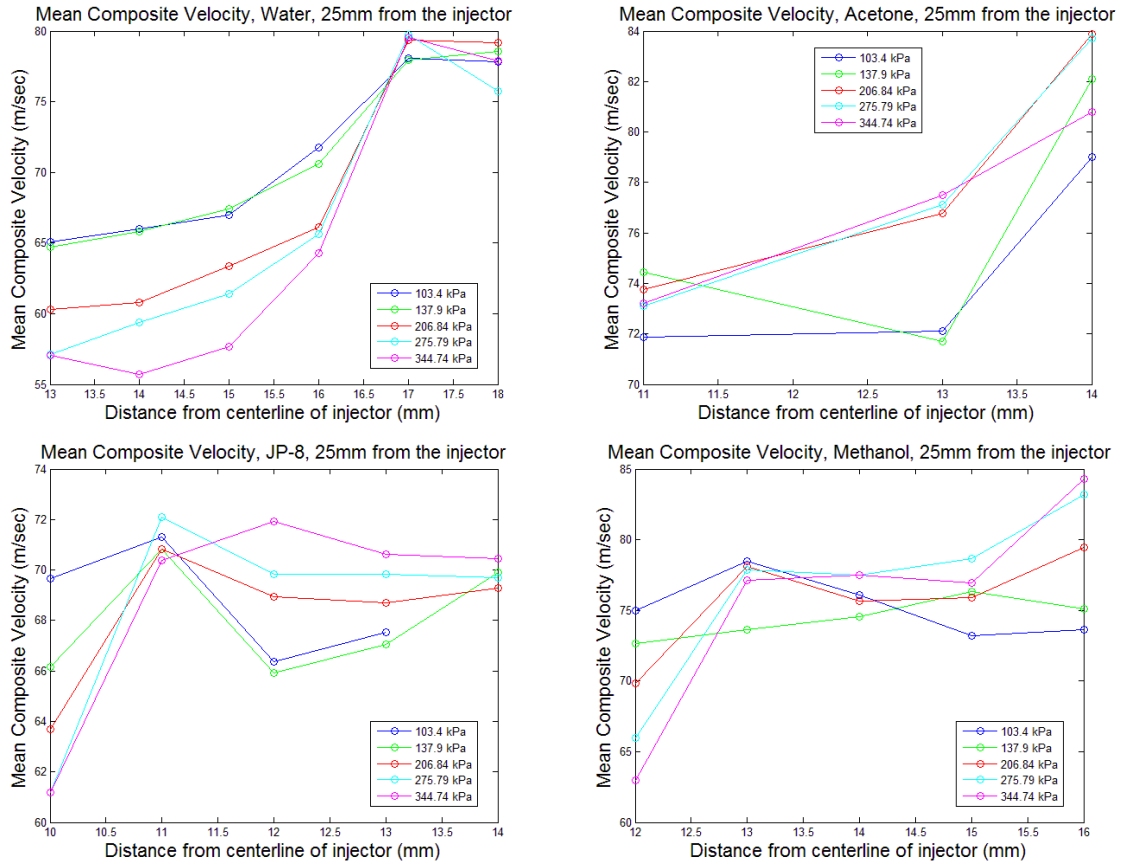


Figure 66: Comparison of composite velocity magnitude, 25 mm from the injector exit.

### C.3.2 Composite Velocity Magnitude, 50 mm from injector exit

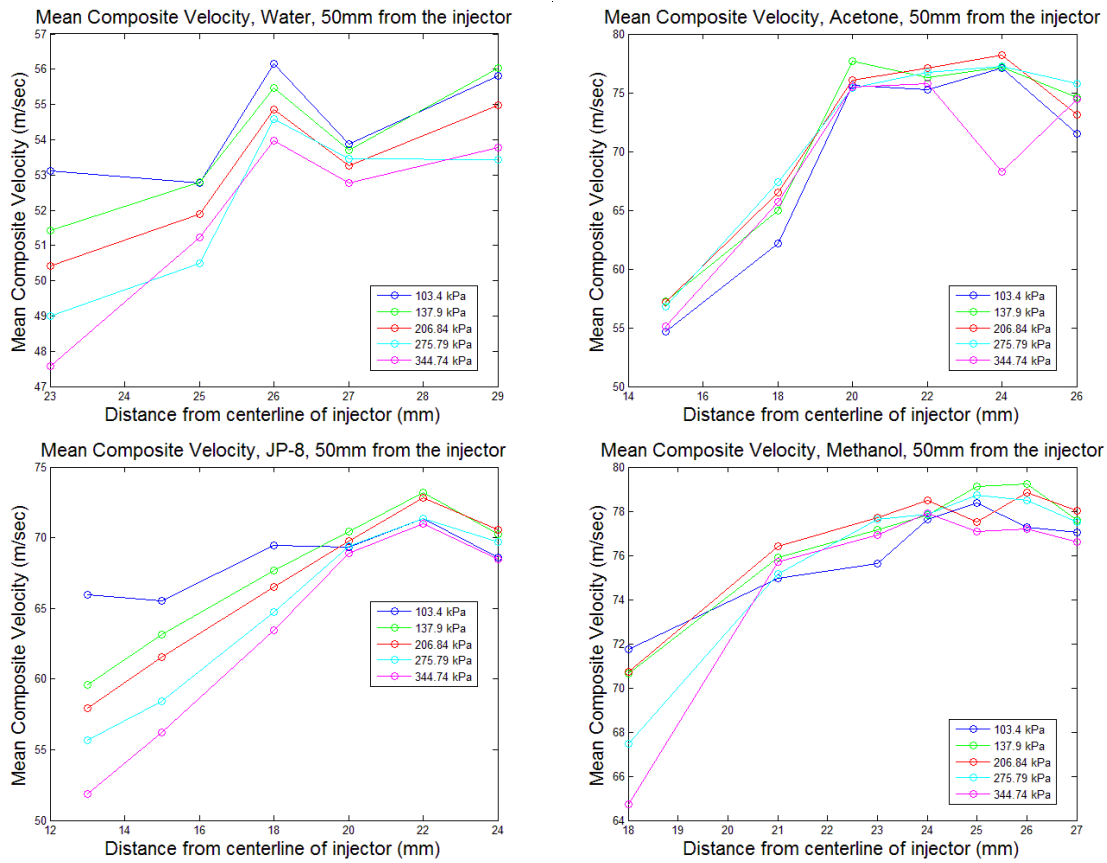


Figure 67: Comparison of composite velocity magnitude, 50 mm from the injector exit.

### C.3.3 Composite Velocity Magnitude, 75 mm from injector exit

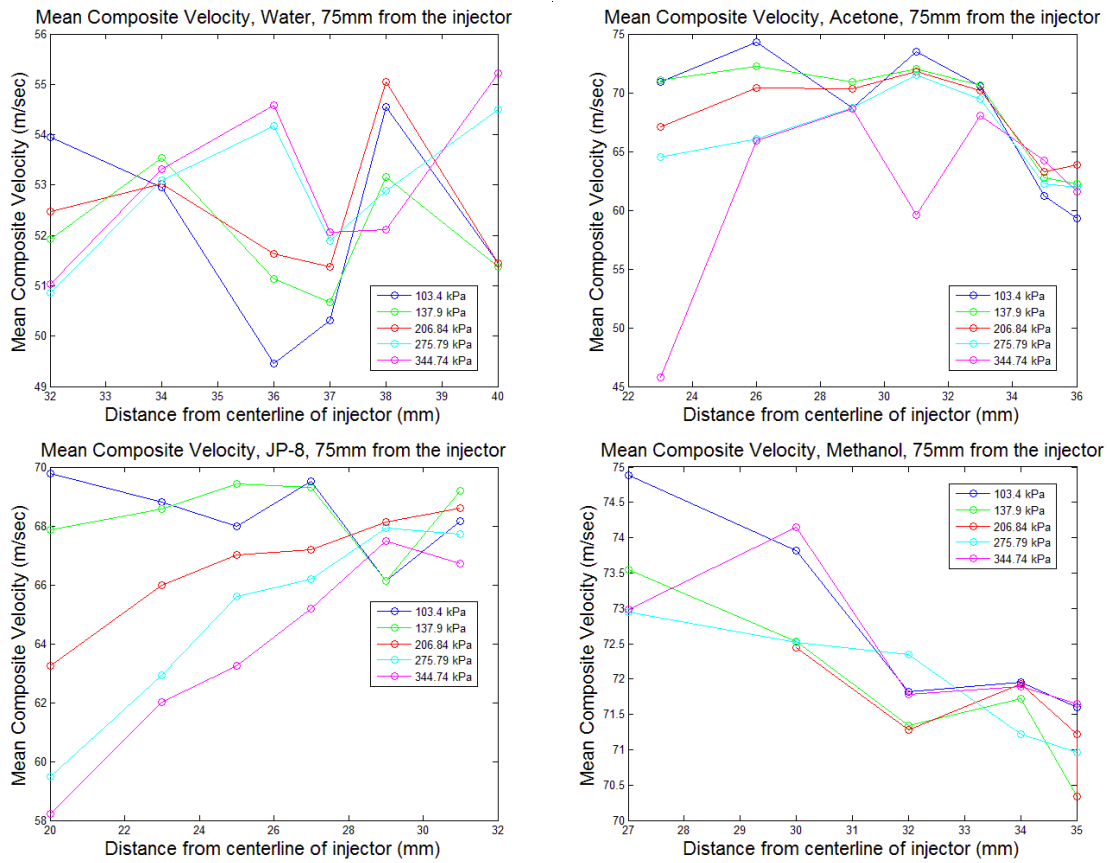


Figure 68: Comparison of composite velocity magnitude, 75 mm from the injector exit.

### C.4 Effects of Fluid Properties on Sauter Mean Diameter (SMD)

#### C.4.1 SMD of fluids at 25 mm from injector exit

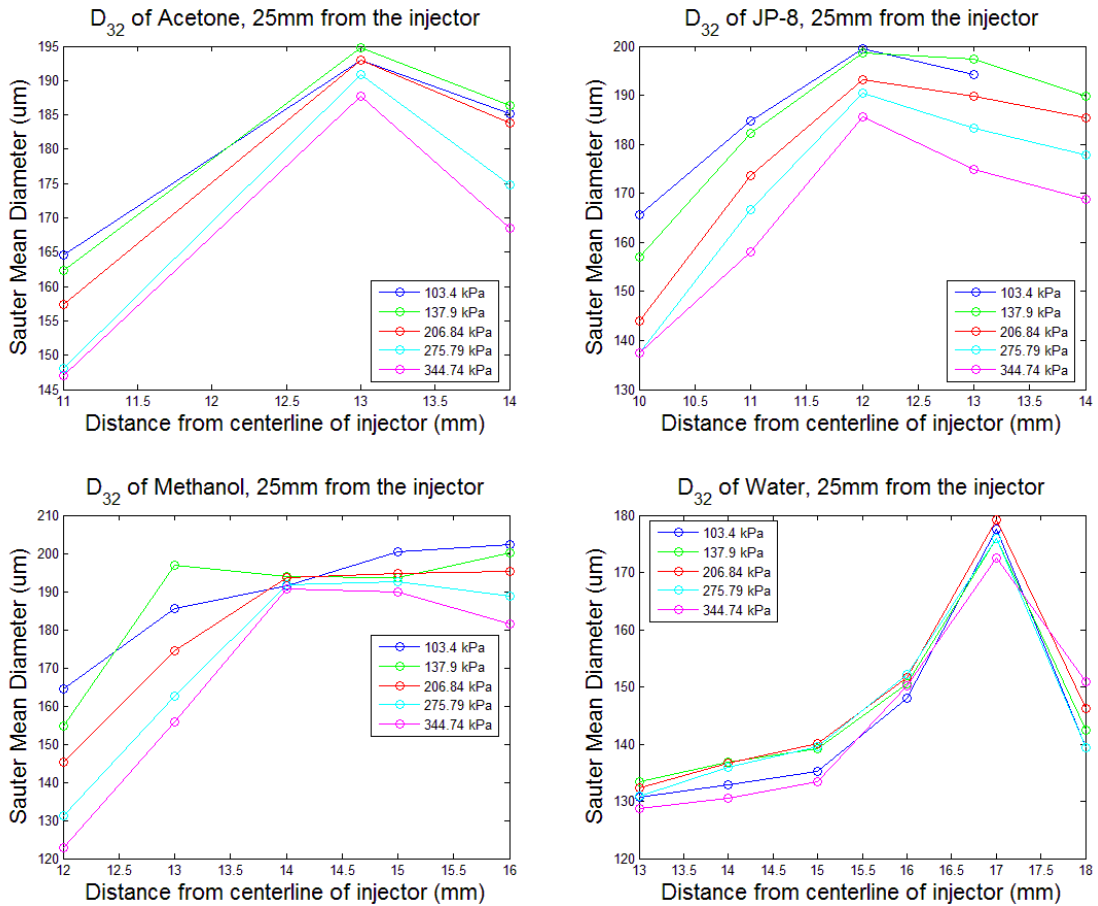


Figure 69: Comparison of Sauter Mean Diameters 25 mm from the injector exit.

### C.4.2 SMD of fluids 50 mm from injector exit

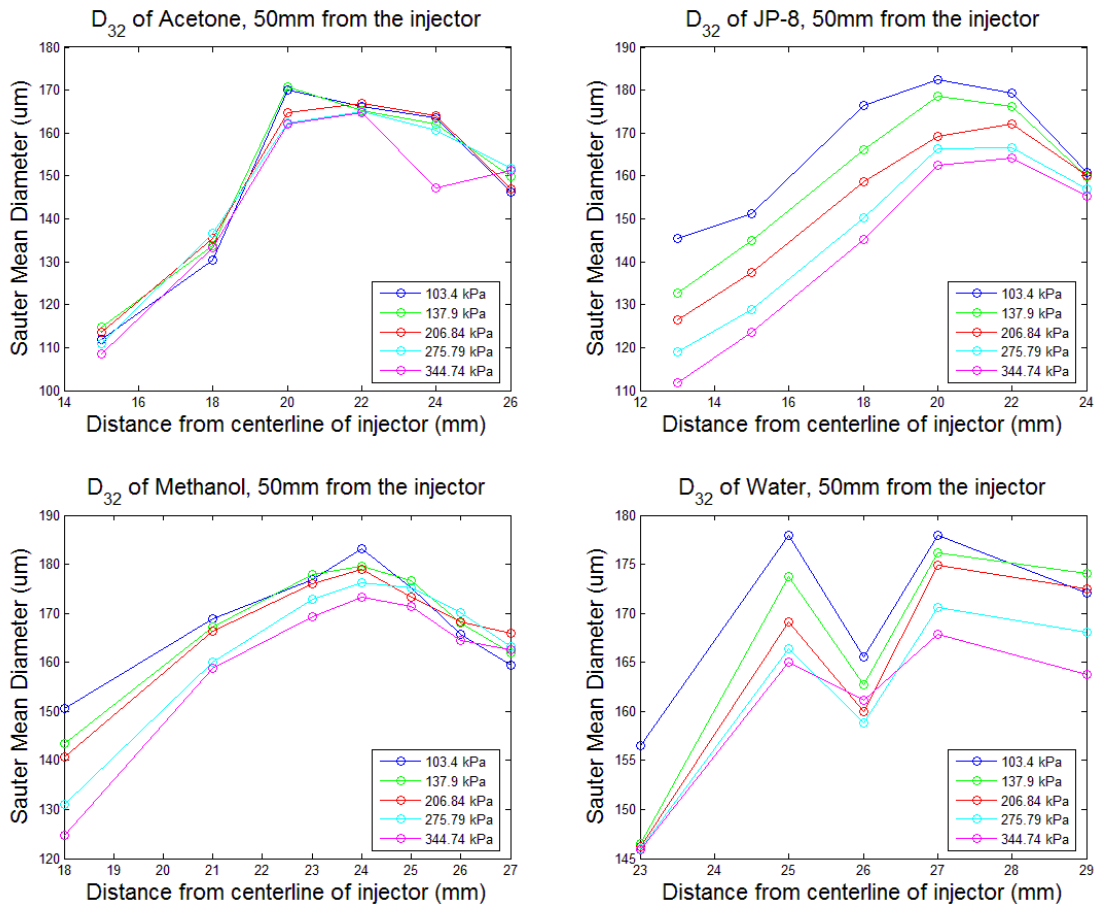


Figure 70: Comparison of Sauter Mean Diameters 50 mm from the injector exit.

### C.4.3 SMD of fluids 75 mm from injector exit

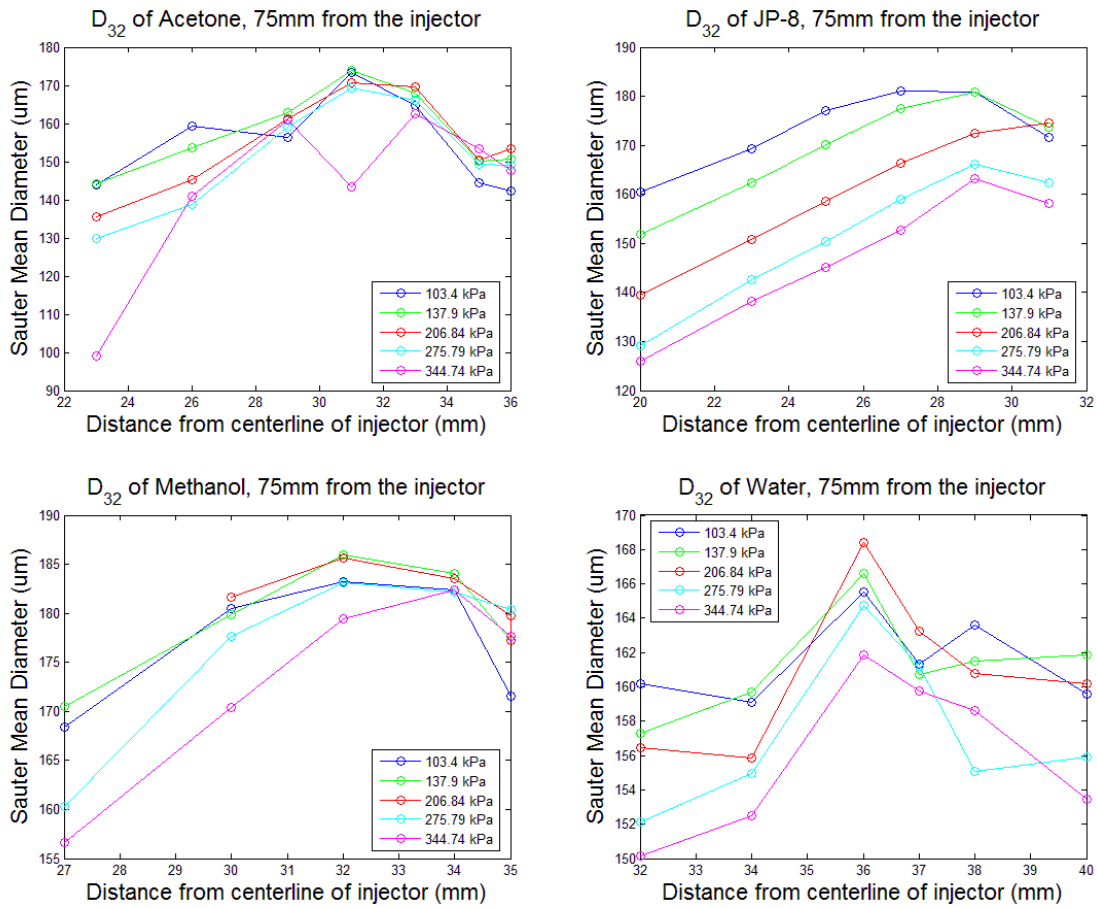


Figure 71: Comparison of Sauter Mean Diameters 75 mm from the injector exit.

### C.5 Droplet Weber Number

#### C.5.1 Droplet Weber Number, 25 mm from injector exit

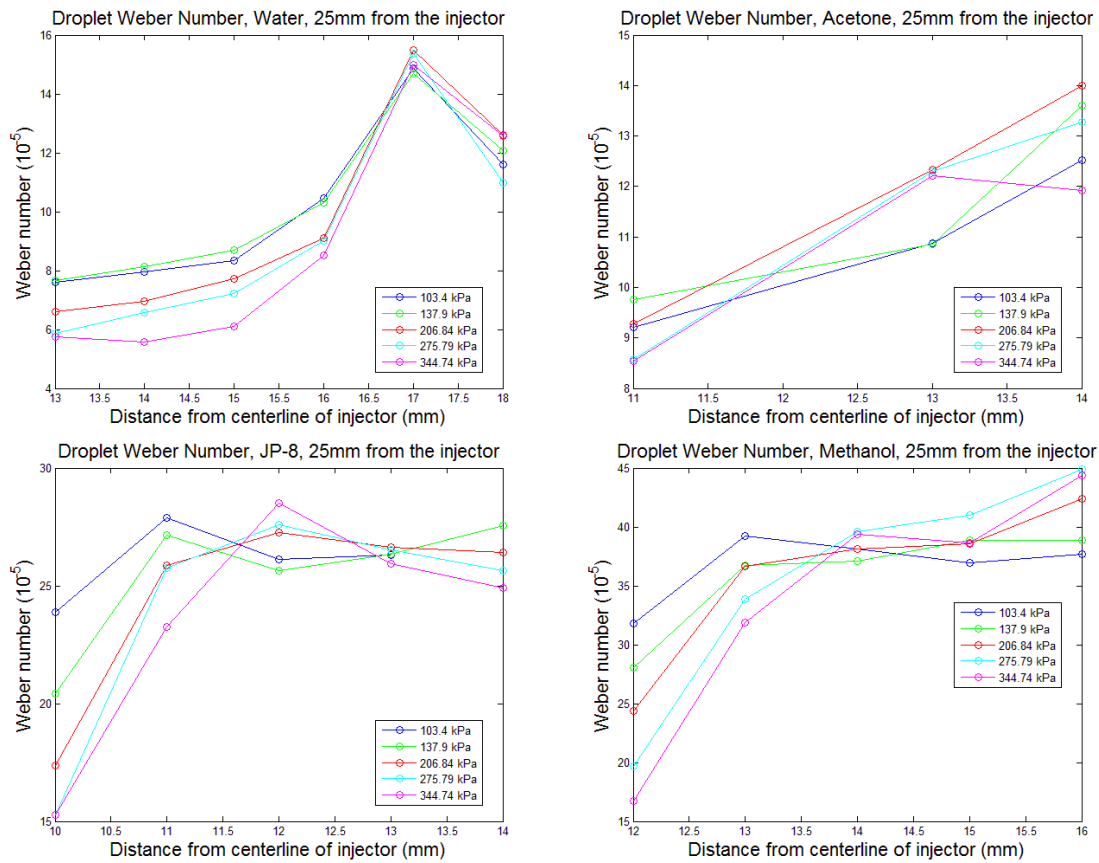


Figure 72: Comparison of Droplet Weber Number, 25mm from the injector exit.

### C.5.2 Droplet Weber Number, 50 mm from injector exit

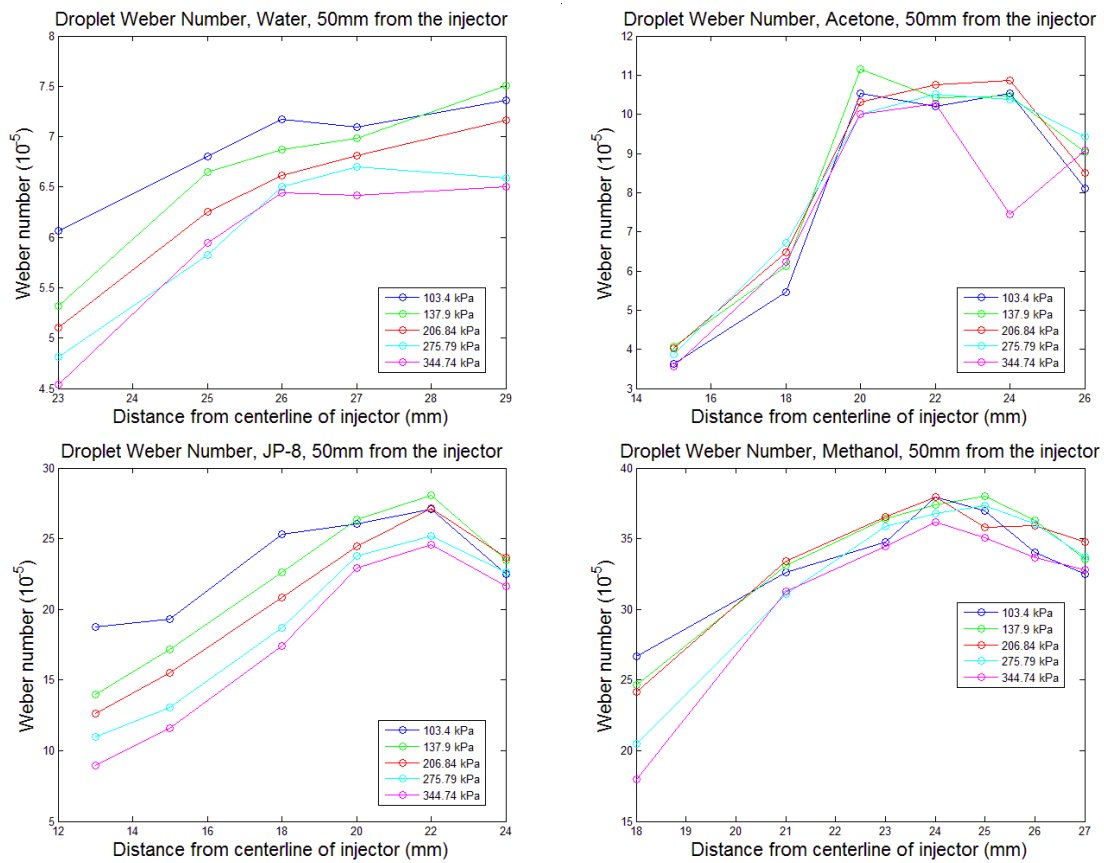


Figure 73: Comparison of Droplet Weber Number, 50 mm from the injector exit.

### C.5.3 Droplet Weber Number, 75 mm from injector exit

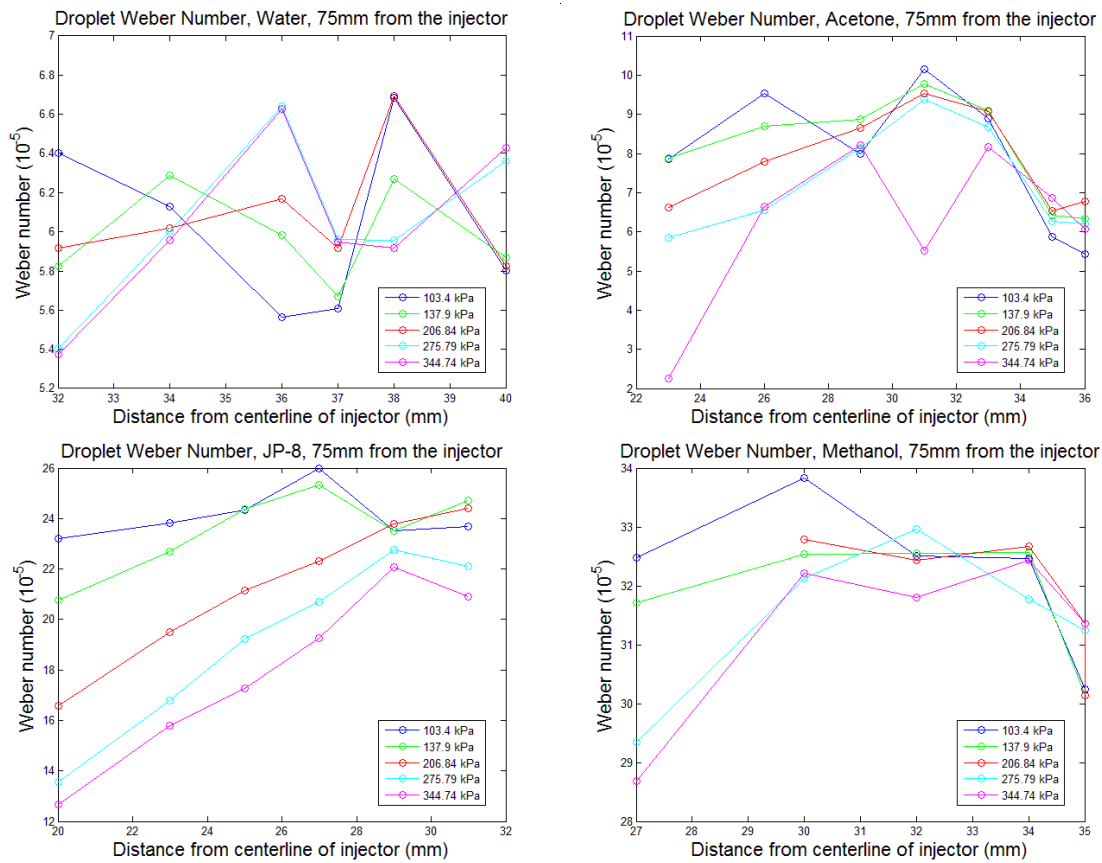


Figure 74: Comparison of Droplet Weber Number, 75 mm from the injector exit.

## C.6 Droplet Reynolds Number

### C.6.1 Droplet Reynolds Number, 25 mm from injector exit

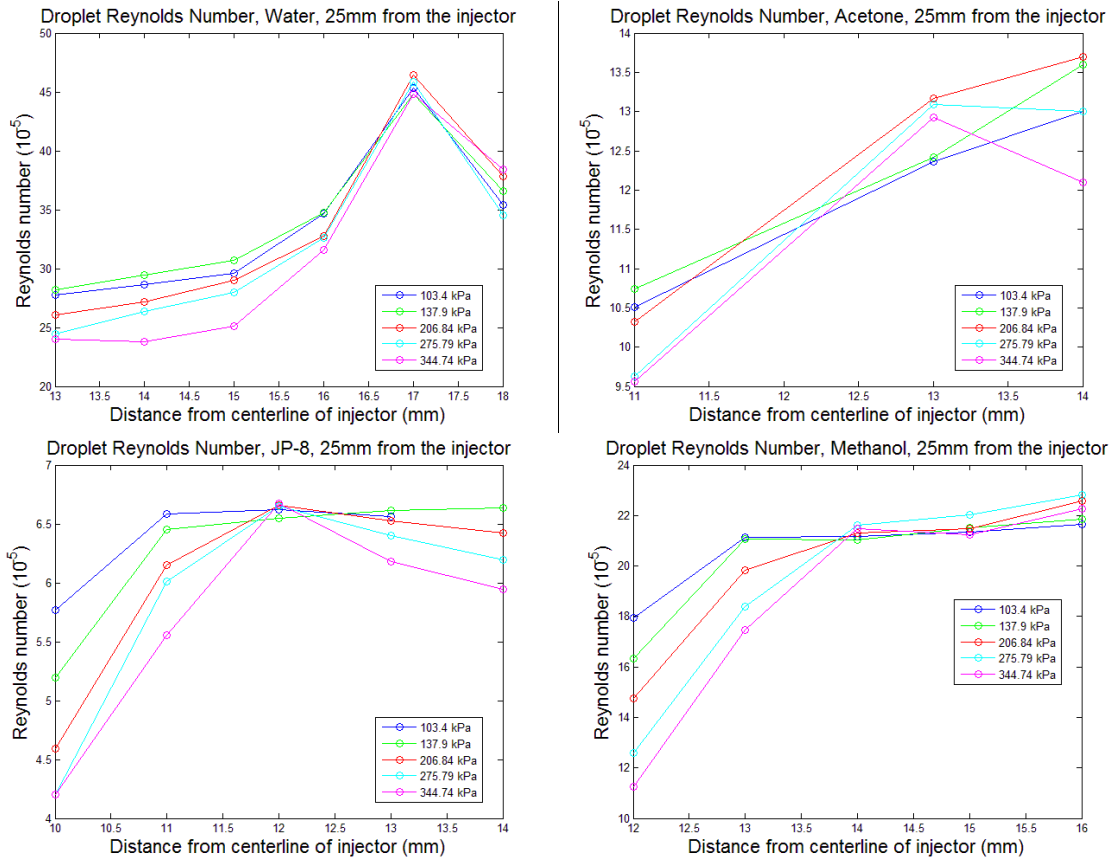


Figure 75: Comparison of Droplet Reynolds Number, 25 mm from the injector exit.

### C.6.2 Droplet Reynolds Number, 50 mm from injector exit

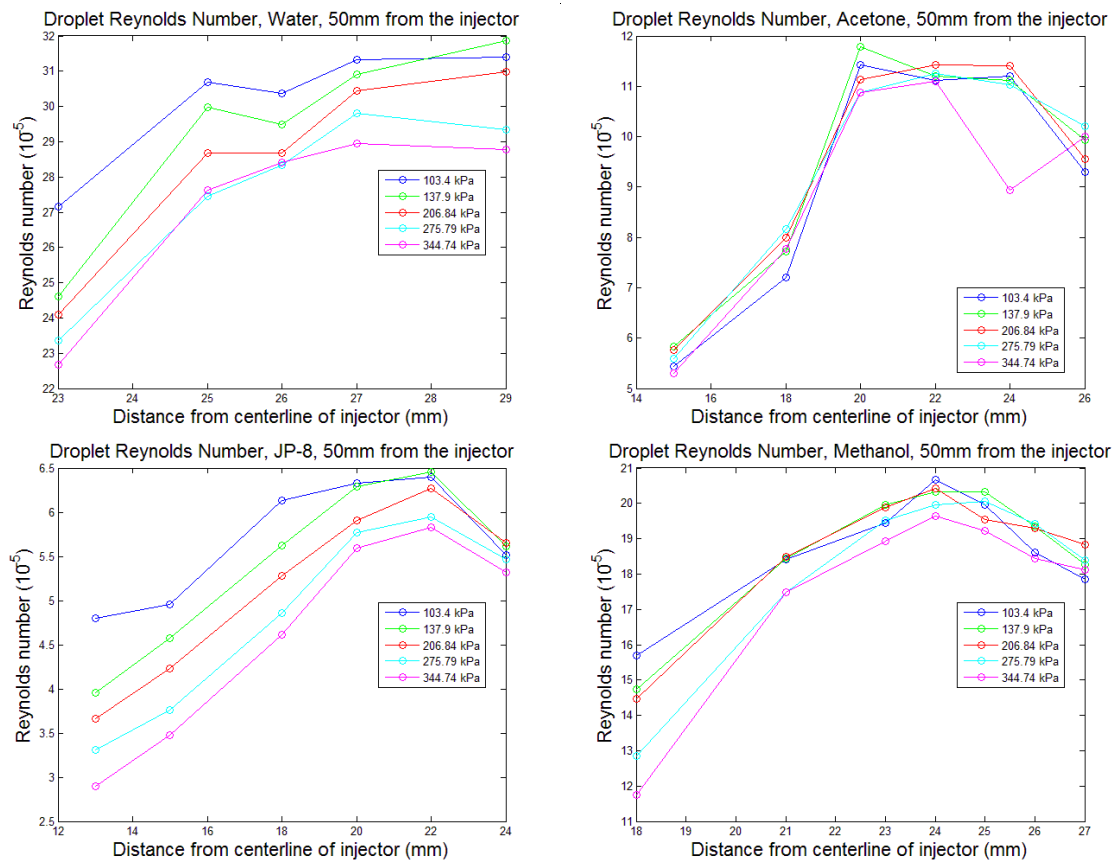


Figure 76: Comparison of Droplet Reynolds Number, 50 mm from the injector exit.

### C.6.2 Droplet Reynolds Number, 75 mm from injector exit

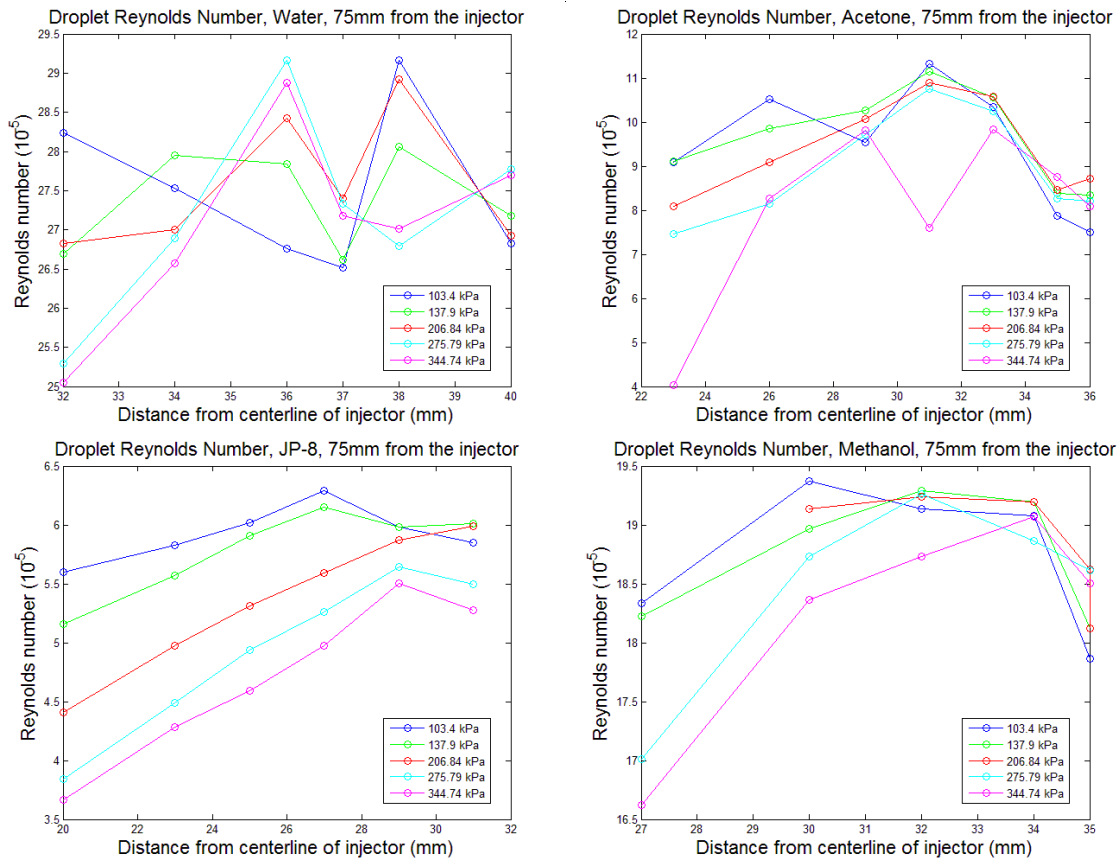


Figure 77: Comparison of Droplet Reynolds Number, 75 mm from the injector exit.

## Appendix D: Code

### D.1 PDPA Data Extraction Code

```

%% PDPA Data Extration
%% Chris Radke - Radke.Christopher@gmail.com
%% November 29, 2012
clc
clear all
close all

fluid=1;           %Fluid number see below

height=25;        %Vertical Distance from Injector exit to PDPA Beam.
Must be 25, 50 or 75

valueofinterest=1; %Value of Interest See Below

%% Value of Interest
% 1 = Velocity Mean Ch.1 - Radial Velocity
% 2 = Velocity Mean Ch.2 - Axial Velocity
% 3 = Velocity RMS Ch. 1 - Radial Velocity
% 4 = Velocity RMS Ch. 2 - - Axial Velocity
% 5 = D32-SMD
% 6 = Diameter RMS
% 7 = Composite Velocity Magnitude
% 8 = Weber Number =rho*v^2*d/sigma
% 9 = Reynolds number= V*D/Nu
% 10= Frequency Plot
%% Fluid
% 1 = water
% 2 = acetone
% 3 = JP8
% 4 = methanol
%%

%Pressures of Interest
psi=[20];
fun=cell(1,length(psi));

%Placeholder count values
counter=1;
counter2=1;
counter3=1;
counter4=1;
counter5=1;
counter6=1;

%Extracts data for all of the pressure for the selected fluid
for n=1:length(psi)
    if fluid==2

```

```

disp('This data is for Acetone')
A1='Acetone';
density=791; %kg/m^3
sigma=.073; %N/m
mu=8.9*10^-4; %Pa*s
PDPA_dir=sprintf('C:\\Users\\... PDPA
Data\\acetone\\acetone\\%spsi\\', num2str(psi(n)));
elseif fluid==1
disp('This data is for Water')
A1='Water';
density=1000; %kg/m^3
sigma=.0728; %N/m
mu=3.06*10^-4; %Pa*s
PDPA_dir=sprintf('C:\\Users\\...PDPA
Data\\water\\%spsi\\', num2str(psi(n)));
elseif fluid==3
disp('This data is for JP-8')
A1='JP-8';
density=805; %kg/m^3
sigma=.0271; %N/m
nu=2*10^-6; %m^2/s
mu=nu*density;
PDPA_dir=sprintf('C:\\Users\\... PDPA Data\\JP-8\\JP-
8\\%spsi\\', num2str(psi(n)));
elseif fluid==4
disp('This data is for Methanol')
A1='Methanol';
density=791; %kg/m^3
sigma=.023; %N/m
mu=5.44*10^-4; %Pa*s
PDPA_dir=sprintf('C:\\Users\\...PDPA
Data\\Methanol\\Methanol\\%spsi\\', num2str(psi(n)));
end
list=dir(PDPA_dir);

%Extracts the X and Z coordinate from the filename
for a=3:length(list)
filename=sprintf('%s%s', PDPA_dir, list(a).name);
name_string=list(a).name;
x_coordinate(a-2,1)=str2double(name_string(1,7:8));
z_coordinate(a-2,1)=str2double(name_string(1,4:5));

%Extracts the selected value of interest

data = csvread(filename, 2, 0);

%Extracts the Mean Radial Velocity
if valueofinterest==1
value(a-2,1)=data(1,33);
A2='Mean Radial Velocity (m/sec)';
A3='Mean Radial Velocity';

%Extracts the Mean Axial Velocity
elseif valueofinterest==2

```

```

value(a-2,1)=data(1,34);
A2='Mean Axial Velocity (m/sec)';
A3='Mean Axial Velocity';

%Extracts the RMS Radial Velocity
elseif valueofinterest==3
    value(a-2,1)=data(1,35);
    A2='Radial Velocity RMS (m/sec)';
    A3=' RMS Radial Velocity';

%Extracts the RMS Axial Velocity
elseif valueofinterest==4
    value(a-2,1)=data(1,36);
    A2='Radial Velocity RMS (m/sec)';
    A3='RMS Axial Velocity ';

%Extracts the Sauter Mean Diameter
elseif valueofinterest==5
    value(a-2,1)=data(1,30);
    A2='Sauter Mean Diameter (um)';
    A3='D_3_2';

%Extracts the RMS Diameter
elseif valueofinterest==6
    value(a-2,1)=data(1,32);
    A2='Diameter RMS (um)';
    A3='RMS Diameter';

%Extracts the mean axial and radial velocities and computes the
%mean velocity magnitude
elseif valueofinterest==7
    value1(a-2,1)=data(1,33);
    value2(a-2,1)=data(1,34);
    value=sqrt(value1.^2+value2.^2);
    M=[value1 value2 value];
    A2='Mean Composite Velocity (m/sec)';
    A3='Mean Composite Velocity';

%Computes the velocity magnitude as above, then uses the SMD value
%to compute the droplet weber number
elseif valueofinterest==8
    value1(a-2,1)=data(1,33);
    value2(a-2,1)=data(1,34);
    value3(a-2,1)=data(1,30);
    value4=sqrt(value1.^2+value2.^2);
    Weber = density/sigma * value4.^2 .* (value3*10e-6);
    value=Weber*10e-5;
    M=[value1 value2 value4 value3 value];
    A2='Weber number (10^-^5)';
    A3='Droplet Weber Number';

%Computes the velocity magnitude as above, then uses the SMD value
%to compute the droplet Reynolds number
elseif valueofinterest==9

```

```

value1(a-2,1)=data(1,33);
value2(a-2,1)=data(1,34);
value3(a-2,1)=data(1,30);
value4=sqrt(value1.^2+value2.^2);
Re=density/mu*value4.* (value3*10e-6);
value=Re*10e-5;
M=[value1 value2 value4 value3 value];
A2='Reynolds number (10^-^5)';
A3='Droplet Reynolds Number';

%Extracts raw droplet values and creates histogram of droplet
sizes
elseif valueofinterest==10
    value(1:275,1)=data(1:275,15);
    value(1:275,2)=data(1:275,17);

    if z_coordinate(a-2)==25
        heightactual=25;

    elseif z_coordinate(a-2)==50
        heightactual=50;

    elseif z_coordinate(a-2)==75
        heightactual=75;
    end

    if psi==15;
        pressure=103;
    elseif psi==20;
        pressure=137;
    elseif psi==30;
        pressure=206;
    elseif psi==40;
        pressure=275;
    elseif psi==50;
        pressure=344;
    end

    clear('str','formatSpec','max')
    figure(a-2)
    ScreenSize = get(0,'ScreenSize');
    figure('Position',[50 50 1080 600])
    max=max(x_coordinate);
    hist(value(:,1),20)
    xlabel('Diameter (um)','fontsize',32);
    set(gca, 'fontsize',25)
    formatSpec=' %s, %d mm axially, %d mm radially, %d kPa';
    str=sprintf(formatSpec,A1,heightactual,max, pressure);
    ylabel('Counts','fontsize',32)
    title(str,'fontsize',32)
    value=(1:length(x_coordinate))';
end

end

```

```

P=(1:length(x_coordinate))';
P(1:length(x_coordinate))=n;
points=[x_coordinate, z_coordinate,P, value];
%%
%% Creates a matrix of all points at a pressure
%%
if points(:,3)==1
    points1=points;
elseif points(:,3)==2;
    points2=points;
elseif points(:,3)==3;
    points3=points;
elseif points(:,3)==4;
    points4=points;
elseif points(:,3)==5;
    points5=points;
end

for e=1:size(points,1);
    if points(e,2) == height;
        B(counter,:) = points(e,:);
        counter = counter + 1;
    end
end

fun{1,n}=points;
end

%%
%%Creates a matrix of all values at a given axial height
%%
for f=1:size(B,1);
    if B(f,3)== 1;
        Fifteen(counter2,:) = B(f,:);
        counter2 = counter2+1;
    end

    if B(f,3)== 2;
        Twenty(counter3,:) = B(f,:);
        counter3 = counter3+1;
    end

    if B(f,3)== 3;
        Thirty(counter4,:) = B(f,:);
        counter4 = counter4+1;
    end

    if B(f,3)== 4;
        Forty(counter5,:) = B(f,:);
        counter5 = counter5+1;
    end

    if B(f,3)== 5;

```

```

    Fifty(counter6,:) = B(f,:);
    counter6 = counter6+1;
end
end

%If statement to plot data or disregard if histogram is already displayed
if valueofinterest==10
    disp('histogram')
else

    ScreenSize = get(0,'ScreenSize');
    figure('Position',[50 50 670 500])
    plot(Fifteen(:,1),Fifteen(:,4),'-ob',Twenty(:,1),Twenty(:,4),'-
og',Thirty(:,1),Thirty(:,4),'-or',Fourty(:,1),Fourty(:,4),'-
oc',Fifty(:,1),Fifty(:,4),'-om')
    legend('103.4 kPa', '137.9 kPa', '206.84 kPa', '275.79 kPa', '344.74
kPa','Location','Best')
    xlabel('Distance from centerline of injector (mm)','fontsize',16)
    formatSpec2='%s';
    str2=sprintf(formatSpec2,A2);
    ylabel(str2,'fontsize',16)
    formatSpec = '%s, %s, %dmm from the injector';
    str=sprintf(formatSpec,A3,A1, height);
    title(str,'fontsize',16)
end

% Set filename with string and file extension
%filename1 = sprintf('%s.fig',str);
%filename2 = sprintf('%s.bmp',str);

% Save file
% 'gcf' is "get current figure"
%saveas(gcf,filename1);
%saveas(gcf,filename2);

%b    blue        .    point        -    solid
%g    green       o    circle       :    dotted
%r    red         x    x-mark      -.   dashdot
%c    cyan        +    plus        --   dashed
%m    magenta    *    star        (none) no line

```

## Acknowledgements

I would like to extend my sincere thanks and gratitude to everyone who helped make this work possible. Specific thanks, to Dr. Terry Meyer for his guidance, technical support, understanding, help and outstanding effort throughout this work and over the course of a significant portion of my collegiate academic career. Your model work ethic, technical knowledge, patience and understanding have and will continue to inspire me as I continue my professional career in combustion and propulsion research. I would also like to thank the other members of my program of study; Dr. James Hill and Dr. Theodore Heindel, for your efforts and contributions to this work.

I would also like to thank and acknowledge Alek Poniatowski, Robert Jaeger and Robert Morehead for their incredible amount of technical support and guidance in helping to accomplish this work. Additional thanks goes to Ben Halls, Jordan Tiarks, Dr. Joseph Miller, Chloe Dedic and all members of Dr Meyers research group for their help, inspiration and great memories during my time as a Research Assistant.

Lastly and certainly not least, many thanks to my wonderful wife Emily for her incredible patience, guidance and support. Also thanks to my parents and family members for their incredible amount of inspiration, patience and endless love they have given me throughout my academic career and life.